Synthesis of Mesoporous Metal Oxide Materials

by

Danielle Ladd

A Dissertation Presented in Partial Fulfillment
of the Requirements for the Degree
Doctor of Philosophy

Approved July 2012 by the
Graduate Supervisory Committee:

Dong Seo, Chair
Ulrich Haussermann
William Petuskey

ARIZONA STATE UNIVERSITY

August 2012

ABSTRACT

Nanoporous crystalline oxides with high porosity and large surface areas are promising in catalysis, clean energy technologies and environmental applications all which require efficient chemical reactions at solid-solid, solid-liquid, and/or solid-gas interfaces. Achieving the balance between open porosity and structural stability is an ongoing challenge when synthesizing such porous materials. Increasing porosity while maintaining an open porous network usually comes at the cost of fragility, as seen for example in ultra low density, highly random porous aerogels.

It has become increasingly important to develop synthetic techniques that produce materials with these desired properties while utilizing low cost precursors and increasing their structural strength. Based on non-alkoxide sol-gel chemistry, two novel synthetic methods for nanoporous metal oxides have been developed. The first is a high temperature combustion method that utilizes biorenewable oil, affording gamma alumina (γ-Al_2O_3) with a surface area over 300 cm^3/g and porosity over 80% and controllable pore sizes (average pore width 8 to 20 nm). The calcined crystalline products exhibit an aerogel-like textural mesoporosity. To demonstrate the versatility of the new method, it was used to synthesize highly porous amorphous silica (SiO_2) which exhibited increased mechanical robustness while achieving a surface area of 960 m^2/g and porosity of 85%.

The second method utilizes sequential gelation of inorganic and organic precursors forming an interpenetrating inorganic/organic gel network. The method affords yttria-stabilized zirconia with surface area over 90 cm^3/g and porosity over 60% and controllable pore sizes (average pore width 6 to 12 nm). X-ray diffraction, gas sorption analysis, Raman spectroscopy, nuclear magnetic resonance spectroscopy and electron microscopy were all used to characterize the structure, morphology, and the chemical structure of the newly afforded materials. Both novel methods produce products that show superior pore properties and robustness compared to equivalent commercially available and currently reported materials.

ACKNOWLEDGMENTS

To all who have helped me along the way.

TABLE OF CONTENTS

CHAPTER Page

CHAPTER Page

CHAPTER Page

LIST OF FIGURES

CHAPTER 1

INTRODUCTION

1.1 Introduction

The diverse crystal structures of metal oxides are responsible for the many mechanical, thermal, electrical, optical,[1] and catalytic properties they exhibit. Open porosity and high surface area are necessary for certain applications, such as thermal insulation, filtration, chemical sensors, batteries, solar cells, fuel cells, and catalysis.[2,3] It is the combination of these two requirements that has made highly porous metal oxides desirable materials. Highly nanoporous metal oxides with accessible three-dimensional surface areas offer unprecedented opportunities in catalysis, energy technologies, environmental remediation, etc.,[4-6] and there has been continual effort to develop new synthetic routes with a particular emphasis on better control of their chemical, physical and pore-structural characteristics.[7-11]

Porous materials are classified by several metrics including pore ordering, connectivity and dimensionality, and pore size and pore size distribution, all of which determine the overall properties of the resulting material.[2] Regarding the later, IUPAC has developed three categories for pore size classification; micropores whose diameters are less than 2 nm, mesopores whose diameters fall between 2 and 50 nm, and macropores whose diameters are greater than 50 nm.[12] Microporous materials are utilized for molecular size selectivity and separation. Macroporous

materials are utilized for their efficient mass transport. Mesoporous materials can be utilized for size selectivity but contain pores large enough for suitable mass transport.

In addition to size, pore connectivity and morphology directly influences the material's properties. The pores of open porous materials are accessible from the surface, allowing for increased fluid permeability, lower density and higher surface area as compared to closed porous materials whose pores are completely isolated.[2] The larger surface area and interconnectivity of pores is desirable for catalysis and filtration purposes, but the increased porosity comes at the cost of mechanical strength. This is well demonstrated in the case of Aerogels. Aerogels are a type of low density, mesoporous material that exhibit an extensively open 3D-connected nanopore structure with volume porosities that can reach up to 99.8% (that is, 99.8% of the material is empty).[13] However, such high porosity is linked to structural fragility and thermal instability of aerogels. When aged in a liquid or heat treated they often undergo structural evolution by chemical transformation, making them a material with desirable properties but structural weaknesses.[5] Aerogels will be discussed in further detail in Section 1.3.

Silica (SiO_2) is the leading metal oxide material in the aerogel research field, owing to the depth of research already done on its precursors, the ease and control of its synthesis, and the ability to tailor the final material for specific applications.[5] The large scope of applications

for silica aerogels ranges from thermal and acoustical insulation, to Cerenkov detectors and catalytic supports. These applications utilize the unique optical and thermal conductivity properties of silica aerogels as well as the highly porous structure.[13]

Alumina (Al_2O_3) aerogels accounted for about 8 % of the total publications on aerogels from 2009-2011.[14] Conversely, alumina dominated the catalysis research field publication wise, ahead of silica, carbon, and metal organic frameworks (MOF's). Alumina has many transition phases, one being γ-Al_2O_3 which is formed from the thermal dehydration of boehmite, AlO(OH). The crystal structure of γ-Al_2O_3, shown in Figure 1.1, is described as a defect spinel structure. Starting from a spinel structure with a chemical formula of M_3O_4 ($M^{2+}(M^{3+})_2O_4$), one third of the M^{+2} atoms are removed and the remaining M^{+2} atoms are replaced by M^{+3} to restore electrical neutrality ($(M^{3+})_{2/3}(M^{3+})_2O_4$). The resulting spinel structure with a chemical formula of M_2O_3 has 1/9 of all the cation sites vacant; i.e., $(M^{3+})_{3(1-x)}O_4$ where x = 1/9. For γ-Al_2O_3, however, the exact distribution of these vacancies between tetrahedral and octahedral positions is still controversial.[15] Gamma-Al_2O_3 is the desired polymorphic phase for catalytic application because of the surface chemistry that the phase exhibits due to coordinatively unsaturated sites.

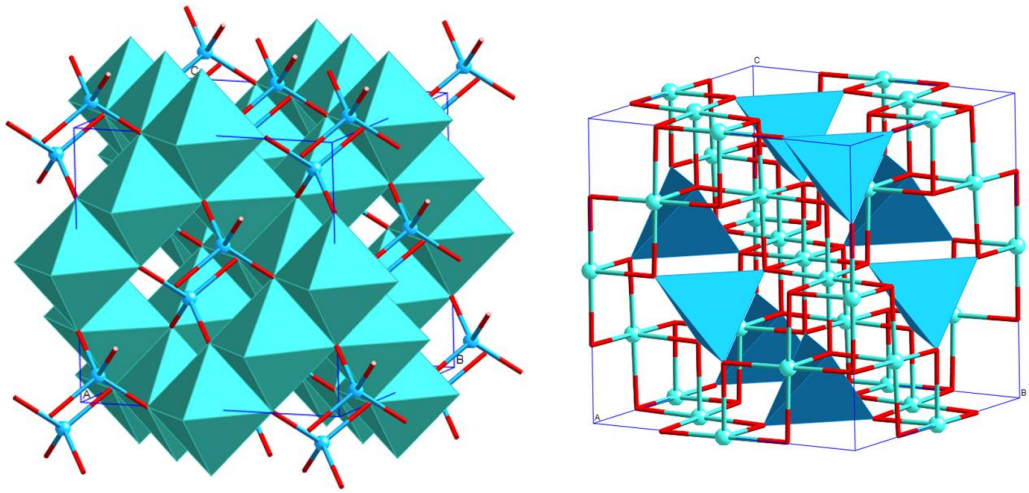

Figure 1.1. Defect spinel structure of γ-Al_2O_3, with Al octahedral (left) and tetrahedral (right) positions shown with tetrahedra.

Another dominating material in the catalysis field is yttria-stabilized zirconia (YSZ). For applications such as a solid electrolyte in solid-oxide fuel cells (SOFC) and catalysis; high porosity, large surface area and thermal stability are required of the material. However, the success in producing such a material has been limited so far due to the difficult synthesis process and the tendency for structural collapse. The parent zirconia lattice has three different possible polymorphs, monoclinic, tetragonal and cubic. Monoclinic phase is formed in bulk zirconia at ambient pressure and at temperatures lower than 1170 °C. However, with the addition of 8 – 9 mol% yttria (Y_2O_3) the high temperature cubic phase, which is desired for its increased mechanical and thermal properties, may become stable or metastable at room temperature.[16] Cubic YSZ adopts a fluorite structure (Figure 1.2), with zirconium cations occupying FCC positions, coordinated with eight equidistant oxygen atoms occupying

interstitial sites. The primitive cell belongs to the space group F*m*-3*m* and has lattice parameter *a* ≈ 5.12Å (the lattice parameter can vary with varying dopant mol %). The substitution of Y^{3+} for Zr^{4+} causes the formation of oxygen vacancies to account for the charge imbalance. These oxygen vacancies are what give YSZ such high ionic conductivity and make porous YSZ materials desirable for SOFC applications.

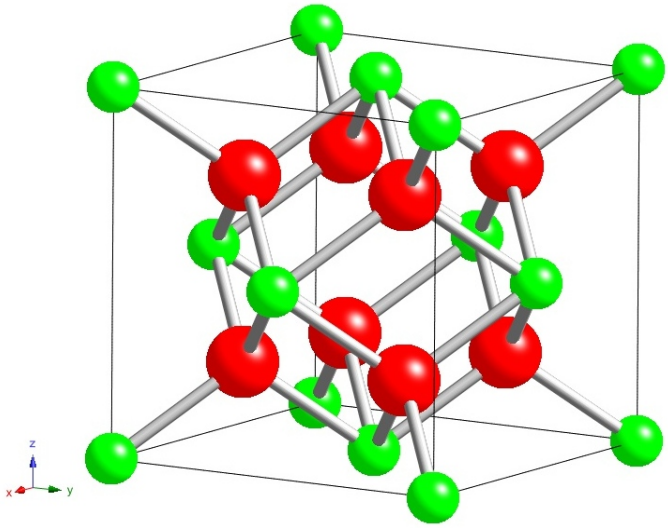

Figure 1.2. Cubic YSZ crystal structure.

1.2 Sol-Gel Chemistry

Porous metal oxides can be synthesized through a variety of techniques but sol-gel chemistry is attractive due to the fact that the synthesis is done under room conditions at low temperature with inexpensive precursors. The ability to tailor the morphology, textural properties, and shape of the resulting material by simply varying the drying technique or precursors demonstrates the versatility of sol-gel chemistry.[17] Metal oxide sol-gel materials are typically prepared using a metal alkoxide

precursor which then undergoes hydrolysis and condensation.[18] The intimate mixing of the molecular precursors on an atomic scale makes sol-gel synthesis attractive for multi-component systems. The initial formation of sols, or stable colloids, is followed by polymerization across the volume of the container resulting in gelation. Lastly, drying of the gel produces homogeneous monoliths or powders.[19]

The formation of the sol can be achieved through various routes and precursors. Metal alkoxides are the most versatile precursor due to their high reactivity with nucleophilic solvents which are used during sol-gel synthesis.[20] However there are only a small number of metal alkoxides that are readily available and not sensitive to heat, moisture and light, making the precursor non-ideal for the synthesis of many transition metal oxides. Sols have also been prepared through the aqueous precipitation of metal ions in the presence of a base.[18] Inorganic salts have been shown to be a versatile and inexpensive alternative to alkoxide precursors,[21-23] however their sol-gel polymerization is more complicated due to the presence of various molecular species that form depending on the initial reactant concentration, pH of the solution, and the oxidation of the metal.[18] The steps of sol-gel synthesis will be discussed in sequential order.

Sol-gel polymerization is initiated by the hydrolysis of the metal salt where a cation M^{Z+} is solvated by water molecules by dissolution of the salt in water. The hydrolysis equilibrium, as shown in *Equation 1* is

established with three types of ligands present in a non-complexing aqueous media: aquo (OH_2), hydroxo (OH), and oxo (=O).[18]

$$\left[M-OH_2\right]^{Z+} \leftrightarrow \left[M-OH\right]^{(Z-1)+} + H^+ \leftrightarrow \left[M=O\right]^{(Z-2)+} + 2H^+ \qquad \textit{Equation 1}$$

The coordinated water molecules become more acidic due to the increased positive partial charge on the hydrogen. This increased charge is the result of a partial charge transfer between the filled 3_{a1} bonding orbital of the water molecule and the empty transition metal ion d orbital. The established equilibrium shown in *Equation 1* depends on the magnitude of the charge transfer while the degree of hydrolysis is dependant on the coordination number, electronegativity and the charge density of the cation and the pH.[18,24] Metal cations with high valence (Z > 5) generally form oxo or oxo-hydroxo complexes while cations with lower valence (Z < 4) form aquo, hydroxo, and hydroxo-aquo complexes. The degree of hydrolysis of cations with Z=4 is pH dependant and the complex can be formed with a combination of oxo, hydroxo, and aquo ligands.

After hydrolysis of the metal cation, condensation occurs through oxolation or olation depending on the coordination unsaturation of the cation.[18,24] Oxolation is the formation of M-O-M bridges. If the complex is coordinatively unsaturated then this occurs through nucleophilic addition. A two-step substitution reaction between oxo-hydroxo species occurs if the complex is coordinatively saturated. The first step being nucleophilic addition and the second being the elimination of water, forming a M-O-M bond. The second route of condensation, olation, is the formation of

hydroxy bridges (M-OH-M) between metal centers through nucleophilic substitution of the coordinatively saturdated hydroxo-aquo complexes. Water acts as the leaving group while the hydroxo group acts as the nucleophile. As more water molecules leave the metal center, the hydroxo groups lose their nucleophilicity, halting condensation and requiring a further reaction initiator or catalyst for further hydrolysis and condensation to occur.

Organic epoxides have been added as gel-initiators for inorganic salt sol-gel syntheses.[22,25,26] The epoxide acts as an acid scavenger, slowly increasing the pH facilitating the hydrolysis and condensation of the hydrated inorganic salts. The metal cation must be acidic enough to protonate the epoxide oxygen, whose ring is irreversibly opened by nucleophilic attack from the anionic conjugate base. The counter ion of the metal salt must be a stronger nucleophile than water, otherwise nucleophilic attack by water on the epoxide results in the formation of a diol and regeneration of a proton. Chloride and nitrates are sufficient nucleophiles, making chloride and nitrate metal salts excellent precursors for the epoxide addition method. The proper ring opening reaction results in the elimination of protons from solution and a gradual, uniform increase of pH which supports controlled oxolation and olation reactions to occur extensively, resulting initially in the formation of a sol and secondly the formation of a solid metal oxide gel network.

The formation of a solid network during gelation results in a wet gel. The term “wet” refers to the solvent present inside of the pores created by the interconnecting metal oxide network. The method which is used to remove this liquid determines the final morphology and pore properties of the metal oxide material.

1.3 Aerogels and Supercritical Drying Technique

The method of drying wetgels strongly influences the porous structure and morphology of the final material (Figure 1.3) adapted from Rolison and Dunn.[27] Supercritical drying is done at high temperature forming aerogels, freeze-drying is done at low temperature forming cryogels, evaporative drying is done at ambient conditions forming xerogels and ambigels.[13]

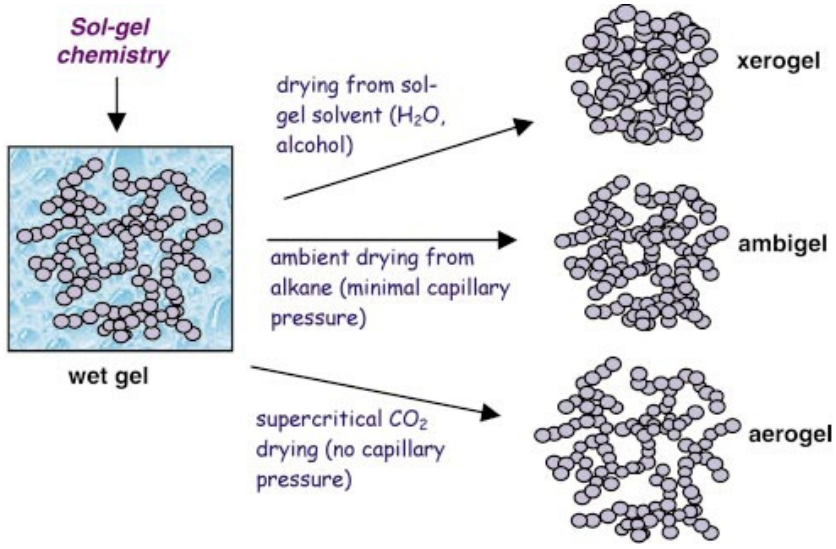

Figure 1.3 Various drying techniques used on sol-gel formed wet gels.

The solid structure of cryogels does not vary differently from that of aerogels, as both drying techniques remove the liquid form the pores with minimal destruction of the wetgel solid network, therefore cryogels will not be discussed further. Xerogels are the least porous of the materials, due to the collapse of the highly porous inorganic solid network as the solvent inside of the pores is evaporated off.[5,13,28] During evaporation, as the liquid retreats into the gel body, a meniscus is formed inside of the pores. As this meniscus recedes through the pore structure, a large force due to capillary pressure (*Equation 2*) acts on the pore walls. The capillary pressure is dependant on the specific energy of the liquid-vapor interface, γ_{LV}, the contact angle, θ, and the surface to volume ratio of the empty pores, $\frac{S_P}{V_P}$.[29]

$$P_C = -\frac{\gamma_{LV}\cos(\theta)S_P}{V_P} \qquad \textit{Equation 2}$$

These forces are strong enough to cause the pore walls to collapse in on themselves (Figure 1.4), resulting in significant shrinkage of the gel body (greater than 75% by volume) and densification of the overall inorganic network. The ambient conditions under which xerogels are dried makes the evaporative drying technique attractive, but the loss of the highly porous structure formed in the wetgel proves to be a significant problem.

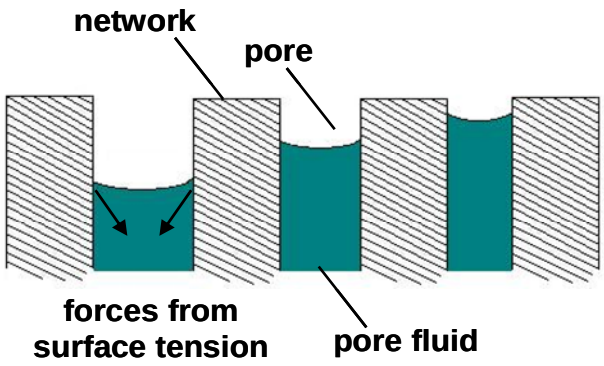

Figure 1.4. Capillary forces due to the formation of a meniscus inside of a pore and the resulting stress on the solid network.

Comparatively, when the liquid inside of the pores is replaced with air without significant change in the volume of the gel body or altering the solid structure, then an aerogel is formed.[13] These highly divided solids have their original gel structure preserved, resulting in low density and high surface area materials. Samuel Kistler was the first to explore the possibilities of removing liquid inside of a gel network while minimizing the formation of capillary pressures by using a supercritical fluid.[30] Supercritical fluids are unique in that they can be thought of as a high density gas or low density liquid, allowing them to have liquid like solubility and nearly gas-like permeability and diffusion. Kistler exploited these properties by taking the solvent inside of the pores up to super critical conditions where there is no distinction between the liquid and vapor phase, and subsequently degassing the solvent while preserving the solid gel structure. At a supercritical state the liquid and vapor phases of the solvent have equal densities and there is no liquid-vapor interface, eliminating the formation of a meniscus and capillary pressure. If the path

of heating and pressurization of the solvent never crosses the phase boundary (Figure 1.5) adapted from Pierre and Pajonk,[5] then the solvent can be vented off once past the critical temperature, T_c, and critical pressure, P_c, leaving the solid gel structure in near the same state as it existed in the wetgel.

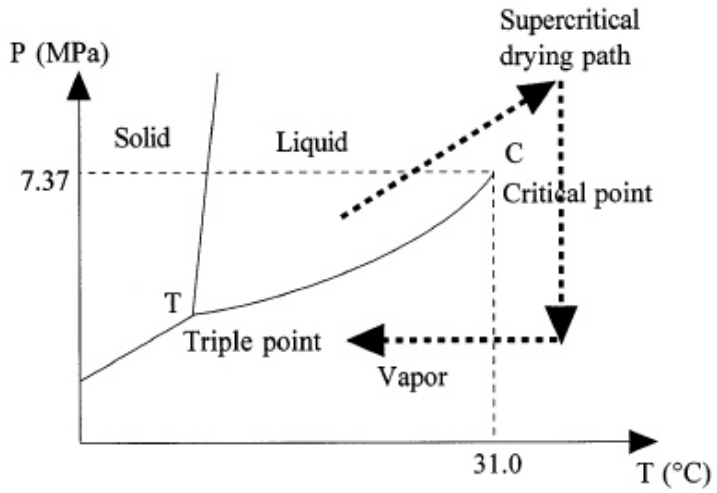

Figure 1.5. Phase diagram of CO_2 marked with possible supercritical drying path.

The process of supercritical drying requires the use of a high pressure autoclave, where the wetgel is heated in a closed environment so that the temperature and pressure can exceed T_c and P_c of the pore liquid. Due to the extreme conditions required to take most solvents up to supercritical state, carbon dioxide is one of the most common solvents used in supercritical drying of sol-gel derived materials. The T_c and T_p of CO_2 are 31℃ and 74 bar respectively. However, carbon di oxide is not miscible with water, one of the components present in the mother liquor

after sol-gel processing, so extensive solvent exchange is required prior to drying. If solvent exchange is not complete, the presence of a liquid-liquid interface due to immiscibility of solvents can cause the formation of capillary pressure inside of the pores.[31] Even after a miscible solvent has been exchanged with the mother liquor inside of the pores, a sufficient amount of time is needed to flush the entire pore structure of the gel with liquid CO_2 before taken up to supercritical conditions. Alcohols can be used as a supercritical solvent, however their high T_c makes the drying process more dangerous and some materials dissolve during alcohol supercritical treatment. The final aerogel materials produced from the supercritical drying method are unique materials with incredible surface area and porosity properties, however the time needed for initial solvent exchange, CO_2 flushing, and the high temperature and pressure required to reach supercritical conditions make the process dangerous, expensive, and time consuming.

Several ambient-pressure drying techniques have been developed for the synthesis of SiO_2 aerogel-like materials, known as ambigels. The first technique requited surface modification of SiO_2 wetgels by a series of solvent exchange steps that resulted in the conversion of surface hydroxy groups into silyl groups using chlorotrimethylsilane.[32,33] This modification reduces the reactivity of the surface and when the gel shrinks during evaporation of the solvent there is no formation of Si-O-Si bonds across the width of the pores, causing irreversible narrowing. This results in the

gel “springing back” close to its original volume after the solvent has been evaporated. The critical requirement for this drying process is that the solid network of the gel must be strong and stable enough to withstand shrinkage of up to 25 percent by volume during drying and subsequent expansion back to the original volume of the gel without significant destruction of the network. The final ambigel material had an aerogel-like structure, but still exhibited a lower porosity and higher density then respective aerogels.

Ambigels could also be achieved if SiO_2 wetgels were aged in a monomeric solution such as tetraethylalcoxysilane.[34] The condensation of the monomers in the weaker areas of the gel, such as the particle necks and micropores, resulted in a significant increase in network strength. The more robust wetgel could then be dried at increased temperature with very minimal shrinkage. As stated above, the use of alkoxides as precursors and aging solvents becomes a limiting factor due to the toxicity and instability with handling when trying to synthesize non-silicate aerogel materials. It is apparent that there is a need for new synthetic routes for producing highly porous aerogel like materials that bypasses the use of a supercritical autoclave and are versatile enough to be applied to many metal oxide systems without relying on selective chemicals.

1.4 Aging

The high temperature and pressure environment that wetgels are exposed to during supercritical drying causes a structural change. Even

though a wetgal has surpassed its gel point, the chemical reactions that bring about gelation continue well beyond this point.[35] During the time after gelation, the gel undergoes polymerization, coarsening and phase transformation during aging. The first, polymerization, is when there is an increase in connectivity of the network through condensation reactions. In the coarsening process, there is dissolution of solid material from the positive curvature of the particle and re-precipitation of that material in the neck region between two particles where the solubility is less due to the negative curvature. This dissolution and re-precipitation causes an increase in strength and stiffness of the gel. Lastly, a phase transformation can occur through the reorganization of the solid structure. All of these aging effects are strongly influenced by various factors such as temperature, pressure, pH, type of solvent and concentration of solid material; such conditions that are changed during supercritical drying. It can be concluded then while there is little shrinkage during supercritical drying, 0-25% depending on synthetic conditions, the structure of the resulting aerogel is not the same as the network in the wetgel and that the solid network undergoes a strengthening during high temperature drying. Post-drying, an additional heating step is required for the strengthening of the solid structure and for possible phase transition from amorphous to crystalline for most metal oxide materials.

Aerogels are described as highly divided solids with metastable character,[5] and if immersed in liquid they collapse immediately.[28] For

example, silica aerogels loose their structural integrity upon immersion in a liquid due to the extreme capillary force exerted on the pore wall[36] and undergo extensive densification/shrinkage above 850 ºC by particle sintering under viscous flow.[11,13,37,38] In fact, such densification has been utilized to strengthen the silica aerogels by sintering at 900ºC for a short period of time (<60min) to give a volume density of ~80%.[11] The resulting material is more robust but the post drying heat-treatment is an additional added step to the already multi-step process required for the synthesis and production of aerogels.

1.5 High Temperature Combustion Synthetic Method

Looking at the full process required for the synthesis of aerogels brings to light the multitude of steps and bottlenecks present in the synthetic process and the flaws that are still present in the final material. The first synthetic bottleneck is the extensive solvent exchange that must be completed in order to get the wet gel ready for supercritical drying. Second, the high pressure autoclave required for supercritical drying is both energy and time intensive. Third, an additional heating step post drying is needed for any phase change required to obtain the desired final material. This heating step comes at the cost of decreased porosity but increased mechanical strength. Taking these issues into account, the idea for a new synthetic route that replaces the initial pore liquid with a liquid that could be rapidly combusted with minimal formation of liquid vapor interface, forming a solid residue to act as a structural support that could

be slowly removed all while at a temperature that would induce any desired phase change but not at the cost of porosity, appears promising.[39] The aforementioned synthetic technique will be referred to as the high temperature combustion synthesis from this point forward.

The liquid that replaces the initial pore liquid must possess such properties as high boiling point, low flash point, high carbon content, and similar viscosity as the exchanged solvent. A high boiling point is desired in order to achieve minimal formation of liquid-vapor interfaces, prior to combustion inside of the pores which is detrimental to the pore structure as seen in typical ambient temperature and pressure drying of wetgels. A low flash point is desired so that the liquid spontaneously combusts, without the need for external ignition, rapidly and at a temperature as close to the boiling point as possible. High carbon content results in the formation of a large amount of carbon residue which can act as a structural support for the solid metal oxide network once the pore liquid has been removed. Lastly, a similar viscosity to the replaced pore liquid is desired in order to insure complete and efficient exchange of the two liquids.

Oil is a sufficient candidate that meets all of the above requirements as well as being economical and easy to handle. Vegetable oils are composed of 93-95% triglycerides by weight, typically with long-chain fatty acids ranging 8-24 carbons in length with varying degrees of units of unsaturation and the presence of various functional groups,

depending on the species that the oil was extracted from.[40] Recently, vegetable oils have become the most widely used renewable resource in the chemical and polymer industry, with 15% of the ~126 million tons produced annually being used in the chemical industry while 80% is used for human nutrition.[41] Castor oil is an attractive oil from an industrial and chemical perspective because it is composed of up to 95% ricinolic acid, an ω-9 fatty acid that can be thermally polymerized. The presence of a hydroxyl group on C12 makes the oil miscible with alcohol, a property that could be utilized during solvent exchange. The wide variety of oils available, each with their own structural and thermal properties, gives for numerous possibilities of potential liquids to exchange into the pores of inorganic wetgels for the proposed high temperature combustion synthesis.

Recycled oil, or waste vegetable oil (WVO), is an alternative to pristine oil when looking at large scale production of mesoporous materials using the high temperature combustion method. WVO is available in huge abundance as a waste product from the commercial food industry and has recently become the dominating precursor for the production of biodiesel.[42] WVO is desired for replacing pristine vegetable oil owing to the fact that it is a cheaper raw material, eliminates the cost of waste product disposal and reduces the need to use land for bio-diesel producing crops. The versatility of the high temperature combustion synthesis of mesoporous materials would allow the use of any of the above described oils, with the stipulation that the pore liquid should first be

exchanged with a solvent that is miscible with both the mother liquor and the utilized oil. This versatility makes the synthesis attractive at both a lab scale and potentially could be applied at an industrial production scale.

The numerous application demands for highly porous metal oxides has brought to light the need for efficient, low cost, versatile synthetic processes able to produce materials with controllable pore properties and increased mechanical strength. The aim of this thesis is to present two new synthetic routes for the production of highly porous metal oxide materials and demonstrate the versatility of these processes by applying them to several metal oxide systems. The resulting materials are comparable or superior to those most recently reported in literature or commercially available.

1.6 References

(1) Livage, J.; Babonneau, F.; Sanchez, C. *Sol-Gel Opt.* **1994**, 39.

(2) K. Ishizaki, S. K., and M. Nanko *Porous Materials; Process technology and applications*; Kluwer Academic Publishers, 1998.

(3) Chan, K. K.; Brownstein, A. M. *American Ceramic Society Bulletin* **1991**, *70*, 703.

(4) Thomas, J. M.; Hernandez-Garrido, J. C.; Raja, R.; Bell, R. G. *Physical Chemistry Chemical Physics* **2009**, *11*, 2799.

(5) Pierre, A. C.; Pajonk, G. M. *Chemical Reviews (Washington, DC, United States)* **2002**, *102*, 4243.

(6) Fryxell, G. E.; Mattigod, S. V.; Lin, Y.; Wu, H.; Fiskum, S.; Parker, K.; Zheng, F.; Yantasee, W.; Zemanian, T. S.; Addleman, R. S.; Liu, J.; Kemner, K.; Kelly, S.; Feng, X. *Journal of Materials Chemistry* **2007**, *17*, 2863.

(7) Huo, Q.; Margolese, D. I.; Ciesla, U.; Feng, P.; Gier, T. E.; Sieger, P.; Leon, R.; Petroff, P. M.; Schueth, F.; Stucky, G. D. *Nature (London, United Kingdom)* **1994**, *368*, 317.

(8) Zhang, Z.; Hicks, R. W.; Pauly, T. R.; Pinnavaia, T. J. *Journal of the American Chemical Society* **2002**, *124*, 1592.

(9) Baumann, T. F.; Gash, A. E.; Fox, G. A.; Satcher, J. H., Jr.; Hrubesh, L. W. In *Handb. Porous Solids*; Schüth, F., Sing, K. S. W., Weitkamp, J., Eds.; Wiley-VCH: Weinheim, Germany, 2002; Vol. 3, p 2014.

(10) De Soler-Illia, G. J.; Sanchez, C.; Lebeau, B.; Patarin, J. *Chemical Reviews (Washington, DC, United States)* **2002**, *102*, 4093.

(11) Long, J. W.; Rolison, D. R. *Acc. Chem. Res.* **2007**, *40*, 854.

(12) Schaefer, D. W. *MRS Bulletin* **1994**, *19*, 14.

(13) Husing, N.; Schubert, U. *Angewandte Chemie, International Edition* **1998**, *37*, 22.

(14) SciFinder; CAS American Chemical Society: 2010.

(15) Sohlberg, K.; Pennycook, S. J.; Pantelides, S. T. *Journal of the American Chemical Society* **1999**, *121*, 7493.

(16) Duwez, P.; Brown, F. H., Jr.; Odell, F. *Journal of the Electrochemical Society* **1951**, *98*, 356.

(17) Brinker, C. J.; Scherer, G. W. In *Sol-Gel Science*; Academic Press: Boston: 1990, p 839.

(18) Livage, J.; Henry, M.; Sanchez, C. *Progress in Solid State Chemistry* **1988**, *18*, 259.

(19) Hench, L. L.; West, J. K. *Chem. Rev.* **1990**, *90*, 33.

(20) Brinker, C. J.; Scherer, G. W. In *Sol-Gel Science*; Academic Press: Boston: 1990, p 1.

(21) Baumann, T. F.; Gash, A. E.; Chinn, S. C.; Sawvel, A. M.; Maxwell, R. S.; Satcher, J. H., Jr. *Chem. Mater.* **2005**, *17*, 395.

(22) Gash, A. E.; Satcher; Simpson, R. L. *Chemistry of Materials* **2003**, *15*, 3268.

(23) Chervin, C. N.; Clapsaddle, B. J.; Chiu, H. W.; Gash, A. E.; Satcher, J. H., Jr.; Kauzlarich, S. M. *Chemistry of Materials* **2005**, *17*, 3345.

(24) Brinker, C. J.; Scherer, G. W. In *Sol-Gel Science*; Academic Press: Boston: 1990, p 21.

(25) Gash, A. E.; Tillotson, T. M.; Satcher Jr, J. H.; Hrubesh, L. W.; Simpson, R. L. *Journal of Non-Crystalline Solids* **2001**, *285*, 22.

(26) Gash, A. E.; Tillotson, T. M.; Satcher, J. H., Jr.; Poco, J. F.; Hrubesh, L. W.; Simpson, R. L. *Chem. Mater.* **2001**, *13*, 999.

(27) Rolison, D. R.; Dunn, B. *J. Mater. Chem.* **2001**, *11*, 963.

(28) Brinker, C. J.; Scherer, G. W. In *Sol-Gel Science*; Academic Press: Boston: 1990, p 453.

(29) Brinker, C. J.; Scherer, G. W. In *Sol-Gel Science*; Academic Press: Boston: 1990, p 407.

(30) Kistler, S. S. *Nature (London, U. K.)* **1931**, *127*, 741.

(31) Kistler, S. S. *Journal of Physical Chemistry* **1932**, *36*, 52.

(32) Deshpande, R.; Smith, D. M.; Brinker, C. J. *Materials Research Society Symposium Proceedings* **1992**, *271*, 553.

(33) Huling, J. C.; Bailey, J. K.; Smith, D. M.; Brinker, C. J. *Materials Research Society Symposium Proceedings* **1992**, *271*, 511.

(34) Einarsrud, M.-A.; Haereid, S. *Journal of Sol-Gel Science and Technology* **1994**, *2*, 903.

(35) Brinker, C. J.; Scherer, G. W. In *Sol-Gel Science*; Academic Press: Boston: 1990, p 357.

(36) Lucas, E. M.; Doescher, M. S.; Ebenstein, D. M.; Wahl, K. J.; Rolison, D. R. *J. Non-Cryst. Solids* **2004**, *350*, 244.

(37) Rolison Debra, R. *Science (New York, N.Y.)* **2003**, *299*, 1698.

(38) Parmenter, K. E.; Milstein, F. *J. Non-Cryst. Solids* **1998**, *223*, 179.

(39) Ladd, D. M.; Volosin, A.; Seo, D.-K. *Journal of Materials Chemistry* **2010**, *20*, 5923.

(40) Lu, Y.; Larock, R. C. *ChemSusChem* **2009**, *2*, 136.

(41) Belgacem, M. N.; Gandini, A. *Monomers, Polymers and Composites from Renewable Resources*; Elsevier: Amsterdam, 2008.

(42) Bautista, L. F.; Vicente, G.; Rodriguez, R.; Pacheco, M. *Biomass and Bioenergy* **2009**, *33*, 862.

CHAPTER 2

CHARACTERIZATION TECHNIQUES

2.1 Introduction

All investigations reported in this thesis used a wide range of characterization techniques which further the understanding of the syntheses proposed and the final materials produced. Gas sorption analysis, in particular nitrogen sorption and desorption studies, were used to determine the surface area, pore size, and pore volume of all the produced materials. Powder X-ray diffraction (PXRD) was used for phase identification and crystallite size calculations. Transmission electron microscopy (TEM) and scanning electron microscopy (SEM) allowed the investigation of macro- and microscopic structural properties respectively. Raman spectroscopy was used in firmly identifying polymorphs of the YSZ materials. Solid state magic angle spinning ^{27}Al nuclear magnetic resonance spectroscopy (^{27}Al MAS NMR) was employed to examine the aluminum coordination environment in the γ-alumina. This chapter is divided into individual characterization techniques for which a brief discussion about the basic theory and application specific to this work is given to assist with the discussion and analysis of results in proceeding chapters.

2.2 Powder X-ray Diffraction (PXRD)

The structural arrangement of atoms and molecules can be probed using PXRD techniques. The short wavelength X-rays can be scattered by

electrons in a material and the collection of the elastic scattering events can be directly related to the symmetry and atomic distances of the material through Bragg's law.[1] Bragg's law describes the conditions needed (scattering angle) for diffraction to occur for a given set of lattice plans, given the inter-plane distance and wavelength of the incident X-ray beam. The collected diffraction pattern contains peaks that are directly related to atomic distances, from which crystal structures can be determined (called Bragg reflection peaks or Bragg peaks). Crystallite size in nanocrystalline bulk materials can also be calculated from the diffraction pattern through Scherrer's equation (Equation 1) which correlates the mean size of the crystallite domains (τ) to the broadening of the diffraction peak (β = Full-Width Half-Maximum (FWHM)).[2]

$$\tau = \frac{K\lambda}{\beta \cos\theta} \qquad \textit{Equation 1}$$

Scherrer's equation is applicable for average crystallite sizes up to about 100 nm due to other factors that can cause peak broadening such as instrumental effects. When comparing the average crystallite size determined from Scherrer's equation to the average particle size values calculated from other methods such as gas sorption and electron microscopy, it should be noted that discrepancies may occur if primary particles are not single crystallite domains.

PXRD was used for primary phase identification for the crystalline materials produced. For the porous alumina samples, for example, the

diffraction pattern for the desired gamma transition phase can be distinguished from the other metastable alumina polymorphs (delta and theta) that form at higher temperatures from the dehydration of boehmite. The defect spinel crystal structure of γ-alumina has been previously discussed in Chapter 1, and the transition from γ to δ and θ occurs through a change in the degree of order of the tetrahedral Al sublattice, with θ having a well ordered sublattice and monoclinic structure.[3] The high temperature, thermodynamically stable phase α-alumina adopts the well known corundum structure. The difference in crystal structure allows for primary phase identification through diffraction techniques, which can be further verified by studies on the coordination environment of the aluminum atoms.

2.3 Raman Spectroscopy

Raman spectroscopy can be used for the investigation of materials on the atomic scale and in particular the short range structure. Raman active modes are attributed to a change in polarizability during the vibration of an interatomic bond or series of bonds, providing molecular structure information. The number of normal vibrational modes (3N – 6, with N = to the number of atoms) can be broken down into various irreducible representations in the point group of the molecule. Selection rules are then used to determine which symmetries are Raman active. In the scope of this work, Raman spectroscopy is used for the phase identification of the produced yttria-stabilized zirconia (YSZ) materials.

Typically diffraction techniques are sufficient for determination of crystallographic structure information, but in the case where two phases have very similar structures resulting in indistinguishable diffraction patterns, Raman spectroscopy can be used for primary phase identification as the spectral patterns can be very sensitive to the symmetry of the vibrational normal modes. For YSZ, the tetragonal distortion from the cubic unit cell is only too small to be distinguished by the PXRD patterns.

In order to understand why Raman spectroscopy can be used for phase identification near the phase boundaries of YSZ, the structural differences between the cubic and tetragonal phase of the parent lattice, ZrO_2, must be understood, as well how Y_2O_3 stabilization of ZrO_2 occurs. The cubic phase of zirconia adopts the fluorite structure, and has been extensively described in Chapter 1. The tetragonal phase of YSZ is similar in structure to the cubic phase but adopts two distortions in order to prevent an undesirably close oxygen–oxygen contact and forms a distorted fluorite structure.[4,5] Tetragonal zirconia has a body-centered unit cell belonging to the $P4_2/nmc$ (No. 137) space group with lattice parameters a = 3.610 Å and c = 5.168 Å.[6] In the tetragonal structure, zirconium cations are still coordinated to eight oxygen atoms, however the oxygen atoms are alternately displaced up and down along the c axis (Figure 2.1). This displacement brings four of the nearest neighbor oxygen

atoms closer to the zirconium, to a distance of ~ 2.1 Å, while moving four nearest neighbor oxygen atoms further away, to a distance of ~2.3 Å.

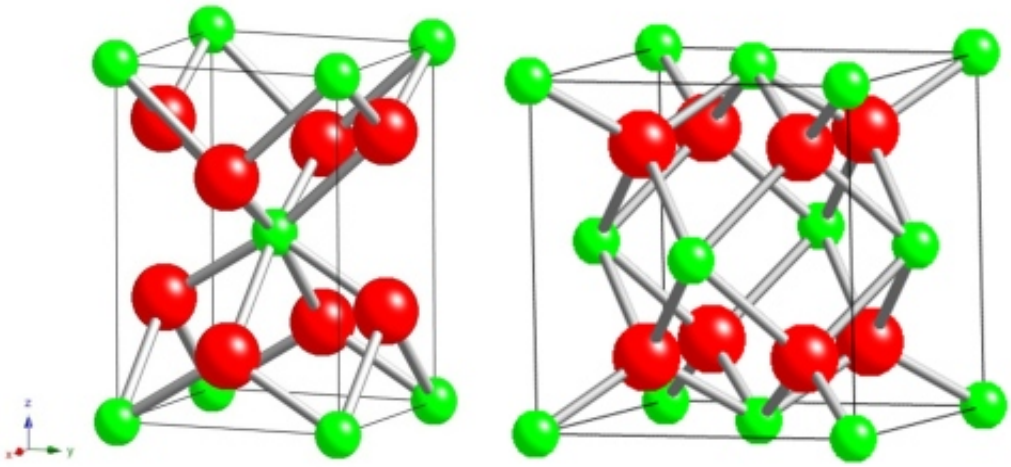

Figure 2.1. Crystal structures of tetragonal YSZ (left) and tetragonal supercell (right). Small green spheres are Zr atoms and large red ones O atoms.

The tetragonal unit cell is primarily used in assigning diffraction peaks, while the direct comparison between the cubic and tetragonal structures can be made when a 'supercell' of the tetragonal structure is used whose *c* axis is parallel and *a* and *b* axes are at 45° to the corresponding axes of the tetragonal cell.[7] The rotation of the axes in the supercell makes them almost parallel to the cubic and monoclinic phase unit cell axes. The lattice parameters for the supercell are *a* = 5.105 Å and *c* = 5.168 Å, which gives *c/a* = 1.012.[6] The *c/a* ratio is commonly used as a measure of 'tetragonality' of a zirconia sample. The positions of the zirconium and oxygen atoms for the tetragonal unit cell and supercell are given in Table 1.

Table 1. Atomic positions for YSZ tetragonal cell and supercell.[6]

		Position	
Atom	Wykoff site	Tetragonal	Supercell
Zr	2a	0,0,0	
	1a		0,0,0
	1b		½, ½, 0
	2g		0, ½, z'[a]
O	4d	0, ½, z[a]	
	8l		x, y, z[a]

[a] z = 0.199, z' = ½, x = y = ¼

When doping zirconia with other oxides, such as Y_2O_3, to achieve stabilization of the high temperature cubic phase, a general mechanism is fairly well understood.[6] The divalent or trivalent cations of the dopant oxide cause a charge imbalance when they are substituted with Zr^{4+}, causing the formation of oxygen vacancies in the lattice. The cations become displaced outward as the oxygen atoms shift closer to the vacancy sites due to their inherent positive charge.

The similar crystallographic structures of cubic and tetragonal YSZ, together with the low scattering ability of oxygen, makes it difficult to distinguish between the two structures using X-ray diffraction techniques. However, the transition from cubic to tetragonal phase occurs through the displacement of oxygen from their ideal sites in the fluorite structure of the cubic phase,[8] and the elongation of the *c* axis in the tetragonal phase.[4] Raman spectroscopy, which is sensitive to the polarizability of the oxygen ions, can be used to clearly identify the presence of both tetragonal and

cubic phase due to the transformation that occurs with the oxygen sublattice.[9] The two distortions give rise to six distinct Raman active modes in the tetragonal phase at approximately 115, 266, 326, 474, 616 and 646 cm^{-1} which can be assigned to the $3E_g$, $2B_{1g}$, and $1A_{1g}$ symmetries (Figure 2.2, adapted from Todorovska[10]). In contrast, the cubic phase is identified by one broad peak in the range of 530 – 670 cm^{-1} which is assigned to T_{2g}, and other poorly defined features as a result of the disorder in the oxygen sublattice, eliminating long range order. [11] It is proposed that the substitution of yttrium for zirconium and the resulting formation of oxygen vacancies cause the oxygens immediately surrounding the vacancies to slightly collapse around the defect.[9] The presence of tetragonal or cubic phase in YSZ materials can be determined using Raman spectroscopy, allowing the degree of stabilization to be determined.

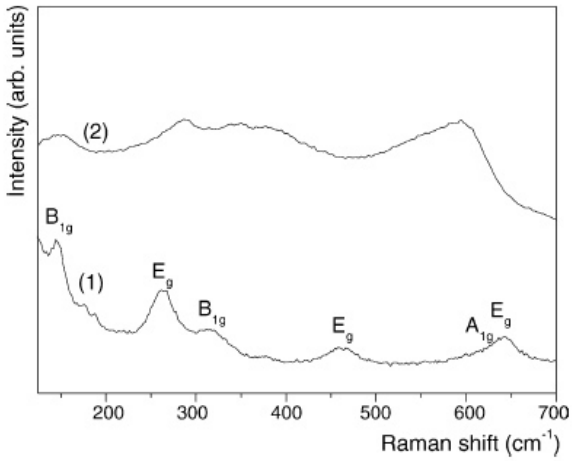

Figure 2.2 Representative Raman spectra of tetragonal (1) and cubic (2) stabilized zirconia. Adapted from Todorovska.[10]

2.4 MAS ^{27}Al NMR

Solid state nuclear magnetic resonance (NMR) is a technique that can be used to investigate the structure of materials on the atomic scale, in particular the local geometry and coordination environments of atoms, and can be applied for both ordered (single crystal) and disordered (amorphous) systems. ^{27}Al is one of the most thoroughly studied nuclides. With a spin of I = 5/2, ^{27}Al has a non-spherical distribution of nuclear electrical charge. This anisotropic distribution results in a nuclear electric quadrupole moment in addition to the magnetic dipole moment. This makes the nucleus interact not only with the applied magnetic field but also the electric field gradients present at the nucleus.[12,13] The presence of quadrupole interactions causes displacement from the isotropic chemical shift as well as peak broadening and distortion. In order to negate these effects, ^{27}Al spectra are often acquired at the highest possible field strength along with being coupled with magic angle spinning (MAS) to narrow the ^{27}Al resonances. In the case of nuclei with spins greater than ½, MAS helps reduce the second order effect on the central transition due to quadrupole coupling, however this effect can not be completely eliminated even under very rapid magic-angle spinning. It is generally accepted that the “true” isotropic shifts for ^{27}Al are usually displaced to more positive values (less shielded) than reported ^{27}Al peak positions.[12]

For the scope of this thesis, MAS ^{27}Al NMR was used for the phase confirmation for the porous alumina (Al_2O_3) products. Alumina materials made from the sol-gel route, or dehydration of boehmite (AlOOH), can form four possible phases: gamma (γ), delta (δ), theta (θ), or alpha (α). γ-Alumina is the desired phase for the porous materials presented, as a density increases is observed with the transition to subsequent phases. The crystal structure of γ-alumina has been presented in Chapter 1. The shifts observed in ^{27}Al NMR are strongly dependant on the coordination environment of Al and the nature of the coordinating atoms. In the case of Al-O environments, there is a distinguishable separation between the chemical shifts for 4-, 5- and 6-coordinated Al.[12] Al in a 4-coordinated environment gives rise to a shift occurring around 50 to 80 ppm while the shift for 6-coordinated Al is from –10 to 15 ppm. The chemical shift for 5-coordinated Al falls in between around 30 and 40 ppm. The structure of γ-alumina has both tetrahedral and octahedral aluminum sites while α-alumina contains only octahedral aluminum sites and hence the two phases can be easily be distinguished by the presence or absence of the chemical shift in the region from about 50 to 80 ppm (Figure 2.3). The identification of the highly desired penta-coordinated aluminum ions, whose coordinatively unsaturated structure provide catalytic reactive sites, can be difficult due to the previously discussed peak broadening and side band formation and requires the acquisition of a high resolution spectra.

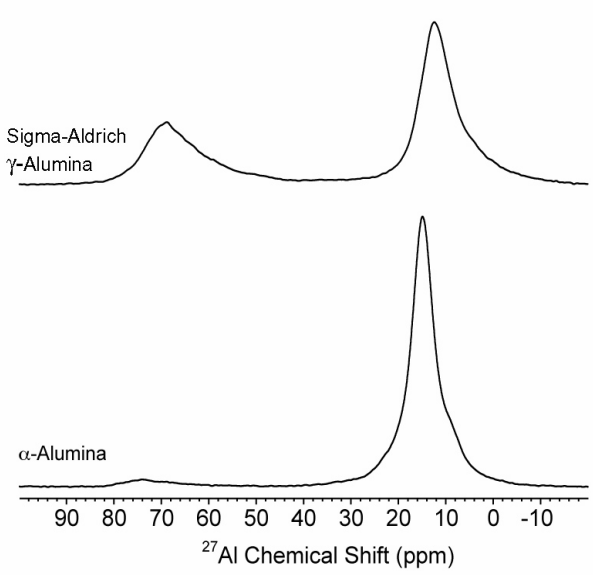

Figure 2.3. MAS ^{27}Al NMR of commercially available γ – Al_2O_3 and α – Al_2O_3.

2.5 Electron Microscopy

Electron microscopy can be used to examine the microstructure and homogeneity of surfaces using lower energy electrons in scanning electron microscopy (SEM), as well as the nanostructure, primary particle morphology, size, and crystallinity through the use of higher energy electrons in transmission electron microscopy (TEM). The strikingly high resolution achieved in TEM is due to the de Broglie wavelength of electrons that is shorter than that of photons used in optical microscopes. Furthermore, the electron's low mass and negative charge allows an electrostatic interaction with the electrons in the inspected material, causing electron scattering.[14] These scattering events create a diffraction pattern that can be used to identify the crystal structure and crystalline nature of a material. TEM and SEM were both used to examine the micro-

and nano-structures of the materials and also to verify primary particle size and crystallinity.

Bright-field TEM imaging is commonly used for the imaging of the bulk or “gross” morphology, mesoparticle size and morphology as well as the determination of atomic ordering of aerogel materials.[15] By defocusing the image so that Fresnel fringes are observed, which are due to an interference effect of the electron plane waves, individual particles within the structure can be easily seen. The multi-dimensional structure of aerogel-like materials will cause the fringing to appear at different focus settings relative to the depths of the particles being examined. This can be exploited by taking a set of through-focus images which will go through underfocus, Gaussian focus, and over focus conditions and allow the connectivity of the particles to be easily imaged. Aerogels exhibit a very unique gross morphology which consists of bonded nanoparticles that form a bicontinuous, multidimensional nanoscale porous network, as schematically shown in Figure 2.4. It is expected that the highly porous materials presented in this work will possess a similar aerogel-like structure, which can be easily confirmed through TEM studies.

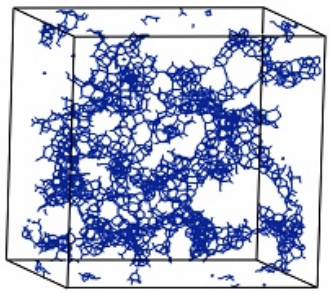

Figure 2.4. Schematic drawing of 3D aerogel structure

Selected-area diffraction can be used to determine the structural ordering of the porous materials. Diffraction patterns of amorphous porous materials will show diffuse rings, while materials with crystalline 2 – 100 nm diameter particles will produce sharp rings. Crystalline porous materials with crystallite diameters greater than 100 nm will produce diffraction patterns with sharp spots.[15] The diffraction patterns, which are formed "pictures" of the distribution of the scattered electrons, are directly related to the specific spacing in the crystal through Equation 2 where R is the measured distance between diffraction spots on the diffraction pattern, λ is wavelength of incident electrons, L is the camera length and *d* is the corresponding crystal spacing.[14] For crystalline materials, the defined spotted diffraction pattern can be used to determine the *d*-spacing.

$$Rd = \lambda L \qquad \textit{Equation 2}$$

In polycrystalline or nanocrystalline materials, the sharp rings seen in a diffraction pattern are formed due to the shape effect, causing broadening of the reciprocal lattice points. In amorphous materials the probability function that defines the locations of neighboring atoms is not uniform on long range, resulting in broad diffraction rings.[14]

The size, shape and connectivity of the primary particles are strongly dependent of the synthetic conditions and precursors, as well as the actual chemical composition of the produced materials. For example, YSZ aerogels and xerogels show very different gross morphologies,[16] while varying between an aluminum chloride and aluminum nitrate

precursor changes the shape of the primary particles in γ-alumina aerogels.[17] The morphological homogeneity, particle connectivity and particle size greatly influence the overall structural properties of highly porous materials, such as aerogels and the materials presented in this wok, making electron microscopy key in the understanding and investigation the structure of such materials.

2.6 Gas Sorption Studies

The use of volumetric physisorption to analyze the surface area and pore properties of porous materials is a well established method, with the chosen gas adsorbate dependent of the type of material being analyzed and pore properties. For all the presented materials, it is assumed based on previous synthesis reports that the newly formed materials will exhibit mostly mesoporous character. A volumetric method was used to measure the adsorption isotherm. For this method of analysis the material being studied is held at a constant temperature (77 K) while known volumes of adsorbate (nitrogen) is introduced. Once the system has reached equilibrium, the pressure is measured.[18] The volume adsorbed is plotted versus the adsorptive pressure, which is expressed as a ratio of the adsorptive pressure over the standard vapor pressure over the bulk liquid, resulting in an isotherm which can then be used to calculate surface area and pore properties using various mathematical models. Nitrogen gas sorption studies were performed on all produced materials and Braunner-Emmett-Teller (BET) specific surface area,

Barrett-Joyner-Halenda (BJH) pore distribution plots and average pore diameter are reported. A brief description of these models will be given, as a full review of all the possible applied analysis mathematical models is outside the scope of this thesis.

The variation of adsorbate-adsorbent interactions as well as the pore geometry gives rise to varying shapes of isotherms, which can be classified into six different types as defined by deBoer, Brunauer, and Gregg (Figure 2.5).[18-20] Microporous materials give Type I, while non-porous or macroporous materials with high energy of adsorption give Type II. Type III isotherms are indicative of non-porous or macroporous materials with low energy of adsorption. Type IV and type V isotherms are both characteristic of materials with mesoporosity with high and low energy of adsorption respectively. Type IV isotherms can be attributed the material having multiple pore sizes.

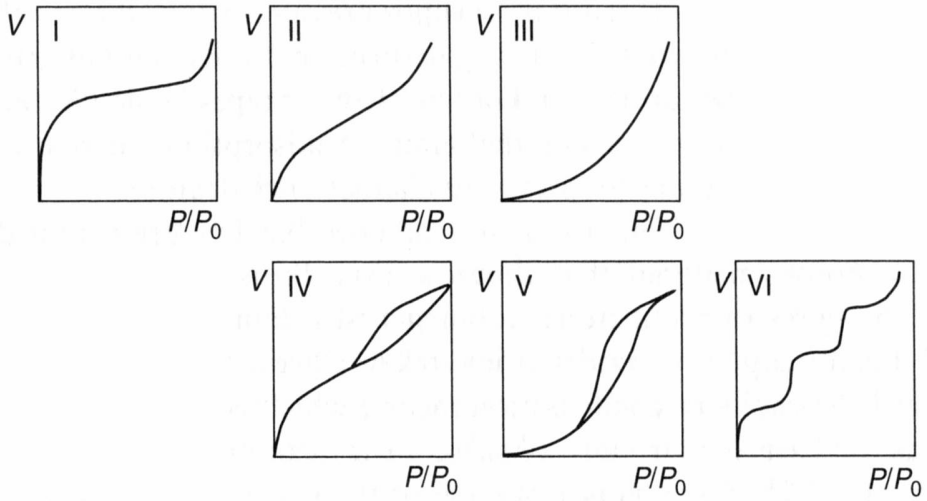

Figure 2.5. Adsorption isotherm types.

The mesoporous materials discussed in this work are generally characterized by a Type IV isotherm. Initially, monolayer adsorption begins and all adsorbed molecules are in contact with the surface of the material causing an initial sharp increase in quantity adsorbed over a small range of relative pressures (~ 0 – 0.1), forming a characteristic "knee" at low relative pressures.[20] Once monolayer adsorption is complete and multilayer adsorption begins, a slower increase in quantity adsorbed is observed with increasing partial pressure as not all of the adsorbate molecules are in contact with the surface. At a critical adsorbate film thickness, capillary condensation begins, filling the residual pore space with condensate and the formation of a meniscus occurs. As the pores continue to be filled, a steep increase in amount adsorbed over high partial pressures is observed until saturation is reached. The presence of macropores can be verified by a sharp increase in quantity adsorbed as the relative pressure reaches 1. During the desorption process, evaporation of the condensate inside of the pores occurs by the thinning of the liquid meniscus and adsorbed layers. The condensation and respective evaporation are both processes that are strongly dependent of adsorbate-adsorbate and adsorbate-pore wall interactions which are influenced by pore size, pore geometry, and surface energy of the adsorbent. If these interactions are significantly different between adsorption and desorption, then a hysteresis is observed. Different pore shapes can be identified by various hysteresis shapes.

Specific surface area was determined assuming the BET mathematical treatment.[19] The method for determining specific surface area of a material (*S*) is given in Equation 3, where the volume of gas adsorbed when the entire surface of the material has monolayer coverage (V_m) is unknown. The average area occupied by one molecule of adsorbate in a monolayer and the molar volume of gas at STP are A_m and V_M respectably.

$$S = \frac{V_m N_A A_m}{V_M} \qquad \textit{Equation 3}$$

The BET model is used to solve for V_m (Equation 4) where the volume adsorbed in the relative pressure rage of 0.05 – 0.35 (the region wherein surface coverage is approximately 100%) for high energy surfaces such as silica and alumina. In this model, *V* is the volume of gas adsorbed at STP, V_{mon} is the volume of gas required for a monolayer and *C* is a constant which describes the attraction forces of the adsorbed molecules to each other and to the surface of the material.[18]

$$\frac{V}{V_{mon}} = \frac{C_x}{(1-x)[1+(C-1)x}, \qquad \text{where } x = \frac{P}{P_s} \qquad \textit{Equation 4}$$

The mesoporosity of the materials was determined using the BJH model which calculates the average pore size and total pore volume by dividing the range of pore sizes into groups that then have a collective average size.[20] The total pore volume is derived from the amount of vapor adsorbed when all pores are filled with condensed adsorbate, near a

relative pressure of 1. BJH analysis calculates the average pore size and pore volume based on the emptying of mesopores over a step-wise reduction of relative pressures, examining two critical steps; the evaporation of the pore core volume and the evaporation of the adsorbed layer. The critical relative pressure that pores lose their "core", which is defined as the volume of condensed adsorbate which evaporates all at once when the critical pressure for that radius is reached, is determined by the Kelvin equation (Equation 5). The Kelvin radius of a pore, r_K, is calculated from the gas-liquid surface tension, γ, volume of one mol of condensate at temperature T, V_{mol}, and the contact angle between the liquid and pore wall, θ.[18]

$$r_K = \left(\frac{-2\gamma V_{mol} \cos\theta}{RT \ln\left(\frac{P}{P_o}\right)} \right) = \frac{k}{\ln\left(\frac{P}{P_o}\right)} \qquad \textit{Equation 5}$$

The thickness of the adsorbed layer in each pore is calculated using the thickness equation (Equation 6) in which V_a is the volume of adsorbed gas, V_m is the volume of gas for a monolayer, and τ is the thickness for a monolayer.

$$t = \frac{V_a}{V_m}\tau \qquad \textit{Equation 6}$$

The use of the Kelvin and Thickness equation allows the amount of adsorbate lost in a desorption step to be related to the average size of pores that empties during that particular step, resulting in the

determination of pore size distribution with respect to pore volume. From this, cumulative pore volume and average pore size can be calculated for the range of pores 1.5 – ~100 nm in size due to the limitations of the instrument employed.

BJH analysis is not the most ideal for mesoporous materials with a wide range of pore sizes and all calculated values must be understood to be mathematical estimations under drastic assumptions on the actual conditions of the studied material. The first assumption made using this model is that all of the pores are rigid and have a regular shape, which is only true for ordered porous materials. The second assumption is that the thickness of an adsorbed film inside of a pore is equivalent to that on a flat surface, ignoring any interactions that arise due to the proximity of adsorbed films to each other inside of the pores. Thirdly, BJH analysis assumes that there are no micropores. Lastly, the assumption is made that size distribution does not extend continuously from the mesopore range to the macropore range, meaning that a plateau must be observed in the adsorption isotherm as the relative pressure approaches 1.

The majority of the assumptions made in the BJH analysis model deviate from the actual conditions of materials being analyzed. The materials presented in the proceeding chapters are exhibit disordered porous structures, with irregular pore shape, size, and connectivity. Most of the materials also exhibit a hierarchically porous structure, meaning that their solid walls contain micropores, while the primary particles form a

mesoporous structure with the possibility of macropores forming as well. However, despite the large discrepancies in the assumptions made in the BJH model, it is one of the most well accepted models used currently to report mesoporosity, for both ordered and disordered porous materials. Therefore, in order for ease of comparison with previously reported materials, standard materials, and keeping with the conventionality of gas sorption data and analysis presented in literature, the BJH model will be used for reporting the cumulative pore volume and average pore diameter.

2.7 References

(1) Klug, H. P.; Alexander, l. E. X-Ray Diffraction Procedures; 2nd ed.; Wiley: New York, 1974.

*(2) Holzwarth, U.; Gibson, N. Nature Nanotechnology **2011**, 6, 534.*

*(3) Zhou, R. S.; Snyder, R. L. Acta Crystallographica, Section B: Structural Science **1991**, B47, 617.*

*(4) Teufer, G. Acta Crystallographica **1962**, 15, 1187.*

*(5) Martin, U.; Boysen, H.; Frey, F. Acta Crystallographica, Section B: Structural Science **1993**, B49, 403.*

(6) Southon, P., University of Technology, Sydney, 2000.

*(7) Southon, P. D.; Bartlett, J. R.; Woolfrey, J. L.; Stevens, M. G. Ceramic Transactions **1998**, 81, 75.*

*(8) Lefevre, J.; Collongues, R.; Jorba, M. P. y. Compt. rend. **1959**, 249, 2329.*

*(9) Feinberg, A.; Perry, C. H. Journal of Physics and Chemistry of Solids **1981**, 42, 513.*

*(10) Todorovska, R.; Petrova, N.; Todorovsky, D. Applied Surface Science **2005**, 252, 1266.*

*(11) Kontoyannis, C. G.; Orkoula, M. Journal of Materials Science **1994**, 29, 5316.*

(12) Mackenzie, K. J. D.; Smith, M. E. Multinuclear Solid-State NMR of Inorganic Materials; Elsevier Science Ltd: Kindlington, Oxford, 2002.

(13) Duer, M. J. Solid-State NMR Spectroscopy; Blackwell Publishing Ltd: Oxford, UK, 2004.

(14) Williams, D. B.; Carter, C. B. Transmission Electron Microscopy: A Textbook for Materials Science; Plenum Press: New York, 1996; Vol. 1.

*(15) Stroud, R. M.; Long, J. W.; Pietron, J. J.; Rolison, D. R. Journal of Non-Crystalline Solids **2004**, 350, 277.*

*(16) Chervin, C. N.; Clapsaddle, B. J.; Chiu, H. W.; Gash, A. E.; Satcher, J. H., Jr.; Kauzlarich, S. M. Chemistry of Materials **2006**, 18, 4865.*

*(17) Baumann, T. F.; Gash, A. E.; Chinn, S. C.; Sawvel, A. M.; Maxwell, R. S.; Satcher, J. H., Jr. Chemistry of Materials **2005**, 17, 395.*

(18) Condon, J. B. Surface Area and Porosity Determinations by Physisorption; Elsevier: The Netherlands, 2006.

*(19) Brunauer, S.; Emmett, P. H.; Teller, E. Journal of the American Chemical Society **1938**, 60, 309.*

(20) Volosin, A., Surface Area and Pore Measurement in Porous Materials.

CHAPTER 3

PREPARATION OF HIGHLY POROUS GAMMA ALUMINA VIA COMBUSTION OF BIORENEWABLE OIL

3.1 Introduction

Highly mesoporous, transparent γ-alumina particulates were successfully prepared using the non-alkoxide sol-gel based synthesis and high temperature combustion method discussed in Chapter 1. Upon using a pristine or biorenewable oil, the new method affords high porosity (80 – 88 %), high surface area (295 – 375 m^2/g) γ-alumina products with controlled pore sizes (average pore diameter = 11 – 21 nm), by achieving rapid solvent removal and calcination *simultaneously* through a single combustion step. The products were characterized by elemental analysis, powder X-ray diffraction, solid-state NMR, and high-resolution transmission electron microscopy with selected area electron diffraction for morphology and structure identification, and ATR-IR spectroscopy for surface chemistry and functional groups, and nitrogen adsorption/desorption analysis for pore properties. The promising results indicate that the new method may be suitable for high-volume production of highly porous metal oxides with aerogel-like pore architectures.

Porous, high surface area γ-Al_2O_3 materials are widely used in catalysis applications in the chemical and petrochemical industry, such as the cracking and hydrocracking of petroleum, and the steam reforming of hydrocarbon feedstocks.[1-3] as well as separation applications.[4]

Compositional, surface area, and porosity control of the material is critical for these applications. Sol-gel synthesis is one of the most popular synthetic routes for the production of alumina materials and has been utilized since initial inception by Yoldas in 1973.[5] Yoldas observed that the catalyzed hydrolysis and condensation of aluminum alkoxide precursors resulted in the formation of solid alumina wetgels that then could be dried to form porous transparent alumina materials. [6-8] Since Yoldas' work, aluminum alkoxides have been the most popular precursors for sol-gel synthesis of alumina materials until recently, when Baumann *et. al.* were able to obtain transparent alumina aerogels using aluminum salts as precursors.[9] After being solvated in water, Al(III) cations form a hexahydrated complex which acts as an acid, forming hydroxylated species that undergo condensation through olation and oxolation reactions.[10] As the pH is slowly and uniformly increased with the aid of an epoxide that acts as a proton scavanger, polynuclear species precipitate out of solution and the condensed solid phase spans the volume of the solution, forming a complete solid gel.[9]

Two parameters that strongly influence the structure and mechanical strength of the resulting aerogel material are the anion of the aluminum salt precursor and the solvent used during the sol-gel synthesis. The hydrolysis and condensation of the hydrated aluminum species as well as the aggregation of the colloidal particles is affected by the complexing character of the salt anion, changing the final primary particle

morphology. Also, the nucleophilicity of the anion towards the protonated epoxide varies depending on the solvent used, causing a large variation in gelation time. It has been found that $AlCl_3 \cdot 6H_2O$ in a 50/50 by volume H_2O/ethanol solution afforded less dense and more mechanically robust aerogels due to the interconnected, fiber-like particles that formed a weblike microstructure.[9] The work done by Baumann and co-workers systematically examines the variation of aluminum salt precursors and solvents in an alkoxide free synthesis of alumina aerogels and therefore will not be covered further within the scope of this chapter.

Another challenge facing the non-alkoxide sol-gel synthesis of non-silicate metal oxides is the significant amount of water in the pores and in the solid component present from the precipitation of metal oxides from an aqueous solution The dried inorganic gels are typically metal oxo-hydroxides or hydrated metal oxides with poor crystallinity, rather than the targeted crystalline metal oxides, although they may have a very high surface area even when dried under ambient conditions.[11-13] For crystalline metal oxide products, a subsequent heat treatment through calcination is required to drive off the crystal water and/or hydroxyl groups and to provide crystallinity, but this often induces pore collapsing.[11,14] It would be desirable to find a method that avoids time/energy-intensive drying processes and achieves rapid removal of the pore liquid and calcination of the inorganic solid component *simultaneously* producing

high surface area, porous γ-Al_2O_3 materials that are comparable to aerogels.

3.2 Experimental Section

3.2.1 Synthesis of Porous γ-Al_2O_3

The preparation of the initial wet alumina gels followed the inorganic precursor method described by Baumann et al. in which $AlCl_3 \cdot 6H_2O$ is employed as an aluminum ion precursor for alumina aerogel preparation.[9] In order to examine the effect of the precursor concentrations on the pore characteristics, six samples (a – f) were prepared with different Al^{3+} concentrations from 0.46 to 1.23 mol/L (Table 1). The 0.61 mol/L concentration (sample b) corresponds to the one employed by the chloride precursor method by Baumann et al. The experiments were performed also for the precursor concentrations lower than 0.46 mol/L but did not provide satisfactory results. In a typical procedure, a proper amount of $AlCl_3 \cdot 6H_2O$ (Sigma-Aldrich, 99%) was dissolved in 20 ml of a 50/50 volume mixture of deionized water and absolute ethanol (Decon Laboratories, Inc.). Propylene oxide (PO) (1,2-epoxypropane, Sigma-Aldrich, 99%) was then added to the clear solution in a molar ratio of Al^{3+}:PO of 1:10 and stirred for 10 min. The reaction was exothermic and after stirring the solution had a pH around 2. The solution was then kept at room temperature for gelation which took place typically within 3 hours as the pH gradually reached 5. After three days of aging in

a closed container, the gel was broken into smaller pieces of *ca*. 1 cm^3 in size and placed in a dimethyl sulfoxide (DMSO) (Sigma-Aldrich, 99.9%) bath for three days. Castor oil is miscible with DMSO, tetrahydrofuran (THF) and alcohols. The gel pieces were then transferred to a castor oil (The Chemistry Store.com Inc., Cayce, South Carolina, Catalog No. 51006-5) bath at 50 ºC for three days while occasionally stirring to ensure the homogeneity of the olegel. The soaking periods for water/ethanol–DMSO and DMSO–oil exchange steps were chosen to ensure full exchange and may be shortened if desired. Upon soaking in DMSO, the gels remained rigid during the solvent-exchange period. Long-term effect of DMSO on the gel structure was not examined. However, it is mentioned that the gels slowly dissolve in DMSO upon heating at about 80 ºC. As the oil replaced DMSO in the gel, the gel became much harder probably due to the high viscosity of the oil. The oil-soaked gel (olegel) pieces were then taken out from the oil bath and placed evenly on a hot plate at about 700 ºC. The olegel pieces ignited instantly with a large flame and broke apart into particulates. The flames ceased within three to six minutes and the product was then heated at 700 ºC for 10 hours in air in order to ensure the complete burn-off of any carboneous species. Alternatively, the removal of the carboneous species could be completed under oxygen flow at temperatures as low as 500 ºC for less than three hours, without affecting the crystallinity of the final products.

3.2.2 Physical Characterization

High-resolution transmission electron microscopy (HRTEM) was performed on a Hitachi HNAR-9000 TEM (LaB_6 source, accelerating voltage 300kV, Scherzer resolution 0.18 nm). The TEM samples were prepared by first grinding in an agate mortar in ethanol and ultrasonically dispersed for 10 minutes. A drop of the solution was deposited on a copper grid covered with a holey carbon film and dried on a hot plate in air. The images were taken under bright field conditions and slightly defocused to increase contrast. Selected area electron diffraction (SAED) pattern of products was also collected from TEM studies.

Particle size, phase information, and crystal structure were determined using powder x-ray diffraction, collected using a Siemens D5000 diffractometer with Cu Kα radiation. MAS ^{27}Al NMR spectroscopic studies for phase identification as well as coordination environment of Al(III) species, were carried out at the resonance frequency of 800 MHz with a rotation frequency of 60 kHz, using Varian Dual Solids/Liquids NMR Spectrometer. The presence of organics through the entirety of the synthesis was monitored using attenuated total reflectance infrared (ATR-IR). These spectrometic studies were conducted on a Thermo Nicolet 380 FT-IR Spectrometer with a Smart Orbit accessory equipped with a diamond crystal plate. Elemental analyses were performed with Perkin-Elmer 2400 Series II CHNS/O Analyzer in order to estimate with the amount of residual carbon in the products.

Brunauer-Emmett-Teller (BET) surface areas were measured with a Micromeritics ASAP 2020 volumetric adsorption analyzer with nitrogen as the adsorbate at 77 K. Prior to the analysis, samples weighing around 100 mg were degassed at 350 ℃ for at least 10 hours under vacuum until a residual pressure of ≤ 10 μmHg was reached. Specific areas were calculated according to the BET equation, using nitrogen adsorption isotherms in the relative adsorption range from 0.06 to 0.2. For the calculation of pore size distribution, the desorption branch was considered and the pore volume was obtained from the amount of nitrogen adsorbed at a relative pressure of 0.99. Mesopore size distributions were obtained using the Barrett-Joyner-Halenda (BJH) method assuming a cylindrical pore model.[15]

3.3 Results and Discussion

3.3.1 Synthesis

Figure 3.1 illustrates the overall synthetic procedure.[16] As in typical sol-gel based porous materials synthesis, our new method starts with the formation of an inorganic wet gel and subsequent solvent-exchange steps. Unlike in those methods that rely on drying as the way of subsequent pore liquid removal, however, the new method employs a combustion process which removes a high boiling point organic liquid, castor oil, by burning. The original liquid is first replaced by an oil-miscible solvent, DMSO.[17] The solvent is then replaced by an oil to produce an oil-soaked gel (called

"olegel" hereafter). In order to remove the oil from the gel pores, the olegel is quickly heated and combusted. The vegetable oil or plant oil does not evaporate significantly before ignition, which avoids serious gel shrinkage and pore collapsing during heating. This combustion dehydrates/crystallizes the pore wall material *simultaneously* without drastic pore collapsing. The removal of all the carboneous species by the combustion and calcination leaves a highly porous metal oxide product (called "pyrogel" hereafter).

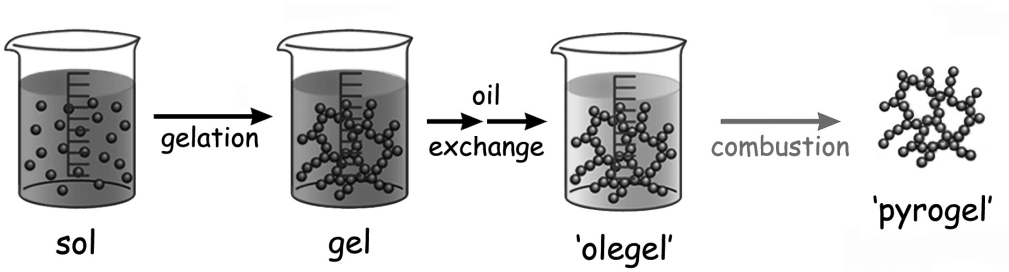

Figure 3.1. Pyrogel process for preparation of highly mesoporous

Figure 3.2a and 3.2b show γ-Al_2O_3 pyrogels that were obtained as glassy (semi)transparent particulates from our experiment. Olegels burn readily, generating large flames, because of the high content of oil in the material. During pyrolysis of oil, the gush of the volatile gases breaks the pyrolyzed olegel pieces into small particulates with a broad size range from several hundred microns to a couple of millimeters. After complete combustion, the individual particulates are transparent under microscope (Figure 3.2b). Such syntheses were repeated several times, confirming

the reproducibility of the process in terms of both the aforementioned physical characteristics and other nature of the materials described henceforth. The elemental analysis shows that the residual carbon content is less than 0.25 wt% for the samples and this proves that the oil can be burned off almost completely without leaving any significant amount of carboneous substances in the products. The substantial transparency is due to the absence of grain boundaries which results in low light-scattering. The glassy, granular form of the products can be well suited for industrial processes unlike the powder form, which may possess drawbacks, such as dusting and high pressure-drops.[2]

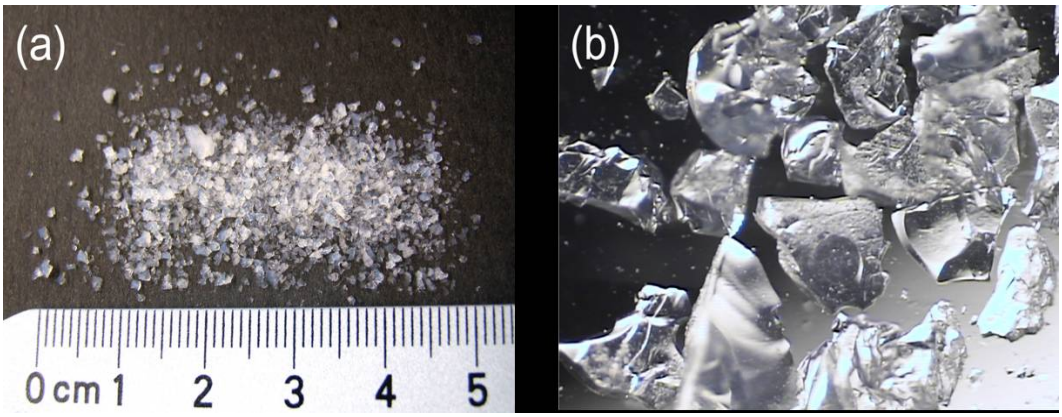

Figure 3.2. γ-Al_2O_3 pyrogel particulates (sample a) (a) under a room light and (b) under microscope. The big particulates around the center of (b) are about 0.5 mm in length.

3.3.2 Powder X-ray Diffraction

All the six samples exhibit similar patterns regardless of the initial precursor concentrations, and the powder XRD pattern of the lowest-concentration Sample a is shown in Figure 3.3. The initial wet gels and

olegels were amorphous based on the absence of any discernable diffraction peaks in their powder XRD patterns. After the combustion, all the pyrogel products show broad Bragg reflection peaks in the XRD pattern, indicating some crystallinity. All the Bragg reflection peaks were assigned to the structure of γ-Al_2O_3 (ICDS 66559).[9,18,19]

The γ-Al_2O_3 structure is typically described as a defect spinel structure with varied degrees of a tetragonal distortion (*c/a* = 1 ~ 0.985) which depend on the heating condition.[20,21] The broadening of the Bragg peaks is caused by the disordering of the aluminum ions particularly at the octahedral sites as well as the small particle sizes. Because of the face-centered cubic close packing of oxide ions, the (400) and (440) reflections tend to dominate the XRD pattern.[9] In Figure 3.3, the (400) and (440) reflections of the spinel are neither split into two peaks, nor apparently asymmetric, which indicates that the products do not exhibit a strong tetragonal deformation. The result positively excludes as a possible candidate the δ-Al_2O_3 structure whose so-called “three spinel blocks structure” develops more extensively with a greater tetragonal distortion and gives additional Bragg reflections due to the superstructure formation.[20,21] The (400) and (440) reflections in Figure 3.3 are sharp and comparable to the ones reported for the γ-Al_2O_3 aerogels in the literature.[9,19]

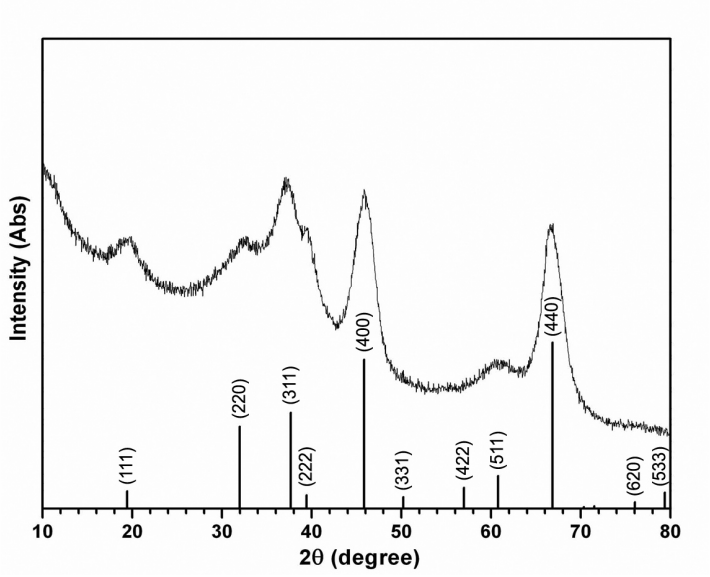

Figure 3.3. Powder X-ray diffraction pattern of γ-Al_2O_3 pyrogel (sample a) compared with calculated Bragg reflection peaks (solid vertical lines) (ICSD 66559)

3.3.3 Electron Microscopy

Transmission electron microscopy was used to evaluate the microstructure of the alumina pyrogels (Figure 3.4). The microstructure of the six products exhibits a common "textural porosity" arising from three-dimensional interconnection of rod-shaped particles, 2 – 5 nm in diameter and of varying lengths. The homogeneity of the morphology and particle size was confirmed by examining several areas of the TEM grid for each sample. The observed particle sizes and pore structure, described as a "weblike" architecture, are consistent with the previous report on γ-Al_2O_3 aerogels which were prepared from the same chloride salt precursor route.[9] Such a weblike microstructure has been considered to provide enhanced mechanical integrity to the low-density aerogel materials.[22]

Despite the high porosity, the pyrogel products did not break upon repeated immersion in liquids such as water, alcohols and hexane, indicating that they can be utilized in catalytic applications that involve liquid solutions. This is in contrast to typical metal oxide aerogels that are prone to pore collapsing due to capillary pressure and lose their porosity significantly.[3,23] Lattice fringes are visible in the higher magnification image (Figure 3.4b), which indicates that the particles are crystalline in nature, consistent with the XRD patterns. The SAED patterns (Figure 3.4c) show intense (400) and (440) reflections and other weak ones. The reflections (311), (400), (440) and (444) appear at 2.36, 1.94, 1.36 and 1.12 Å respectively, and this is in agreement with the theoretical *d*-spacing of those reflections for the cubic γ-Al_2O_3 structure (2.39, 1.97, 1.40 and 1.14 Å) with the powder XRD pattern in Figure 3.3.

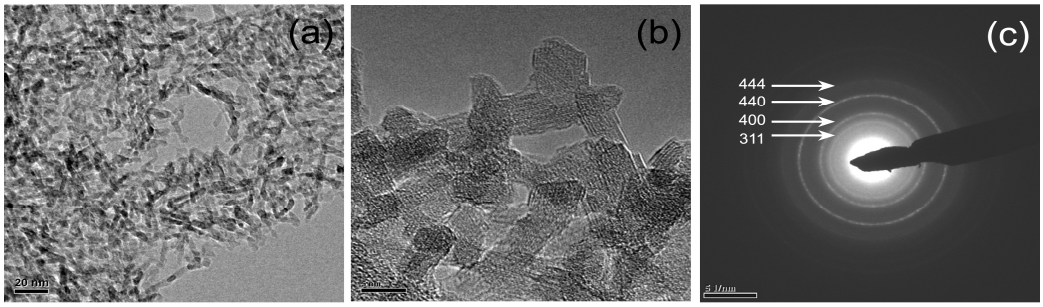

Figure 3.4. (a), (b) Transmission electron micrographs and (c) selected area diffraction (SAED) pattern of γ-Al_2O_3 pyrogels (sample a) (scale bar = 20 and 5 nm for (a) and (b), and 5 nm^{-1} for (c)).

3.3.4 Surface Area and Porosity Analysis

The surface areas, average pore diameters and pore volumes for the alumina pyrogels were measured using nitrogen adsorption/desorption

methods (Table 1). The estimated BET surface areas range from 295 to 375 m^2/g, mostly contributed from mesopores, and do not depend significantly on the precursor concentration changes. For the samples a to c in the low precursor concentration range (0.46 – 0.77 mol/L), the average pore diameter (17 – 21 nm) and cumulative pore volume (1.6 – 2.0 cm^3/g) increase as the precursor concentration decreases, indicating that the new method may allow control of pore sizes to some extent. In the high concentration region (samples d – f), however, such correlation is not seen, while all the samples d – f have a lower porosity than the samples a – c in the low concentration region.

A volume porosity of 80 – 88 % is estimated roughly from the pore volumes and the theoretical density of γ-Al_2O_3 as described above. The results are comparable to what have been reported for γ-Al_2O_3 aerogels that were prepared through supercritical drying and subsequent calcination.[9,19] In particular, the 88 % porosity of the sample a, from the lowest precursor concentration, compares well with the 89 % porosity of the calcined γ-Al_2O_3 aerogels reported from the same chloride precursor method (the porosity was estimated from the pore volumes and the theoretical density of γ-Al_2O_3). Their average pore diameters are also very much comparable to each other (21 nm vs. 22 nm). The pore volumes are larger than what has been observed for the commercial γ-Al_2O_3 (pore volume of 0.1 – 1.2 cm^3/g) which have relatively small pore sizes (2 – 10 nm).[24] Although still significantly high, the maximum surface area of the

pyrogels is somewhat lower than that of the reported aerogel (max. 375 vs. 431 m^2/g). This discrepancy can be due to the different extent of particle sintering or differing amounts of micropores. For the sample a, the micropores contribute about 10 % to the total BET surface area. The micropore contribution for the reported γ-Al_2O_3 aerogel was not given. Further optimization of the synthetic parameters may afford higher porosity products with higher surface areas.

Table 1. Selected Properties of γ-Al_2O_3 Pyrogels.

sample	Al^{3+} precursor concentration (mol/L)	BET surface area (m^2/g)	BET surface area from micropores[a] (m^2/g)	BJH desorption average pore diameter[b] (nm)	BJH adsorption cumulative pore volume[c] (cm^3/g)
a	0.46	340	35	21	2.0
b	0.61	318	26	19	1.8
c	0.77	327	25	17	1.6
d	0.92	295	16	12	1.1
e	1.07	332	22	13	1.3
f	1.23	375	20	11	1.3

[a]by the use of *t*-plots with the Harkins-Jura model.

[b]4(total pore volume)/(surface area).

[c]from the pores with their pore width no larger than 150 nm.

The adsorption/desorption isotherms for the alumina pyrogels are summarized for the precursor concentrations of 0.46, 0.77 and 1.07 mol/L in Figure 3.5a and 0.61, 0.92 and 1.23 mol/L in Figure 3.5b. The grouping

is solely for the sake of clarity of the figures. All of those can be classified as type IV isotherms, characteristic for mesoporous materials, based on the classification by Brunauer. All the isotherms show an H1-type of hysteresis, with hysteresis loops at higher relative pressures above 0.7, and thus the desorption branch was used to calculate the pore size distribution based on the BJH method (Figure3.6). The hysteresis loop of the sample d is slightly asymmetric with a distant resemblance to an H2-type loop. For highly disordered, connected pore systems, a caution should be exercised in using the desorption branch for the BJH pore size analysis, because the factors that determine the shape of the hysteresis loop are still not completely known.[25]

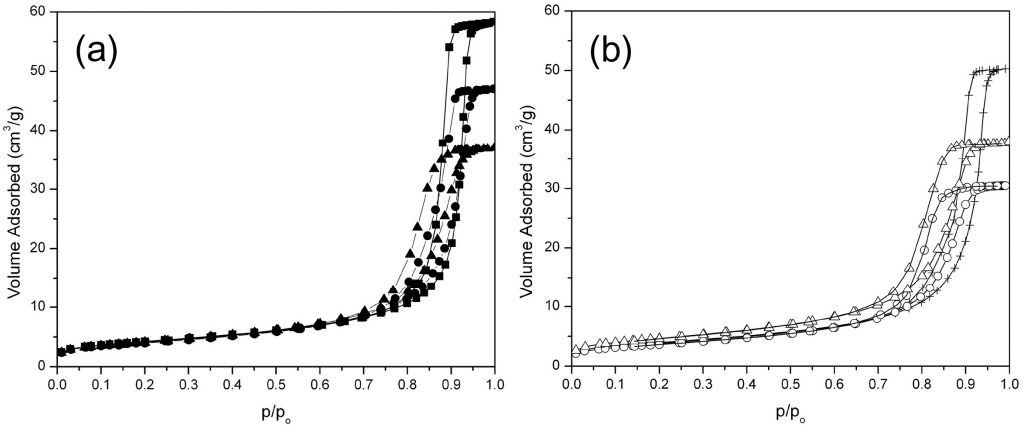

Figure 3.5. Nitrogen adsorption/desorption isotherms of six γ-alumina pyrogel samples a – f. (a) for samples a (■), c (●) and e (▲), and (b) for samples b (+), d (○) and f (△). The calculated *C* values are 133.9, 130.2, 126.4, 114.6, 119.9 and 118.6 from the BET plots.

Nevertheless, the pore size distribution curves in Figure 3.6 show a general trend of pore size increase upon the decrease in precursor

concentration, which is consistent with the trend in the average pore diameter and pore volume as a function of precursor concentration. The curves also indicate relatively narrow pore size distributions and a lack of large pores in the samples.

The hysteresis in the isotherms is typically associated with capillary condensation within mesopores. Therefore, the slight differences in the shape of the hysteresis loops of the pyrogel samples are related to the delicate variations of the structure of the mesopore network.[9,25] The observation of the H1- or H2-type hysteresis for the pyrogels is not in agreement with the H3-type hysteresis reported for the alumina aerogels from the same chloride salt precursor method.[9] In ordered pore systems very often the H1-type hysteresis occurs, whereas the H2- and H3-type hysteresis is typically observed for disordered mesoporous systems. Unlike the other types, the isotherms with the H3-type hysteresis do not show limiting adsorption at high relative pressure and their desorption branch contains a steep region at the relative pressure between 0.4 and 0.45. The H3-type hysteresis is prevalent among non-rigid aggregate structures made of plate-like plates giving rise to slit-shaped pores and can be also due to the presence of a significant amount of macropores. Therefore, the H1-type hysteresis observed in Figure 3.5 indicates that the weblike architecture may not be the main origin of the H3-type hysteresis for the alumina aerogels and that macropores are not significantly present in our samples.

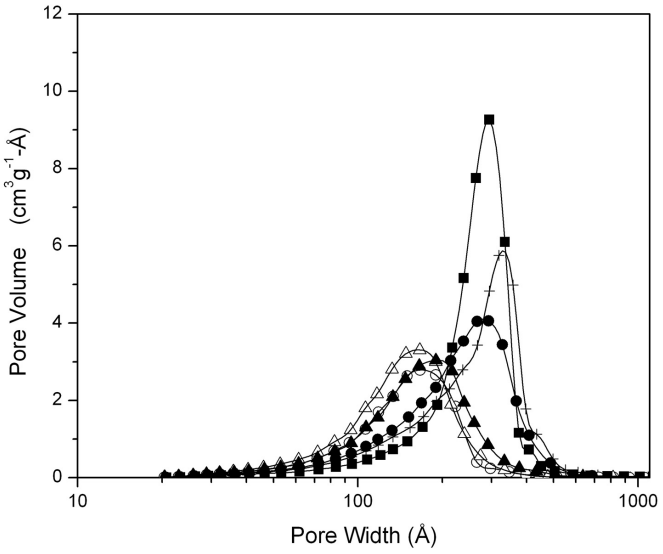

Figure 3.6. BJH pore distributions of six γ-Al_2O_3 pyrogel samples a – f. ■ for a; + for b; ● for c; ○ for d; ▲ for e; △ for f.

3.3.5 MAS ^{27}Al NMR

In order to examine the local structure of the Al^{3+} ions in the alumina particles, the pyrogels were studied using solid state ^{27}Al MAS-NMR along with a reference γ-alumina (Sigma-Aldrich, Product No. 544833, particle size: 40 – 47 nm) (Figure 3.7). ^{27}Al NMR chemical shifts are directly related to the coordination number of the Al^{3+} ion.[9] Chemical shifts for octahedral Al^{3+} units appear between –10 and 20 ppm, while tetrahedral Al^{3+} centers exhibit peaks between 50 and 80 ppm. The spectrum of the alumina pyrogel (Figure 3.7a) is consistent with that of the reference γ-alumina (Figure 3.7b), and exhibits the two peaks centered at 11 and 70 ppm which correspond the tetrahedral and octahedral Al^{3+} species, respectively.[26]

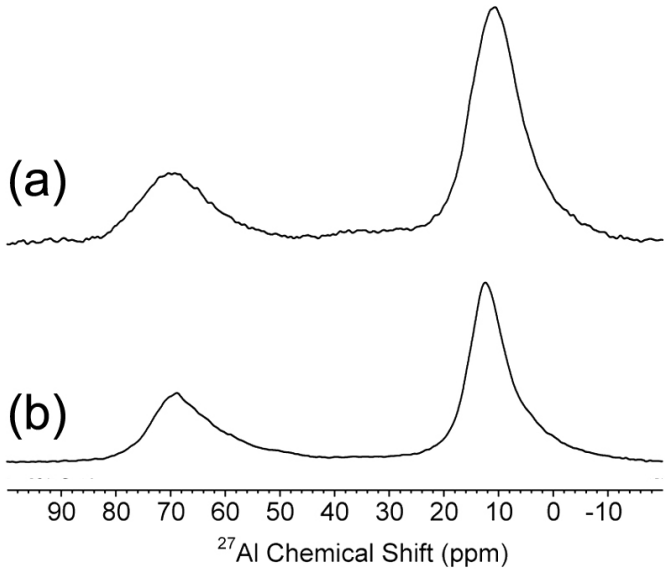

Figure 3.7. 800 MHz ^{27}Al-MAS-NMR spectra of (a) γ-Al_2O_3 pyrogels (sample a), and (b) γ-Al_2O_3 reference at a 60 kHz MAS frequency.

3.3.6 ATR-IR

All the six samples, as well as other samples prepared in the course of the work, showed the same IR spectral features without appreciable differences and we show the spectrum of the sample a in Figure 3.8. The weak-intensity peaks between 1500 and 2500 cm^{-1} appear at different positions and with various but consistently weak intensities among different samples. They could be due to the stretching vibrations of C=C, C≡C and C=O groups in the carboneous materials (< 0.25 wt%) present in the samples. Incompletely calcined/dehydrated alumina particles can exhibit relatively well-developed absorptions peaks between 1300 and 2300 cm^{-1},[27,28]. The lack of such absorption peaks in

Figure 3.8 suggests that the calcined samples do not contain an appreciable amount of hydroxyl species in the crystal lattice, although their presence on the pore surfaces cannot be excluded. This is not in disagreement with the observation from the XRD studies and we suspect that the pyrogel process may be well suited for gel calcination in γ-Al_2O_3 preparation. The rapid burning of the oil inside the gel pores may not be disadvantageous in achieving proper heating in nanoscale.

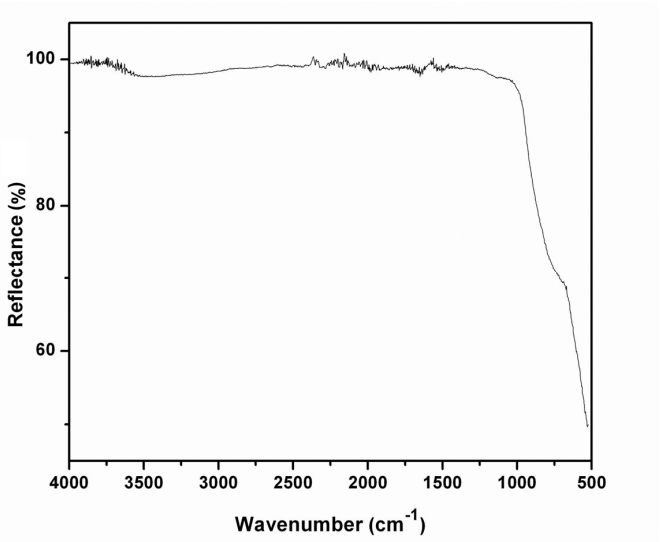

Figure 3.8. An ATR-IR spectrum of γ-Al_2O_3 pyrogel (sample a).

3.3.7 Oil Combustion and Olegels

The choice of the castor oil is based on its propensity to thermally polymerize and its relatively high viscosity (232 cP at 40 °C) in comparison to other biorenewable oil (25 – 40 cP at 40 °C).[29-31] Castor oil, an unconjugated oil, is roughly 87 % triglyceride of ricinoleic acid which has a double bond in the C-9 position and a hydroxyl in the C-11.[32] When

heated, it easily dehydrates to become conjugated and thus can polymerize at temperatures as low as 150 °C.[33] These properties lead to slow evaporation/atomization, inefficient mixing with air, oxidative and thermal polymerization, and carboneous deposit formation that are in fact typical in biorenewable oil combustion processes.[34,35] The formation of (semi) solid polymer under oxygen-deprived heating conditions can effectively avoid liquid/gas interfaces during oil burning, minimizing pore collapsing and thus gel shrinkage. Indeed, such thermal polymerization has been exploited successfully in block-copolymer template-based processes for ordered mesoporous transition metal oxides by employing designer polymers which first become more cross-linked rather than decompose when heated.[36] In our other experiments, the low-viscosity unconjugated oils did not work as effectively as castor oil in alumina pyrogel production and yet the products from all the tested oil (soybean oil, corn oil and canola oil) still showed high porosities (typically up to 85 %). However, it must be mentioned that the synthetic condition was not optimized for those oils in those preliminary experiments.

Olegels themselves are unprecedented materials to our knowledge and their detailed calcination mechanism will be studied in due course. The combustion of the olegels was found to take five to six times longer than what we observed for the corresponding oil itself. The retarded combustion is understandable considering that the well-known low thermal conductivity of aerogels is partly due to the slowed gas diffusion through

the pore network.[37,38] That is, evaporation of the oil and oxygen diffusion must take place through the tortuous gel network and hence become delayed significantly. The oxygen-deprived heating leads to thermal polymerization of the oil, and subsequent char formation in the pores should be helpful in minimizing formation of liquid/gas interfaces. The formation of char materials in the gel pores during the combustion is apparent from the pitch-black color of the resulting materials when the olegels were deliberately combusted incompletely by removing them from heat right after the initially large flames diminish. However, it is elusive at the moment how significantly the *in situ* formed char material plays a role of templating in preserving the porosity. Further studies will reveal the effect of viscosity, composition and volatility of the oils on the properties of the products.

3.4 Conclusion

It has been successfully shown that through utilization of biorenewable oil, highly porous γ-Al_2O_3 particles can be synthesized. Given the flexibility of the method inherent from the adopted sol-gel process and from the availability of other various organic liquids and their combinations, it is anticipated that the method can be customized for syntheses of various porous metal oxides. The rapid combustion process is advantageous for large-scale production of the materials with a combustion heat as a useful energy byproduct, which potentially makes the method much resource/energy-efficient.

3.5 References

(1) Trueba, M.; Trasatti, S. P. *European Journal of Inorganic Chemistry* **2005**, 3393.

(2) Li, W.-C.; Lu, A.-H.; Schmidt, W.; Schueth, F. *Chemistry--A European Journal* **2005**, *11*, 1658.

(3) Choi, J.; Suh, D. J. *Catalysis Surveys from Asia* **2007**, *11*, 123.

(4) Euzen, P., Raybaud, P., Krokidis, X., Toulhoat, H., Le Loarer, J., Jolivet, J., Froidefond, C *Handbook of Porous Solids*; Wiley-VCH: Weiheim, 2002.

(5) Yoldas, B. E. *Journal of Applied Chemistry & Biotechnology* **1973**, *23*, 803.

(6) Yoldas, B. E. *Journal of Materials Science* **1975**, *10*, 1856.

(7) Yoldas, B. E. *American Ceramic Society Bulletin* **1975**, *54*, 289.

(8) Yoldas, B. E. *American Ceramic Society Bulletin* **1975**, *54*, 286.

(9) Baumann, T. F.; Gash, A. E.; Chinn, S. C.; Sawvel, A. M.; Maxwell, R. S.; Satcher, J. H., Jr. *Chemistry of Materials* **2005**, *17*, 395.

(10) Baes, C. F., Mesmer, R.E. *The Hydrolysis of Cations*; John Wiley & Sons: New York, 1976.

(11) Livage, J.; Henry, M.; Sanchez, C. *Progress in Solid State Chemistry* **1988**, *18*, 259.

(12) Jolivet, J.-P.; Henry, M.; Livage, J.; Bescher, E. *Metal Oxide Chemistry and Synthesis: From Solution to Solid State*; John Wiley & Sons: New York, 2000.

(13) De Soler-Illia, G. J.; Sanchez, C.; Lebeau, B.; Patarin, J. *Chemical Reviews (Washington, DC, United States)* **2002**, *102*, 4093.

(14) Baumann, T. F.; Gash, A. E.; Fox, G. A.; Satcher, J. H., Jr.; Hrubesh, L. W. In *Handb. Porous Solids*; Schüth, F., Sing, K. S. W., Weitkamp, J., Eds.; Wiley-VCH: Weinheim, Germany, 2002; Vol. 3, p 2014.

(15) Rouquerol, F.; Rouquerol, J.; Sing, K. *Adsorption by Powders and Porous Solids: Principles, Methodology and Applications*; Academic: San Diego, 1999.

(16) Pierre, A. C.; Pajonk, G. M. *Chemical Reviews (Washington, DC, United States)* **2002**, *102*, 4243.

(17) Tetramethyfuran (THF) can be used as an alternative which does not give any polluting gases upon burning.

(18) Zhang, Z.; Hicks, R. W.; Pauly, T. R.; Pinnavaia, T. J. *Journal of the American Chemical Society* **2002**, *124*, 1592.

(19) Suh, D. J.; Park, T.-J.; Kim, J.-H.; Kim, K.-L. *Chemistry of Materials* **1997**, *9*, 1903.

(20) Wilson, S. J.; McConnell, J. D. C. *Journal of Solid State Chemistry* **1980**, *34*, 315.

(21) Krokidis, X.; Raybaud, P.; Gobichon, A.-E.; Rebours, B.; Euzen, P.; Toulhoat, H. *Journal of Physical Chemistry B* **2001**, *105*, 5121.

(22) Kucheyev, S. O.; Baumann, T. F.; Cox, C. A.; Wang, Y. M.; Satcher, J. H., Jr.; Hamza, A. V.; Bradby, J. E. *Applied Physics Letters* **2006**, *89*, 041911/1.

(23) Long, J. W.; Rolison, D. R. *Accounts of Chemical Research* **2007**, *40*, 854.

(24) Oberlander, R. K. *Appl. Ind. Catal.* **1984**, *3*, 63.

(25) Lowell, S.; Shield, J. E.; Thomas, M. A.; Thommes, M. *Characterization of Porous Solids and Powders: Surface Area, and Density*; Kluwer: Dordrecht, The Netherlands, 2004; Vol. 84.

(26) MacKenzie, K. J. D. *Multinuclear Solid-State Nuclear Magnetic Resonance of Inorganic Materials*; Pergamon: New York, 2002.

(27) Khaleel, A. A.; Klabunde, K. J. *Chemistry--A European Journal* **2002**, *8*, 3991.

(28) Wang, J. A.; Bokhimi, X.; Morales, A.; Novaro, O.; Lopez, T.; Gomez, R. *The Journal of Physical Chemistry B* **1998**, *103*, 299.

(29) Hidalgo, F. J.; Zamora, R. In *Handbook of Food Science, Technology, and Engineering; 4 Volume Set*; Hui, Y. H., Ed. 2005; Vol. 1, p 3632 pp.

(30) Ndiaye, P. M.; Tavares, F. W.; Dalmolin, I.; Dariva, C.; Oliveira, D.; Oliveira, J. V. *Journal of Chemical and Engineering Data* **2005**, *50*, 330.

(31) Scholz, V.; Nogueira da Silva, J. *Biomass and Bioenergy* **2008**, *32*, 95.

(32) Ogunniyi, D. S. *Bioresource Technology* **2006**, *97*, 1086.

(33) Conceição, M. M.; Fernandes; Araújo, A. S.; Farias, M. F.; Santos, I. M. G.; Souza, A. G. *Energy & Fuels* **2007**, *21*, 1522.

(34) Mondal, P.; Basu, M.; Balasubramanian, N. *Biofuels, Bioproducts & Biorefining* **2008**, *2*, 155.

(35) Demirbas, A. *Energy Conversion and Management* **2008**, *50*, 14.

(36) Lee, J.; Orilall, M. C.; Warren, S. C.; Kamperman, M.; DiSalvo, F. J.; Wiesner, U. *Nature Materials* **2008**, *7*, 222.

(37) Caps, R.; Fricke, J. *Sol-Gel Technologies for Glass Producers and Users* **2004**, 349.

(38) Norris, P. M.; Shrinivasan, S. *Annual Review of Heat Transfer* **2005**, *14*, 385.

CHAPTER 4

SYNTHESIS OF HIGHLY POROUS GAMMA ALUMINA VIA CONTROLLED GEL DENSIFICATION COUPLED WITH COMBUSTIVE REMOVAL OF PORE LIQUID

4.1 Introduction

Mesoporous γ-alumina particulates with high porosities were successfully prepared from sol-gel reactions through controlled pre-condensation of the gels and subsequent combustion, departing from conventional drying processes. The pre-condensation was achieved by using a mixture of tetrahydrofuran (THF) and castor oil or waste vegetable oil (WVO) in various proportions as the pore liquid. After evaporation of THF, the gels pre-condensed by the evaporation, were combusted and calcined to provide crystalline products with controlled pore volumes varying from 0.9 to 2.8 cc/g and pore sizes from 9 to 22 nm. The largest pore volume corresponds to the porosity close to 91 %, making the product comparable to previously reported aerogels. It is also shown that utilization of waste oil gives similar controlled porosity of the final materials, with pore volumes varying from 0.8 to 2.3 cc/g and pore sizes from 8 to 18 nm, corresponding to a possible maximum porosity of 89 %. The promising results indicate that the new synthetic method can be employed to control the pore properties of the resulting materials, lending itself to possible further optimization and higher porosity products, while using an industrial waste as resources.

High porosity metal oxides such as aerogels are interesting due to their potential applications in sorbents, catalysis and thermal insulation.[1-5] The thermal insulation applications are particularly unique to aerogels, as an ultra high porosity typically over 90 % is important for desired superior insulating properties.[6] Various preparation methods have been reported to control porosity of the materials, wherein drying processes affect the pore texture of the products because surface tension at the liquid/gas interface forces primary particles closer together, thus causing undesirable condensation and densification of the gels.[7-9] Aerogel is obtained from a wet gel by replacing the original pore liquid with a supercritical fluid, a drying technique that results in low density, high porosity materials. Aerogels exhibit a pore structure distinctly different from xerogels, which are obtained from a wet gel by the evaporation of the pore liquid, resulting in a denser, less porous material. Many studies have been reported on the relationship between synthetic conditions and pore properties of aerogel and xerogel.[7,10,11] Other than the ambient drying method through the spring-back effect which has been limited to silica[12], porosities greater than 90 % have been rarely achieved without the use of supercritical drying.

Alumina is most widely used for supports of industrial catalysts because of its advantages in cost and chemical/thermal stability, as well as controllable pore properties.[13-16] Various alumina products with a wide range of surface areas and porosities suitable for a variety of catalytic

applications are commercially available.[8] However, the industrial importance and demand for alumina (and alumina based materials) makes it a very active area of research including the development and investigation of new preparation methods with ability to control pore structures in a cost effective and environmentally viable manner. In fact, alumina aerogels with ultra high porosity have been relatively expensive to produce due to the supercritical drying process employed in the literature.[17,18]

In previous work, a synthetic method that produces highly mesoporous, transparent γ-alumina particulates while sidestepping drying processes typical in sol-gel-based synthetic methods was reported.[19] In the synthesis, the pore liquid in the wet gel was first exchanged with a solvent that is miscible with vegetable (biorenewable) oil. The solvent was then replaced by the oil to produce an oil-soaked gel (called “olegel”). In order to remove the oil from the gel pores, the olegel was quickly heated and combusted. The heating dehydrates/crystallizes the pore wall material *simultaneously* without drastic pore collapsing. The combustive removal of all the carboneous species by the combustion and calcination leaves a highly porous metal oxide product (called “pyrogel”). Compared to organic solvents, the vegetable oil or plant oil does not evaporate as significantly before ignition, which may avoid serious gel shrinkage and pore collapsing during the heating. It was shown that the new method afforded relatively high mesopore volume close to 2.0 cc/g, which

corresponds to 88 % porosity (hereafter, porosity is given as the one estimated from the alumina density and pore volume from BET analysis). Given the fact that the as-prepared alumina wet gels contained only less than 0.8% of solid boehmite in volume, the observed porosity implies that the gel shrinkage or consolidation is still significant. Indeed, even for alumina aerogels, volume shrinkage up to 45% has been observed during calcination alone, a step necessary to form crystalline γ-Al_2O_3 via the dehydration of boehmite.[17] Further studies will be required to fully understand the capacity of the new method and to extend it so as to produce materials with even higher porosities by minimizing the gel condensation during the combustion.

One distinct feature of the olegel route is that the oil has the highest boiling point among the pore liquids, such as water, alcohols and other typical organic solvents, utilized during the synthetic steps. This in fact allows the elimination of the low-boiling point solvent in the olegels more rapidly and completely; i.e., simple heating of the olegel in a lab oven evaporates the solvents, leaving only the oil in the pores. The loss of the solvents in the pores inevitably causes gel shrinkage (condensation). On the other hand, this effect can be utilized to deliberately pre-condense the gel before the subsequent combustion and to study its effect on the resulting pyrogel porosity. Herein, we demonstrate that such controlled gel pre-condensation is beneficial and can be used to tailor the porosity of the pyrogel products, with pore volumes reaching up to 2.8 cc/g,

corresponding to 91 % porosity. It is also demonstrated that waste vegetable oil, an industrial waste, can be utilized in place of fresh oil, and a product with porosity reaching 89 % can still be achieved, which makes the new synthetic more attractive in terms of effective use of resources.

4.2 Experimental

4.2.1 Synthesis of Variable Porosity γ-Al_2O_3

Two different oils were employed; castor oil (The Chemistry Store.com Inc, Cayce, South Carolina, Catalog No. 51006-5; boiling point = 313 ℃) and waste vegetable oil. The waste vegetable oil (WVO) was donated by Arizona BioDiesel (Gilbert, Arizona; website at www.azbiodiesel.com) and used after filtration to remove any solid particles. For each oil, the initial wet alumina gel was prepared following the procedure described by Baumann *et al*. using inorganic salt precursors and an epoxide as a gel initiator.[17] In a typical procedure, 29.6 g of $AlCl_3 \cdot 6H_2O$ (Sigma-Aldrich, 99%) was dissolved in 200 ml of a 50:50 volume mixture of deionized water and absolute ethanol (Decon Laboratories, Inc.). Propylene oxide (PO) (1,2-epoxypropane, Sigma-Aldrich, 99%) was then added to the clear solution in a molar ratio of Al^{3+}:PO of 1:10 and stirred for 10 min. The reaction was exothermic and after stirring, the solution had a pH around 2. Gelation of the solution generally occurred within 30 min at room temperature, with the final pH of the gel reaching about 5. After three days of aging in a closed container

the gels were broken into smaller pieces of *ca*. 1 cm^3 and placed in a bath of tetrahydrofuran (THF) (Spectrum Laboratories; boiling point = 66 ℃) for three days with the bath solvent being replaced once a day. Subsequently, olegels were prepared from the wet gels by modifying the process described in our previous work,[19] in order to accommodate controlled pre-condensation of the gel as the following.

For each set of the experiments with castor oil or waste vegetable oil, the THF-soaked gel was first divided into ten samples. The samples were placed separately in different baths that contained mixtures of oil and THF at various ratios (Tables 1 and 2), and were allowed to soak for two days and subsequently removed from the baths. The sample names are designated based on the oil used, castor oil (C) and WVO (W), and the oil vol% in the oil/THF mixtures. As a reference, one sample (REF in Table 1) was thoroughly soaked only in a THF bath, by changing the solvent once a day for three days. The oil molecules in the oil/THF mixture outside the gel slowly diffuse through the gel pores. The equilibrium of the diffusion was monitored by color change of the gel. The color intensity did not increase after one day, indicating that the diffusion could reach to an equilibrium within a day. After the soaking steps, all the samples were then placed in a lab oven heated at 70 ℃ for 4 h to evaporate off the THF, leaving only the oil in the gel pores (olegel preparation).

A small amount of excess oil was dropped onto each olegel sample and the olegel pieces were coated evenly with the oil by rolling the

individual pieces around in the added excess oil. This additional oil coating was found to be effective in providing more homogeneous combustion products by minimizing premature oil evaporation from the surface of the olegel pieces. The olegel pieces were then evenly spread on an Inconel dish and placed in an ashing furnace (Carbolite AAF 1100) preheated at 700 ℃. The olegel pieces ignited within 3 – 10 seconds, giving off a large flame before breaking apart into small particulates. The flame ceased within three to six minutes and the material was further kept at 700 ℃ for 10 h in the furnace to completely burn off any carbonaceous species. Analysis of the residual carbon content was obtained by employing Perkin-Elmer 2400 Series II CHNS/O Analyzer with a thermal conductivity detector.

4.2.2 Physical Characterization

Powder X-ray diffraction (PXRD) data was collected using a Siemens D5000 diffractometer with a Cu-Kα radiation. High-resolution transmission electron microscopy (HRTEM) was performed on a JEOL JEM 2000FX TEM (LaB_6 source, accelerating voltage 200 kV, PTP resolution 0.28 nm). The TEM samples were prepared by first grinding the pyrogels in an agate mortar in ethanol. A copper grid covered with lacy carbon was submerged in the solution, taken out and then allowed to dry in air. The images were taken under bright field conditions. N_2 sorption experiments were carried out with a Micromeritics ASAP2020 volumetric adsorption analyzer (samples REF, C10, C20, C90, C100, and all WVO

samples), or with a Micromeritics Tristar II 3020 (samples C30 – C80), by using nitrogen as the adsorbate at 77K. Prior to the analysis, samples weighing around 150 mg were degassed at 300 ℃ for 10 h under vacuum on the ASAP2020 until a residual pressure of ≤10 μmHg was reached, or under ambient pressure on the Tristar II 3020. Specific surface areas were calculated according to the Brunauer-Emmett-Teller (BET) equation using nitrogen adsorption isotherms in the relative pressure range from 0.06 to 0.2. For the calculation of pore size distribution, the desorption branch was considered and the pore volume was obtained from the amount of nitrogen adsorbed at a relative pressure of 0.99. Mesopore size distributions were obtained using the Barrett-Joyner-Halenda (BJH) method assuming a cylindrical pore model. HP 5890 Gas Chromatograph interfaced to a HP 5972 Mass Selective Detector Quadruple Mass Spectrometer was used for compositional analysis of the waste vegetable oil. In order to increase the volatility of the fatty acids, they were converted to their corresponding fatty acid methyl esters (FAME) before the analysis.

4.3 Results and Discussion

4.3.1 Synthesis

Highly mesoporous, glassy (semi)transparent γ-alumina particulates were prepared with different pore sizes and pore volumes by varying the oil:THF ratio of the pore liquid in the presented new procedure (Table 1

and 2 for the castor oil-based and the WVO-based samples, respectively). The substantial transparency is consistent with previous results[19] and is due to the absence of grain boundaries which results in low light-scattering. The synthetic procedure closely follows our previous work based on a gel combustion process, rather than drying. As in typical sol-gel based porous materials synthesis, the procedure starts with the formation of an inorganic wet gel. The water/ethanol pore liquid is first replaced by THF, a low-boiling point solvent that is miscible with vegetable oil as well as water and ethanol. A certain amount of the THF in the gel pores is then replaced by the oil, by soaking the gel in an oil/THF mixture bath with a predetermined oil:THF ratio (the second column in Tables 1 and 3). The oil:THF ratio in the gel at diffusion equilibrium (the third column in Tables 1 and 3) can be estimated based on the experimental wet gel volumes, oil/THF volumes and on the theoretical pore volume determined from the volume of solid in the wet gel (0.8 vol%). The subsequent heating of the gel at 70 ℃ evaporates the THF, leaving only the oil in the gel pores. The THF evaporation causes the gel to condense to a controlled or predetermined extent in that the condensed volume of the gel is determined by the relative amount of oil in the pores and thus the condensation ratio can be estimated as the ratio of the initial gel volume to the final gel volume (the fourth column in Tables 1 and 3). The pre-condensed gels are combusted to give the calcined γ-alumina pyrogels. After the subsequent carbon burn-off, elemental analysis

showed that the residual carbon content is less than 0.3 wt% for the samples.

Table 1. Selected properties of γ-Al_2O_3 pyrogel samples synthesized using castor oil.

Sample	Oil:THF vol. in exchange solvent	Oil:THF vol. in pores at equilibrium	Pre-condense ratio[a]
REF	0:100	0:100	122
C10	10:90	7:93	12
C20	20:80	15:85	6.4
C30	30:70	22:78	4.4
C40	40:60	29:71	3.4
C50	50:50	37:63	2.7
C60	60:40	44:56	2.2
C70	70:30	51:49	1.9
C80	80:20	59:41	1.7
C90	90:10	66:34	1.5
C100	100:0	73:27	1.4

[a](Initial gel volume)/(final gel volume after THF evaporation)

Table 2. Properties of γ-Al_2O_3 pyrogel samples synthesized using castor oil.

Sample	BET surface area (m^2/g)	BET surface area from micropores[a] (m^2/g)	BJH pore diameter[b] (nm)	BJH pore volume[c] (cm^3/g)	Porosity[d] (%)
REF	237	20	9	0.7	73
C10	339	44	18	2.2	89
C20	338	45	22	2.8	91
C30	322	36	20	2.2	89
C40	328	37	17	1.9	88
C50	299	27	11	1.1	81
C60	275	24	9	0.9	77
C70	300	28	13	1.3	83
C80	372	34	13	1.7	86
C90	317	38	17	1.9	88
C100	320	42	21	2.2	89

[a] by the use of *t*-plots with the Harkins-Jura model.

[b] 4(total pore volume)/(surface area).

[c] from the pores with the pore width no larger than 150 nm.

[d] from the BJH pore volume and theoretical density of γ-Al_2O_3

It was observed that the oil/THF soaked gels cracked and broke apart into small particles during the THF evaporation, in addition to their apparent shrinkage. The resulting olegels were always harder than the original oil/THF-soaked gels. For the samples with castor oil, the olegels were completely transparent for the samples made with an oil volume between 10 and 50 % (samples C10 – C50). For 50 – 100 % oil volume, the olegels became opaque and white during the THF evaporation (C60 –

C100), with the opacity increasing with the oil amount. However, the resulting pyrogel particles were semitransparent or transparent (after the calcination). It is suspected that there is a certain degree of microscopic heterogeneity in oil distribution, due to the increased viscosity of the THF/oil mixture, causing visible light scattering in the samples made with higher oil content. This heterogeneity, however, is not apparent in the final pyrogels, showing that the employed combustion process is forgiving towards minimal heterogeneous oil distribution. For the samples treated with the WVO, the effect of the oil amount was not as pronounced. Slight shrinkage was observed in the samples with oil content higher than 50 %, but all samples appeared translucent and amber in color, reflecting the dark color of the WVO. The olegels from the WVO are always less hard than those from castor oil. This is due to the fact that castor oil is more viscous than the majority of plant or vegetable oil.[20] The GC-MS analysis of the WVO showed highest concentrations of palmitic and linoleic acid, with behenic and arachidic acids being second most in abundance. These acids make up the major triglycerides found in palm oil, sunflower oil, corn oil, canola oil and peanut oil.[21]

Table 3. Selected properties of γ-Al_2O_3 pyrogel samples synthesized using WVO.

Sample	Oil:THF vol. in exchange solvent	Oil:THF vol. in pores at equilibrium	Pre-condensation ratio[a]
W10	10:90	7:93	12
W20	20:80	15:85	6.4
W30	30:70	22:78	4.4
W40	40:60	29:71	3.4
W50	50:50	37:63	2.7
W60	60:40	44:56	2.2
W70	70:30	51:49	1.9
W80	80:20	59:41	1.7
W90	90:10	66:34	1.5
W100	100:0	73:27	1.4

[a](Initial gel volume)/(final gel volume after THF evaporation)

Table 4. Properties of γ-Al_2O_3 pyrogel samples synthesized using WVO.

Sample	BET surface area (m^2/g)	BET surface area from micropores[a] (m^2/g)	BJH pore diameter[b] (nm)	BJH pore volume[c] (cm^3/g)	Porosity[e] (%)
W10	326	40	17	2.0	88
W20	332	39	18	2.3	89
W30	297	28	10	1.1	81
W40	286	23	9	1.0	78
W50	298	29	9	1.0	79
W60	294	28	9	1.0	78
W70	290	27	8	0.9	76
W80	288	26	8	0.8	75
W90	293	25	8	0.8	76
W100	286	25	8	0.8	76

[a]by the use of *t*-plots with the Harkins-Jura model.

[b]4(total pore volume)/(surface area).

[c]from the pores with the pore width no larger than 150 nm.

[d]from the BJH pore volume and theoretical density of γ-Al_2O_3

4.3.2 Powder X-ray Diffraction

All of the samples exhibit similar XRD patterns regardless of the oil type and oil amount used for their synthesis, and the patterns show the Bragg reflection peaks that are assigned to the structure of γ-Al_2O_3 (ICSD 66559).[17,18,22] No impurities were observed in the XRD patterns. Figure 4.1 shows the powder XRD patterns of six representative samples, REF, C20, C60, C100, W20 and W80, which are chosen for their highest or lowest porosities (column 9 in Tables 1 and 2). The γ-Al_2O_3 structure is typically described as a defect spinel structure with varied degrees of a

tetragonal distortion (*c/a* = 1 ~ 0.985) which depend on the heating condition.[23,24] The broadening of the Bragg peaks may be attributed to two factors, the disordering of the aluminum ions particularly at the octahedral sites, and small constituting particle sizes. Because of the face-centered cubic close packing of oxide ions, the (400) and (440) reflections tend to dominate the XRD pattern.[17]

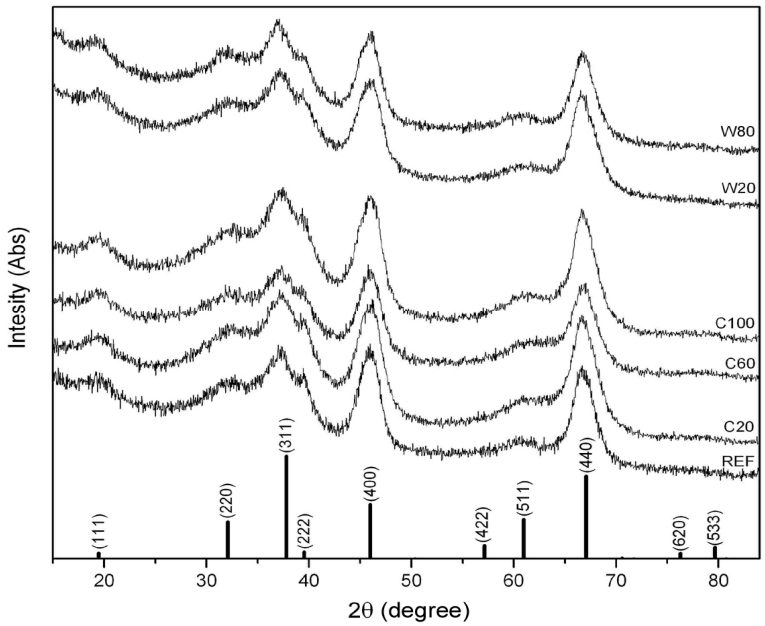

Figure 4.1. Powder X-ray diffraction patterns of samples REF, C20, C60, C100, W20 and W80, along with the simulated pattern of γ-Al_2O_3 (ICSD 66559).

In Figure 4.1, the (400) and (440) reflections of the spinel are neither split into two peaks, nor apparently asymmetric, which indicates that the products do not exhibit a strong tetragonal deformation. The results positively exclude the so-called “three spinel blocks structure” of δ-Al_2O_3,

which develops more extensively with a greater tetragonal distortion and gives additional Bragg reflections due to the superstructure formation.[23,24]

4.3.3 Electron Microscopy

Transmission electron microscopy was used to evaluate the microstructure of the varying samples of pyrogels. Homogeneity of the final pyrogel samples was confirmed by examining multiple areas of the TEM sample grid. Pyrogels with the highest (samples C20 and W20) and lowest pore porosities (samples C60 and W80) are shown in Figure 4.2. All of the samples exhibited a common three-dimensional interconnection of rod shaped particles from 2 – 7 nm in diameter and of varying lengths. The web-like textural porosity is consistent with previous reports on the preparation of γ-Al_2O_3 pyrogels and aerogels using the same precursors for initial wet-gel formation.[17,19] The degree of connectivity of the particles appeared to vary between samples. A large difference can be seen in the concentration of particles within a given area as well as the degree of connectivity, with connectivity being defined as the number of particles in contact with a given particle. Due to the random pore network nature of the pyrogels, it is difficult to quantify the exact interparticle spacing and connectivity by sole examination of the structure using TEM, yet general observations can be made after looking at several areas of the material on the TEM sample grid. The larger pore width and pore volume samples showed, in general, a lesser degree of connectivity and larger interparticle spacing compared to the smaller pore width and pore volume samples.

The TEM microstructural observations were supported by the trends in BJH pore volumes and the average pore sizes of the samples (Tables 1 and 2).

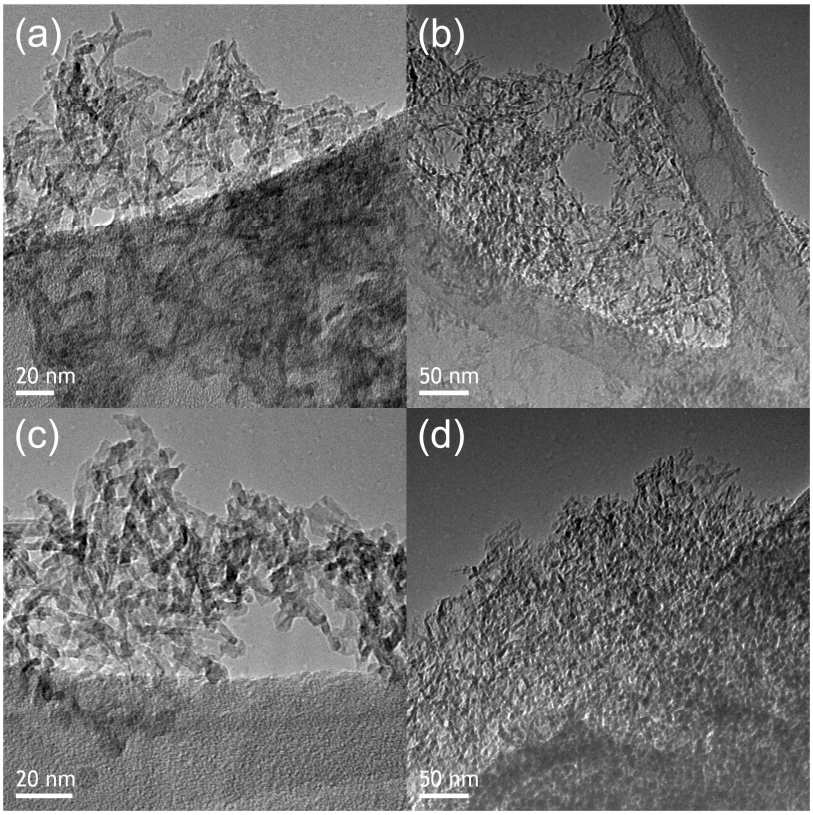

Figure 4.2. High-resolution transmission micrographs of samples (a) C20, (b) W20, (c) C60 and (d) W80

4.3.4 Surface Area and Porosity Analysis

The specific surface areas, average pore diameters and pore volumes for the alumina pyrogels were measured using nitrogen adsorption/desorption methods (Tables 2 and 4). The adsorption/desorption isotherms for the alumina pyrogels are summarized in Figure 4.3. All of the isotherms can be classified as type IV,

characteristic for mesoporous materials, based on the classification by Brunauer. All the isotherms show an H1- or H2-type of hysteresis, with hysteresis loops at relative pressures above 0.7 for the castor oil samples and 0.65 for the WVO samples.

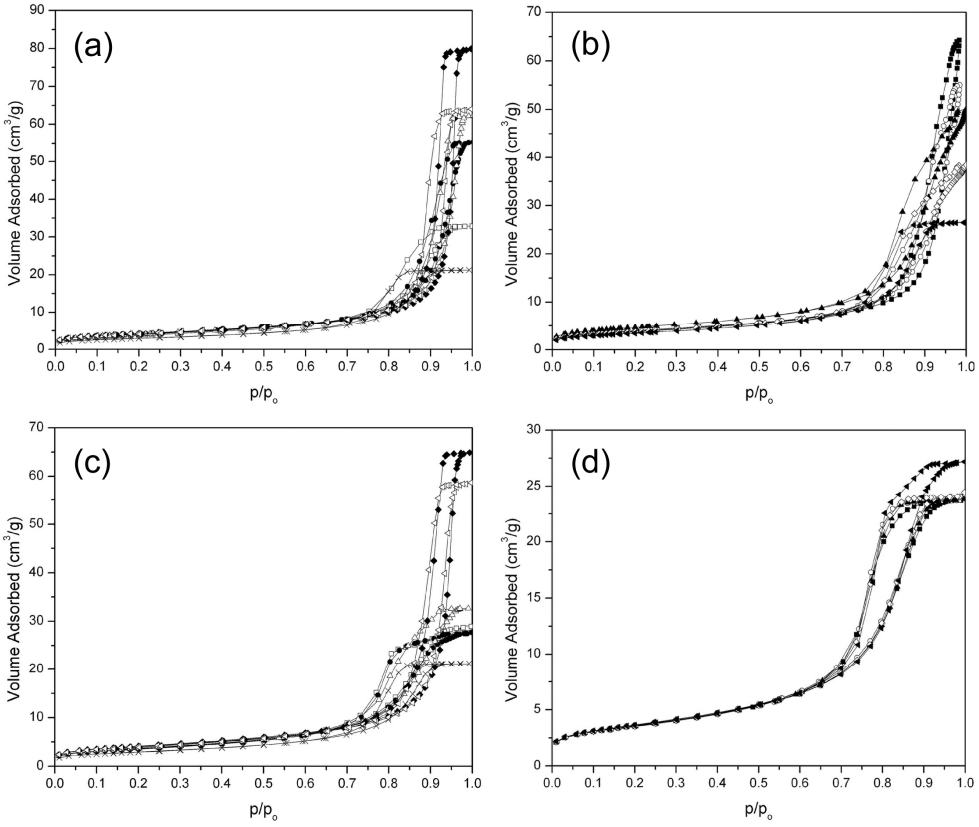

Figure 4.3. N_2 sorption isotherms of the samples (a) REF (×), C10 (◁), C20 (◆), C30 (△), C40 (●), C50 (□); (b) C60 (◀), C70 (◇), C80 (▲), C90 (○), C100 (■); (c) REF (×), W10 (◁), W20 (◆), W30 (△), W40 (●), W50 (□); (b) W60 (◀), W70 (◇), W80 (▲), W90 (○), W100 (■).

The desorption branch was used to calculate the pore size distribution based on the BJH method (Figure 4.4). From the BET analysis, the estimated surface areas range from 275 to 372 m^2/g for the pyrogels made using castor oil and 286 to 332 m^2/g for samples made using WVO, mostly contributed from mesopores.

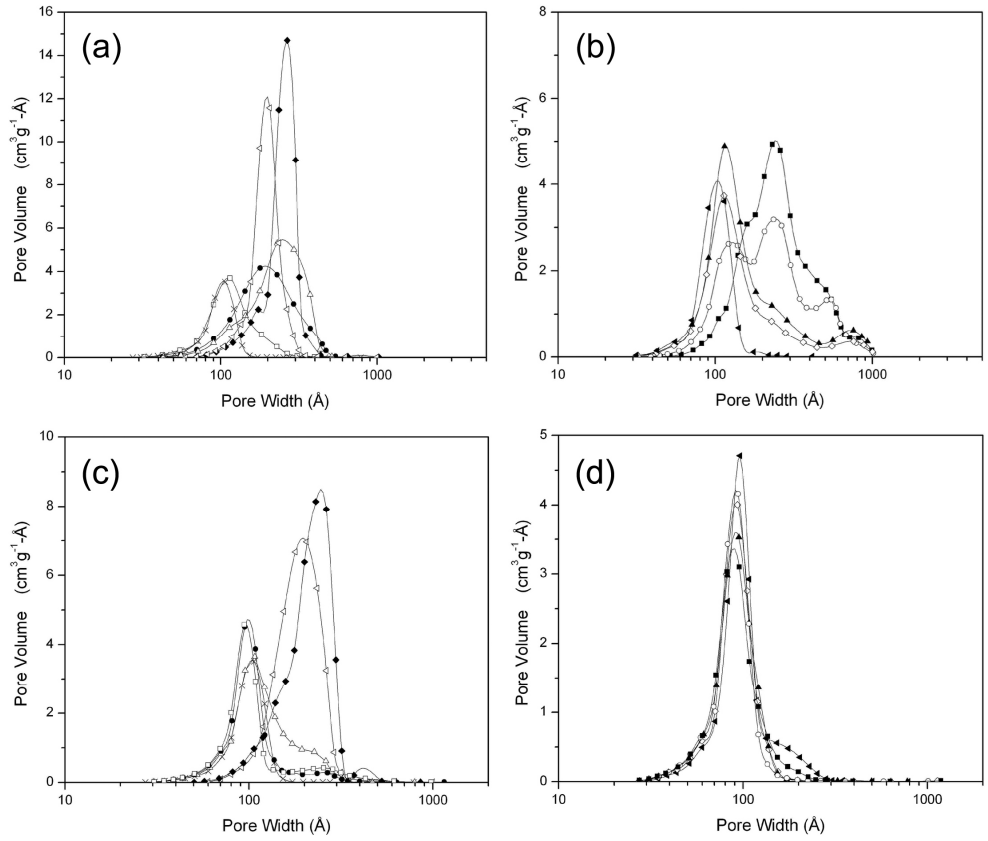

Figure 4.4. BJH pore width distribution of the (a) REF (×), C10 (◁), C20 (◆), C30 (△), C40 (●), C50 (□); (b) C60 (◀), C70 (◇), C80 (▲), C90 (○), C100 (■); (c) REF (×), W10 (◁), W20 (◆), W30 (△), W40

The surface area of the pyrogels does not appear to be dependent of the oil/THF mixture as there was no definitive trend seen in either series of samples. However, all of the pyrogel samples do show a greater surface

area than the REF sample, which was synthesized using THF as the sole pore liquid, indicating that the presence of oil in the gel pores positively influences the pore property.

The BJH pore volume and pore width of the pyrogel products are shown as a function of the oil content in Figures 4.5 and 4.6, respectively. All the olegel samples have a pore volume larger than the sample REF (0.7 cm^3/g), which is consistent with the surface area results. For castor oil-based pyrogel products (solid circles in Figure 4.5), the pore volume increases as the oil content increases but rapidly reaches its maximum value of 2.8 cm^3/g at C20 (i.e., 15 % oil in the pores). It decreases down to 0.9 cm^3/g when the oil content is about 45 % in the pore liquid. As the oil content in the olegels increases further, the pore volume becomes larger again up to 2.2 cm^3/g (C100, 73 % oil). For the pyrogels from WVO (solid triangles in Figure 4.5), a similar trend is observed and the maximum pore volume occurs for W20, which is consistent with the castor oil results (solid circles). However, the 2.3 cm^3/g pore volume of W20 is significantly lower than that of C20. Furthermore, all the products from the high WVO content olegels have a noticeably small pore volume which is close to the value from the sample REF. In any event, the maximum pore volume of 2.8 cm^3/g found for C20 corresponds to 91 % porosity based on the theoretical density of γ-Al_2O_3. This is higher than the 88 % porosity (2.0 cm^3/g BJH pore volume) of the pyrogel reported in our previous work and also the 89 % porosity (2.3 cm^3/g) of the calcined γ-Al_2O_3 aerogels

reported from the same chloride precursor method.[17] The latter is comparable to the pore volume found for W20, indicating that the utilization of WVO in the pyrogel synthesis can provide products with porosities as high as what has been found for calcined aerogels from supercritical drying.

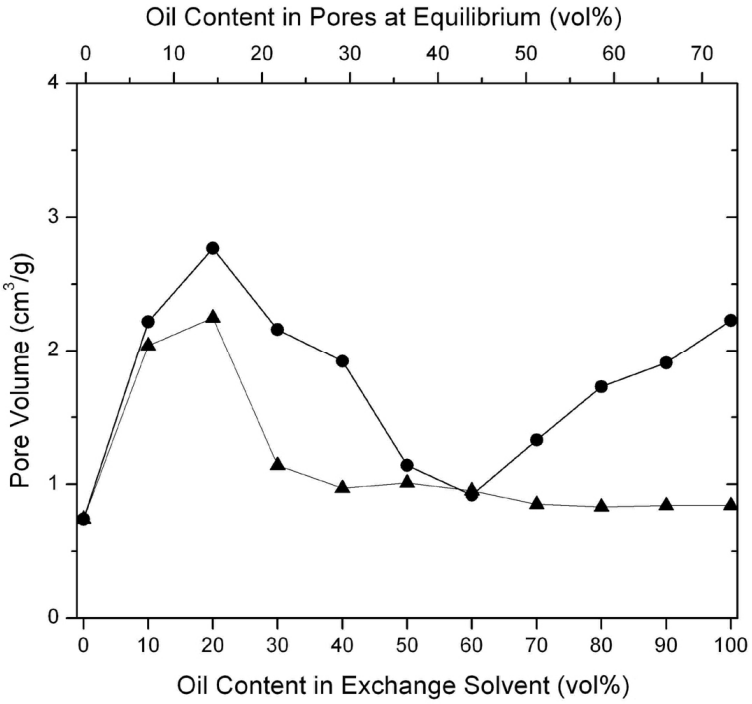

Figure 4.5. Pore volume vs. oil content of the olegels for the castor oil-based samples (C10 – C100, solid circles) and the waste vegetable oil-based samples (W10 – W100, solid triangles), with the sample REF at 0 % oil content.

The trend in the pore width of the pyrogels shown in Figure 4.6 correlates with their respective pore volume. The maximum pore widths are 22 nm (C20) for the castor oil-based pyrogels and 18 nm (W20) for the

WVO-based pyrogels. The pore widths of W70 – W100 pyrogels are 8 nm, which is comparable to the sample REF. For the castor oil-based pyrogels, however, the pore width of C70 – C100 monotonically increases up to 21 nm as the castor oil content increases.

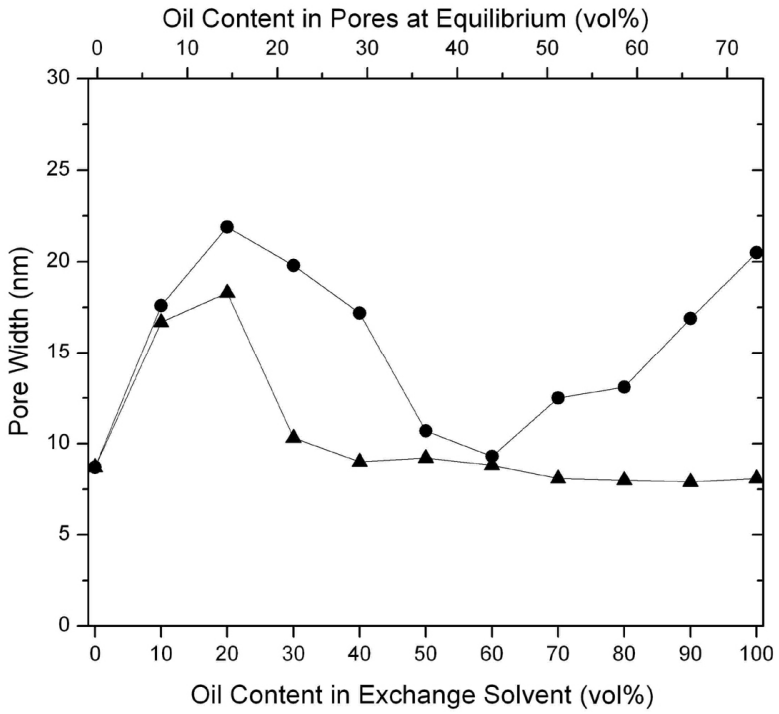

Figure 4.6. BJH pore width vs. oil content of the olegels for the castor oil-based samples (C10 – C100, solid circles) and the waste vegetable oil-based samples (W10 – W100, solid triangles), with the sample REF at 0 % oil content.

As far as castor oil is concerned, the increase in porosity in the high oil content region is consistent with our previous assumption that the presence of oil in the pores is critical in preserving pore structure to some extent during the calcination. When the olegel burns, evaporation of the oil and oxygen diffusion takes place through the tortuous gel network and

hence become delayed significantly, as understandable considering that the well-known low thermal conductivity of aerogels is partly due to the slowed gas diffusion through the pore network.[25,26] This is evidenced by the observation that the combustion of the olegels takes five to six times longer than what we observed for the corresponding oil itself. The oxygen-deprived heating leads to thermal polymerization of the oil and subsequent char formation in the pores which may help minimizing formation of liquid/gas interfaces. The formation of char materials in the gel pores during the combustion is apparent from the pitch-black color of the resulting materials when the olegels were deliberately combusted incompletely by removing them from heat right after the initially large flames diminish.

For the WVO-based pyrogels, however, the consistently low porosities among the products from the high oil content olegels imply that the role of WVO in pore preservation is minimal for those samples. The reason for the less spectacular performance of WVO may be understood from the difference in the chemical and thermal characteristics of the two oils. In castor oil, the main fatty acid, comprising of almost 87% of the total amount of triglycerides, is ricinoleic acid, a C15-hydrocarbon chain with one double bond at the C-9 position and a hydroxyl at the C-11 position.[27] The presence of the hydroxyl makes castor oil the most viscous and least volatile among most vegetable or plant oil. Upon heating, the hydroxyl group combines with a hydrogen on a β-carbon to

undergo dehydration and hence provides conjugated double bonds which then undergo polymerization at temperatures as low as 150 ℃.[28] The lower onset temperature of polymerization leads to slow evaporation/atomization of the oil, increased oxidative and thermal polymerization and promotion of the formation of carboneous residue deposit.[29] On the contrary, the WVO in this work consists mainly of palmitic and linoleic acids as the most dominant fatty acids present. Linoleic acid has two unconjugated double bonds in each hydrocarbon chain while palmitic acid has a saturated hydrocarbon chain. Their free-radical polymerization becomes significant only at higher temperatures. This would result in a larger amount of evaporation during combustion causing a significant collapse of the pore structure, leading to a lower porosity pyrogel, which is disfavored for our purpose..

Even for the pyrogels from the low oil content olegels, the castor oil still provides a higher pore volume than the WVO and yet the difference is not as drastic. Especially, C10 and W10 are much the same with 2.2 and 2.0 cm^3/g pore volumes and 18 and 17 nm pore width, respectively. This indicates that the effect of oil characteristic is much less pronounced in determining the porosity at the lower oil contents. Furthermore, it is striking that the porosities from the low oil content olegels are much higher than the ones from the high oil content olegels. These observations can be explained by considering the fact that the low oil content olegels have a denser solid network due to the controlled pre-condensation through

selective THF evaporation. When the olegels burn, the consequent pore collapsing is expected to be less severe if the pore wall is denser and thus potentially more robust, and the resulting pyrogels are more porous. In addition, the denser olegels are less likely affected by the nature of the oil, which is consistent with our observation. Future studies will reveal the effect of temperature and type of solvent in solvent/oil mixture on the pre-condensation and therefore pore properties of the final pyrogels.

4.4 Conclusion

It has been demonstrated that utilization of biorenewable oil and control of gel pre-condensation can afford highly mesoporous, glassy (semi)transparent γ-alumina particulates all while bypassing the supercritical drying process. While the important role of the oil in gel calcination has been illustrated already, this work newly shows that controlled pre-condensation of the wet gel can drastically increase the porosity of the final product in a synergistic way. Control over the pore volume and pore width could be achieved by simply choosing the proper pre-condensation ratio. It is also shown that WVO can be a viable replacement for pure oil for the synthesis of highly porous γ-alumina that is in par with γ-alumina aerogels from supercritical drying, providing a synthetic procedure that utilizes a waste material as a chemical component in synthesis and as a source of heat that may be convertible into electrical energy.

4.5 References

(1) Husing, N.; Schubert, U. *Angewandte Chemie, International Edition* **1998**, *37*, 22.

(2) Kucheyev, S. O.; Baumann, T. F.; Cox, C. A.; Wang, Y. M.; Satcher, J. H., Jr.; Hamza, A. V.; Bradby, J. E. *Applied Physics Letters* **2006**, *89*, 041911/1.

(3) Pajonk, G. M. *Catalysis Today* **1999**, *52*, 3.

(4) Tiemann, M. *Chemistry--A European Journal* **2007**, *13*, 8376.

(5) Rao, Y.; Antonelli, D. M. *J. Mater. Chem.* **2009**, *19*, 1937.

(6) Carlson, G.; Lewis, D.; McKinley, K.; Richardson, J.; Tillotson, T. *Journal of Non-Crystalline Solids* **1995**, *186*, 372.

(7) Alie, C.; Pirard, R.; Lecloux, A. J.; Pirard, J.-P. *Journal of Non-Crystalline Solids* **1999**, *246*, 216.

(8) Kim, S.-W.; Iwamoto, S.; Inoue, M. *Journal of Porous Materials* **2010**, *17*, 377.

(9) Klvana, D.; Chaouki, J.; Repellin-Lacroix, M.; Pajonk, G. M. *Journal de Physique, Colloque* **1989**, C4.

(10) Baumann, T. F.; Gash, A. E.; Fox, G. A.; Satcher, J. H., Jr.; Hrubesh, L. W. In *Handbook of Porous Solids*; Schüth, F., Sing, K. S. W., Weitkamp, J., Eds.; Wiley-VCH: Weinheim, Germany, 2002; Vol. 3, p 2014.

(11) Jarzebski, A. B.; Lorenc, J.; Aristov, Y. I.; Lisitza, N. *Journal of Non-Crystalline Solids* **1995**, *190*, 198.

(12) Rolison, D. R.; Dunn, B. *Journal of Materials Chemistry* **2001**, *11*, 963.

(13) Trueba, M.; Trasatti, S. P. *European Journal of Inorganic Chemistry* **2005**, 3393.

(14) Seki, T.; Onaka, M. *Catalysis Surveys from Asia* **2006**, *10*, 138.

(15) Rambo, C. R.; Sieber, H. *Advanced Materials (Weinheim, Germany)* **2005**, *17*, 1088.

(16) Pinnavaia, T. J.; Zhang, Z.; Hicks, R. W. *Studies in Surface Science and Catalysis* **2005**, *156*, 1.

(17) Baumann, T. F.; Gash, A. E.; Chinn, S. C.; Sawvel, A. M.; Maxwell, R. S.; Satcher, J. H., Jr. *Chemistry of Materials* **2005**, *17*, 395.

(18) Suh, D. J.; Park, T.-J.; Kim, J.-H.; Kim, K.-L. *Chemistry of Materials* **1997**, *9*, 1903.

(19) Ladd, D. M.; Volosin, A.; Seo, D.-K. *Journal of Materials Chemistry* **2010**, *20*, 5923.

(20) Fountain, C. W.; Jennings, J.; McKie, C. K.; Oakman, P.; Fetterolf, M. L. *Journal of Chemical Education* **1997**, *74*, 224.

(21) U.S. Department of Agriculture, Agricultural Research Service. 2009. USDA National Nutrient Database for Standard Reference, Release 22. Nutrient Data Laboratory Home Page, http://www.ars.usda.gov/ba/bhnrc/ndl, products and services-fats and oils.

(22) Zhang, Z.; Hicks, R. W.; Pauly, T. R.; Pinnavaia, T. J. *Journal of the American Chemical Society* **2002**, *124*, 1592.

(23) Wilson, S. J.; McConnell, J. D. C. *Journal of Solid State Chemistry* **1980**, *34*, 315.

(24) Krokidis, X.; Raybaud, P.; Gobichon, A.-E.; Rebours, B.; Euzen, P.; Toulhoat, H. *Journal of Physical Chemistry B* **2001**, *105*, 5121.

(25) Caps, R.; Fricke, J. *Sol-Gel Technologies for Glass Producers and Users* **2004**, 349.

(26) Norris, P. M.; Shrinivasan, S. *Annual Review of Heat Transfer* **2005**, *14*, 385.

(27) Ogunniyi, D. S. *Bioresource Technology* **2006**, *97*, 1086.

(28) Conceição, M. M.; Fernandes; Araújo, A. S.; Farias, M. F.; Santos, I. M. G.; Souza, A. G. *Energy & Fuels* **2007**, *21*, 1522.

(29) Mondal, P.; Basu, M.; Balasubramanian, N. *Biofuels, Bioproducts & Biorefining* **2008**, *2*, 155.

CHAPTER 5

SYNTHESIS OF ROBUST SILICA AEROGEL-LIKE MATERIALS VIA A HIGH TEMPERATURE COMBUSTION ROUTE

5.1 Introduction

Silica gel materials are some of the most studied materials in inorganic chemistry owing to the abundance of silicon present on earth and the presence of polysilicate gels and particles in natural systems. Tetraehtylorthosilicate (TEOS), on of the most common precursors used in the modern day synthesis of silica gels, was first synthesized in 1845 by Ebelmen who subsequently also discovered that TEOS could undergo hydrolysis producing fibers that would form into gels over an extended period of time.[1] This initial discovery was further confirmed and formulated into the knowledge that organosilicate compounds could form siloxane polymers containing organic side groups, and through subsequential hydrolysis and condensation, result in monolithic gels.[2] The ease at which silica gels form made them an ideal candidate for the first attempts to produce aerogels, materials in which the liquid inside of the gel's pores is exchanged for air.[3] Silica aerogels and other highly porous silica materials have become some of the most utilized materials for catalysis and catalytic supports,[4-8] thermal[9-12] and acoustical insulation,[13,14] filtration and separation applications,[15] as well as use in optical sensors.[16]

The vast variety of uses for silica (SiO_2) aerogels has created such a demand that the materials currently being mass produced and sent out

for use in large scale production applications.[17,18] Aerogels have historically been made using a supercritical drying technique, which has been extensively covered in Chapter 1 of this thesis. Recently, attempts have been made to synthesize SiO_2 aerogel-like materials using ambient drying techniques that involve surface modification that prevent the irreversible collapse of the pores during evaporation of the solvent out of the wet gel.[19-24] The resulting materials exhibit aerogel-like porosity and surface areas, however are impractical at large scale due to the expensive precursors required for the surface modification. Even with the possibility of using an ambient temperature and pressure drying technique, aerogels ultra low density and high porosities come at the price of mechanical strength. Controlled sintering of the solid network has been shown to increase the mechanical strength of SiO_2 aerogels, allowing them to be immersed in liquid with minimal structural collapse.[24] It is ideal to find a synthetic route in which highly porous SiO_2 can be produced without the need for high pressure autoclaves or super critical drying and the use of expensive precursors. The formed product must exhibit mechanical robustness so it can be utilized in applications that may require the material to be wetted or soaked in a liquid without complete structural collapse.

It has been shown in the case of γ - alumina, that a high temperature combustion synthetic technique is viable for producing highly porous, robust, metal oxide materials.[25] It was shown that starting with an

inorganic wet gel, the liquid inside of the pores can be replaced with a combustible liquid, such as oil, that can then be exposed to temperatures above the liquids auto-ignition temperature, causing spontaneous combustion and rapid formation of solid carbon residue acting as a structural support inside of the pores. The carbon residue can then be slowly burned away affording a robust, porous product. It will be shown that a high temperature combustion synthesis could be used for the production of SiO_2 materials with high porosities, controllable pore volume and pore width, as well as mechanical strength great enough to allow them to be submerged in liquids without structural collapse.

5.2 Experimental

5.2.1 Synthesis of porous SiO_2

The initial wet silica gel was prepared following the procedure described by Livermore *et al.*[26], a base catalyzed synthesis using TEOS as a silica source. In a typical procedure, two solutions were made, a silica solution and a catalyst solution. For the silica solution, 25 mL of TEOS was added to 40 mL of absolute ethanol and mixed. 1.21 mL of 0.5 M ammonium fluoride was then added to the silica solution and stirred. The catalyst solution was prepared by combining 35 mL of absolute ethanol, 70 mL of water and 0.275 mL of 30% aqueous ammonia. The catalyst solution was slowly stirred into the silica solution until a homogeneous solution was achieved. The solution was allowed to sit at room temperature until a solid gel had formed.

After the initial wet silica gel preparation, the olegel preparation was done following the procedure described in Chapter 3 of this thesis. The wet gel was allowed to age for x days after initial gelation occurred. After aging in a closed container the gels were broken into smaller pieces of *ca*. 1 cm^3 and placed in a bath of tetrahydrofuran (THF) (Spectrum Laboratories; boiling point = 66 ℃) for three days with the bath solvent being replaced once a day. Subsequently, olegels were prepared from the wet gels by modifying the process described in our previous work,[25] in order to accommodate controlled pre-condensation of the gel as the following.

Once solvent exchange was sufficiently completed, the THF-soaked gels were divided into ten samples. The samples were placed separately in different baths that contained mixtures of oil and THF at various ratios (Table 1), and were allowed to soak for two days and subsequently removed from the baths. The sample names are designated by the oil vol % in the oil/THF mixtures. As a reference, one sample (REF in Table 1) was thoroughly soaked only in a THF bath, by changing the solvent once a day for three days. The oil molecules in the oil/THF mixture outside the gel slowly diffuse through the gel pores. The equilibrium of the diffusion was monitored by color change of the gel. The color intensity did not increase after one day, indicating that the diffusion could reach to an equilibrium within a day. After the soaking steps, all the samples were then placed in a lab oven heated at 70 ℃ for 4 h to

evaporate off the THF, leaving only the oil in the gel pores (olegel preparation).

A small amount of excess oil was dropped onto each olegel sample and the olegel pieces were coated evenly with the oil by rolling the individual pieces around in the added excess oil. This additional oil coating was found to be effective in providing more homogeneous combustion products by minimizing premature oil evaporation from the surface of the olegel pieces. The olegel pieces were then evenly spread on an Inconel dish and placed in an ashing furnace (Carbolite AAF 1100) preheated at 500 ℃. The olegel pieces ignited within 3 – 10 seconds, giving off a large flame before breaking apart into small particulates. The flame ceased within three to six minutes and the material was further kept at 500 ℃ for 10 h under a constant flow of oxygen to completely burn off any carbonaceous species.

5.2.2 Physical Characterization

Powder X-ray diffraction (PXRD) data was collected using a Siemens D5000 diffractometer with a Cu-Kα radiation. High-resolution transmission electron microscopy (HRTEM) was performed on a JEOL JEM 2000FX TEM (LaB_6 source, accelerating voltage 200 kV, PTP resolution 0.28 nm). The TEM samples were prepared by first grinding the pyrogels in an agate mortar in ethanol. A copper grid covered with lacy carbon was submerged in the solution, taken out and then allowed to dry in air. The images were taken under bright field conditions. Scanning

electron microscopy (SEM) studies was performed using ground samples on a FEI XL-30 Environmental SEM using 2 keV electrons. N_2 sorption experiments were carried out with a Micromeritics ASAP2020 volumetric adsorption analyzer), by using nitrogen as the adsorbate at 77K. Prior to the analysis, samples weighing around 150 mg were degassed at 300 ℃ for 10 h under vacuum on the ASAP2020 until a residual pressure of ≤10 μmHg was reached. Specific surface areas were calculated according to the Brunauer-Emmett-Teller (BET) equation using nitrogen adsorption isotherms in the relative pressure range from 0.06 to 0.2. For the calculation of pore size distribution, the desorption branch was considered and the pore volume was obtained from the amount of nitrogen adsorbed at a relative pressure of 0.99. Mesopore size distributions were obtained using the Barrett-Joyner-Halenda (BJH) method assuming a cylindrical pore model.

5.3 Results and Discussion

5.3.1 Synthesis

Highly mesoporous silica particles were prepared with varying pore sizes and pore volumes achieved through changing the oil:THF ratio of the pore liquid and subsequent high temperature combustion. The acid catalyzed sol-gel synthesis of silica wet gels using TEOS as a precursor is a well known and studied procedure. The mixed solution of the base catalyst and silica precursors undergoes gelation within 30 minutes, transitioning from a transparent sol liquid to a translucent gel. Allowing the

gel time to age is crucial in the strengthening of the solid silica network.[27] Aging in the mother-liquor solution of the initial synthesis plays a role in further strengthening the solid network. The unreacted oligomers present in the mother solution as well as the excess water and ethanol, can further undergo hydrolysis and condensation on the surface of the newly formed sol particles, increasing the precipitation of solid material onto the solid network resulting in strengthening of the solid network.

After the initial formation and aging of the wet gel, the procedure closely follows our previous work described in Chapter 4 on the controlled condensation and subsequent gel combustion, rather than supercritical or ambient drying. For the controlled condensation route, the pore liquid is replaced first with THF, although other aprotic-polar solvents can be used. Second, a fraction of the THF is replaced with oil, by soaking the gels in a oil/THF mixture bath with a predetermined oil:THF ratio (the second column in Table 1). Heating of the gels at 70 ℃ cause s the THF, and any unexchanged solvent, to be evaporated off leaving only oil inside of the gel pores. As observed with alumina wet gels, the evaporation of the THF causes the gel to controllably condense meaning that the condensed volume is determined by the volume of the oil present inside of the pores which has been predetermined. Varying the volume of oil in the initial oil:THF mixture allows control over the condensed volume and resulting pore properties of the final material. After the gels have been pre-condensed, they are then combusted to give silica pyrogels. After carbon

burn-off, elemental analysis showed the pyrogels had an average residual carbon content less than 0.5 wt%.

Table 1. Selected properties of SiO_2 pyrogel samples synthesized using castor oil.

Sample	Oil:THF vol. in exchange solvent	BET surface area (m^2/g)	BET surface area from micropore[a] (m^2/g)	BJH pore diameter[b] (nm)	BJH pore volume[c] (cm^3/g)	Porosity[e] (%)
REF	0:100	811	17	3.9	0.9	66
S10	10:90	957	35	7.8	2.1	82
S20	20:80	872	28	7.3	1.8	80
S30	30:70	849	36	6.8	1.7	79
S40	40:60	959	38	6.5	1.8	80
S50	50:50	828	12	6.4	1.6	78
S60	60:40	963	17	6.6	1.9	81
S70	70:30	811	18	7	1.7	79
S80	80:20	788	22	8.4	1.9	81
S90	90:10	687	20	10.4	2.5	85
S100	100:0	632	16	11.3	2.0	82

[a]by the use of *t*-plots with the Harkins-Jura model.

[b]4(total pore volume)/(surface area).

[c]from the pores with the pore width no larger than 150 nm.

[d]from the BJH pore volume and theoretical density of SiO_2

It was observed that the oil containing gels, after the THF had been evaporated off, maintained their initial oil/THF soaked gel shape, with the exception of their apparent shrinkage. The evaporation of the THF did not cause any cracking or breaking apart of the gel pieces. The opacity of the oil filled gels increased with increasing oil content, which could be due to

the microscopic heterogeneity in oil distribution. However, after combustion, it was observed that the resulting silica pyrogels were all completely transparent in appearance. The rapid combustion caused the gel pieces to break apart into a wide distribution of particle sizes ranging form a couple hundred microns to 8 mm. The breaking of the initial gel particle can be attributed to rapid formation of volatile gases in the gel body.[25]

5.3.2. Surface Area and Porosity Analysis

The surface areas, average pore diameters and pore volumes for the silica pyrogels were measured using nitrogen adsorption/desorption methods (Table 1) The adsorption/desorption isotherms for the silica pyrogels are summarized in Figure 5.1. All of the samples showed type IV sorption isotherms with hysteresis loops at relative pressures above 0.6, which is characteristic of mesoporous materials. The estimated BET surface areas for all the samples range from 630 – 960 m^2/g, with majority contribution from mesopores, and appears to not be dependant on the oil/THF mixture due to the absence of trend as the ratio was varied across the samples. When compared to the reference sample which had only THF as a pore liquid, the oil containing samples showed significantly larger surface areas.

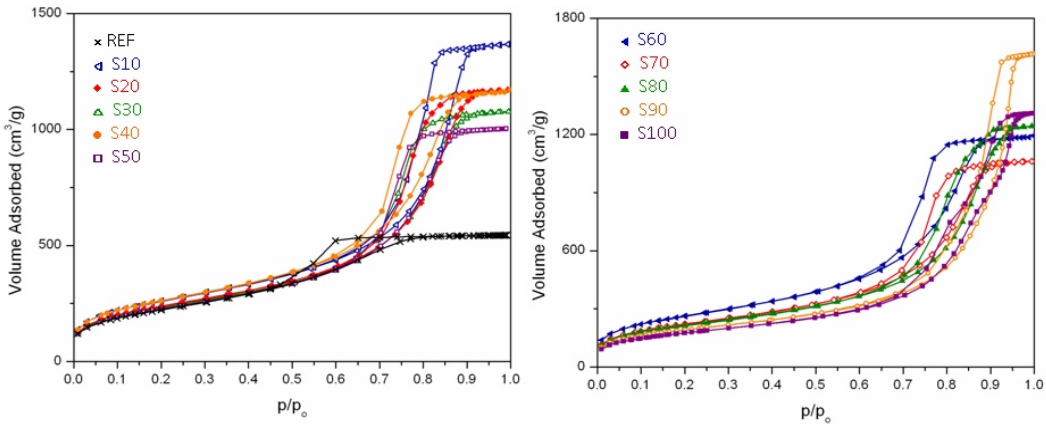

Figure 5.1. N_2 sorption isotherms for silica pyrogel samples synthesized with varying oil volume.

The pore size distribution plots calculated from the desorption branch of the isotherm using the BJH method are shown in Figure 5.2. A general trend can be seen that with increasing oil volume, there is an increase in the broadness of the pore distribution. This could be due to inhomogeneous solvent and oil exchange. As the oil volume % increases in the oil/solvent mixture, the viscosity of the exchanging solution increases, making the full exchange of pore liquid with the oil/solvent mixture diffusion dependent. The heterogeneity of incomplete exchange could cause a wider distribution in pore sizes.

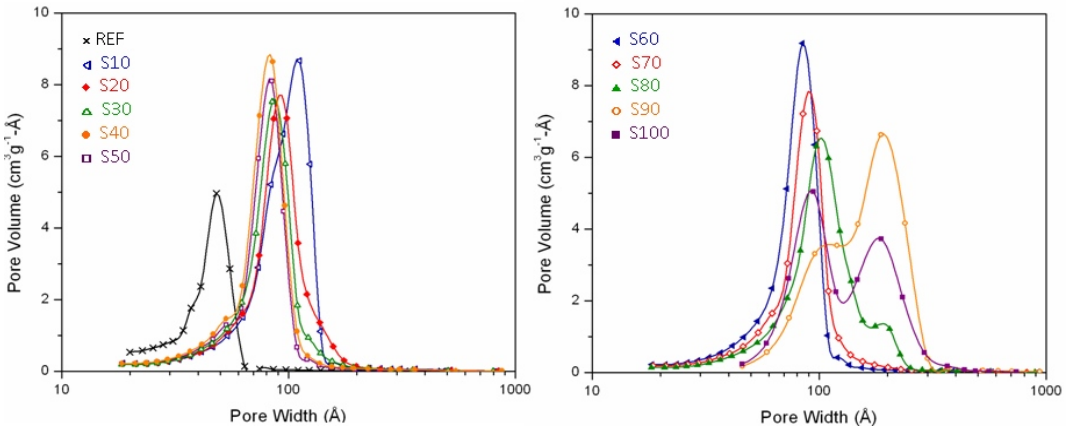

Figure 5.2. Pore distribution curves for silica pyrogel samples synthesized with varying oil volume.

A comparison of total pore volume and average pore width between the silica pyrogel products synthesized with varying oil volume % is graphed in Figure 5.3. The pore width reaches a maximum of 11.3 nm when 100% of the pore liquid is oil and slowly starts to decrease with decreasing volume of oil, reaching a minimum of 6.4 nm when the oil content is about 50 % of the pore liquid. As the oil content decreases further, an increase in pore width is seen, with a second maximum pore width of 7.8 nm is reached when about 10% of the pore liquid is oil. A very similar trend is seen with the pore volume.

A maximum pore volume of 2.5 cm^3/g is achieved when the pore liquid is 90 % oil, and slowly decreases to a minimum pore volume of 1.6 cm^3/g at 50 % oil volume only to slowly increase up to 2.1 cm^3/g when the pore liquid is 10% oil in volume. The maximum pore volume corresponds to 85 % porosity, which is comparable to the porosities of silica aerogels that have been sintered at 500 ℃, and greater than the porosities of

mesoporous silica produced using template methods that have been calcined at 600 ℃. [28] These high porosities and surface areas indicate that the high temperature combustion method with controlled condensing can produce comparable materials synthesized using supercritical drying or expensive templates (Table 2). The small contribution of microporosity to the overall porosity of the pyrogel materials results in a more robust structure.

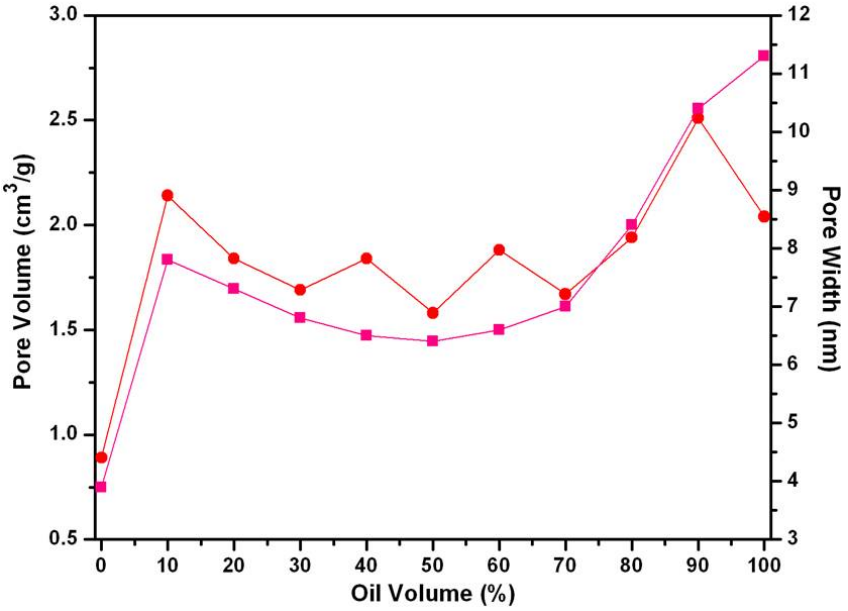

Figure 5.3. Average pore width and pore volume for REF, and S10 – S100.

5.3.3. Electron Microscopy Studies

Scanning electron microscopy was used to evaluate the macrostructure and homogeneity of the surface of the silica pyrogel samples. All of the samples had similar surface morphology, with representative images shown in Figure 5.4 of sample Z4. The samples

had homogeneous surfaces, free of large macropores as evident by the solid appearance of the particle surface. Transmission electron microscopy was used to evaluate the microstructure of the silica materials. The samples all exhibited similar microstructures as well, with the only difference being the density of particles. The lowest porosity product had a larger density of particles in a given area while the highest porosity product had a lower density of particles in a given area. Images from the highest porosity product are shown in Figure 5.5. Homogeneity of the final pyrogel samples was confirmed by examining multiple areas of the TEM grid.

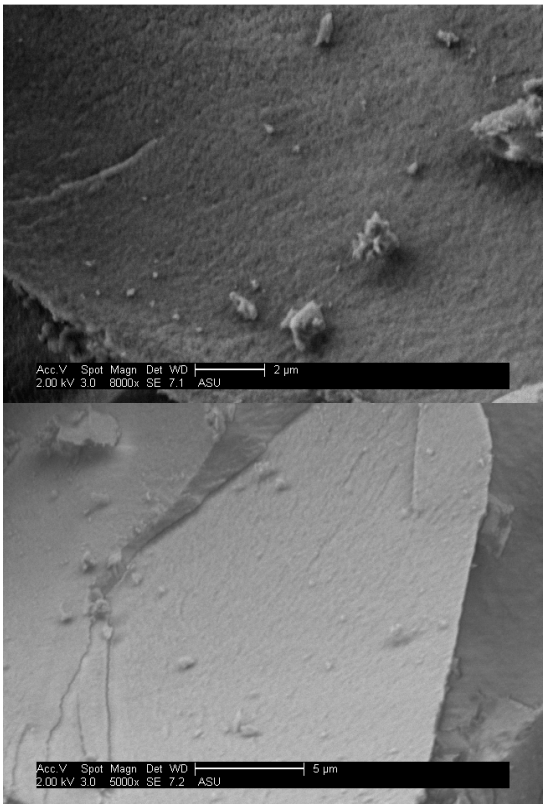

Figure 5.4. SEM images of representative silica pyrogel material.

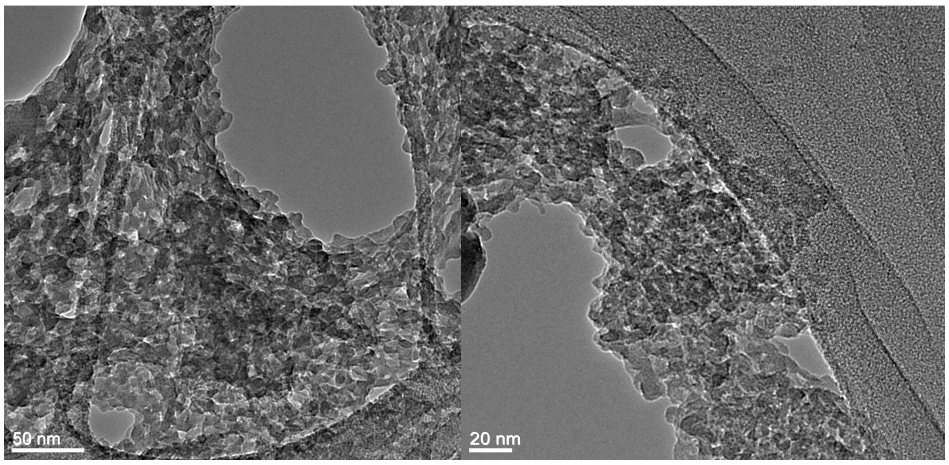

Figure 5.5. TEM images of representative silica pyrogel material

All of the samples exhibited an intricate web-like three-dimensional structure with well-sintered elongated particles. This morphology is significantly different from the morphology typically seen in porous silica xerogels and aerogels produced using a base catalyzed TEOS sol-gel synthesis. For comparison and to verify that the observed morphology was not due to beam damage, several commercially available mesoporous silica samples, Davisil Grade 646, Davisil Grade 12, and chromatography column silica were examined using the exact same TEM sample prep and imaging conditions. The commercially available silica materials had varying particle size across the different samples, but all were composed of semi-spherical particles loosely sintered together forming a textural porosity consistent with that observed in silica aerogels. The highest surface area sample, Davisil 646, had a primary particle size of ~ 10 nm while Davisil Grade 12 and the chromatography column silica had a primary particle size of ~ 20 nm. Beam damage could be ruled out as

there was no change in particle shape, size, or morphology after extensive time of beam exposure to the same area of a particle for both the commercially available silica and the silica pyrogel particles.

Table 2. Comparison of commercially available and recently reported mesoporous silica materials.

	BET surface area (m^2/g)	BET surface area from micropores (m^2/g)	BJH pore diameter (nm)	BJH pore volume (cm^3/g)	Porosity (%)
SiO_2 Aerogel	>1600	NR	20 – 150	1.8 - 130	80 – 99.8
Davisil Grade 646[a]	746	201	3.7	0.15	25
Davisil Grade 12[a]	308	70	12.3	1.1	70
Column Chromatography SiO_2[a]	361	67	8.5	0.9	67
Ordered SiO_2 from template synthesis[b]	670	NR	21	2.2	83
SiO_2 pyrogel S90	687	20	10	2.5	85

[a]Purchased from Sigma-Aldrich

[b]Sample MSU-J-TEOS-65 ℃ from Jiao *et al.*[28]

The ultra high porosity of aerogels is desirable for application purposes, however, it leads to very weak structural integrity.[24] The porosity of the reported pyrogels is lower than that of synthesized silica aerogels but the structural strength of the pyrogels is much greater that that of fragile aerogels. In order to assess the general robustness of the newly afforded silica pyrogels, the materials were soaked in various solvents such as water, ethanol, acetone, and hexanes and observations

were made about the structural integrity of the material afterwards. Two mechanical robustness tests were carried out. The first was by dropping small drops of liquid onto the particles, allowing the liquid to be absorbed by the particle and observing the change in macroscopic structure of the particle. The liquids were rapidly absorbed by the particles, with the lowest surface tension liquids being absorbed the fastest. One the liquid was absorbed the particle remained completely in-tact and not cracking or breaking could be observed. The particle maintained its original shape and no visible changes could be seen. Repeated wetting of dry particles showed that the silica pyrogels were able to absorb liquids without any visible change or damage to the solid structure.

The second test was done by dropping the silica particles into a large volume of solvent. The particles initially floated on the surface of the liquids, until the diffusion of the liquid through the solid caused the particles sink. The higher the surface tension of the liquid, the longer it took for the particles to sink and solvents with very higher surface tension like water, respectably, required the particles to be shaken into the solution in order to allow the diffusion of the liquid through the material. Once the particles sank to the bottom, the solutions were shaken for several seconds, allowing the particles to become dispersed in the liquid. The amount of time it took for the particles to sink back down to the bottom of the container was compared to the standard silica materials, fumed silica, Davisil Grade 646, Davisil Grade 12, and Column

chromatography silica. It was observed that the silica pyrogel materials sank to the bottom seconds faster then the Davisil and column chromatography silica. Fumed silica stayed dispersed in solution for one day. The mechanical robustness of the silica pyrogels along with being able to be easily dispersed and re-collected in a solution without structural collapse and maintaining a high porosity makes them a perfect candidate for applications that require soaking, impregnation, filtration or separation steps.

The unique well-sintered morphology and resulting increased mechanical robustness of the pyrogel is most likely due to the high temperature combustion of the oil inside of the pores. Around 500 ℃, the residual alkoxide moieties present on the surface of the solid network begin to burn off causing the condensation of neighboring silanols.[24] This condensation eliminates surface reactive sites, but does not contribute to the densification or increased mechanical robustness of the solid network. It is not until temperatures greater than 850 ℃ that the sintering of silica particles under viscous flow occurs. The increased formation of siloxane bonds results in densification of solid structure. [22-24]

When the oil-filled gels are combusted, the actual temperature that the particle “sees” is much greater than the 600 ℃ temperature of the oven due to the heat of combustion of castor oil (38.65 kJ/g). This temperature is great enough to cause sintering of the individual silica particles creating the well sintered web-like morphology seen in the

pyrogel products. However, the time that the particles are exposed to these high temperatures is on the order of tenths of a second, resulting in only slight sintering and densification. This “flash-sintering” greater preserves the initial solid structure of the oil soaked gel giving products with higher porosity and equal or greater mechanical robustness as compared to aerogels sintered at 900 ℃ for 10, 30, an d 60 minutes.[24]

5.4 Conclusion

High temperature combustion of oil filled silica wet gels with initial pre-condensing has been shown to produce highly mesoporous transparent silica particles with controllable pore size and pore volume. The quick sintering of primary particles during the combustion step results in a unique, web-like morphology that contributes to increased mechanical robustness of the final product without sacrificing porosity or surface area. It has already been shown that the high temperature combustion aids in dehydration of certain hydrous metal oxide gels, but in the case of silica, this work newly shows that the combustion step aids in the formation of a new, unique, well sintered solid network while removing the pore liquid and preserving the porous network structure simultaneously. This strengthening of the solid leads to a material that can be immersed into various liquids without destruction to the porous structure as well as a material that can be dispersed in a liquid and recovered quickly, all while avoiding the use of expensive drying techniques or template precursors.

5.5 References

(1) Iler, R. K. *The Chemistry of Silica*; Wiley New York, 1979.

(2) Brinker, C. J.; Scherer, G. W. In *Sol-Gel Science*; Academic Press: Boston, 1990, p 97.

(3) Kistler, S. S. *Nature (London, United Kingdom)* **1931**, *127*, 741.

(4) Blanchard, F.; Reymond, J. P.; Pommier, B.; Teichner, S. J. *Journal of Molecular Catalysis* **1982**, *17*, 171.

(5) Bond, G. C.; Flamerz, S. *Applied Catalysis* **1987**, *33*, 219.

(6) Pajonk, G. M. *Applied Catalysis* **1991**, *72*, 217.

(7) Wang, L.; Eguchi, K.; Arai, H.; Seiyama, T. *Applied Catalysis* **1987**, *33*, 107.

(8) Rolison Debra, R. *Science (New York, N.Y.)* **2003**, *299*, 1698.

(9) Fricke, J.; Caps, R.; Buettner, D.; Heinemann, U.; Huemmer, E.; Kadur, A. *Solar Energy Materials* **1987**, *16*, 267.

(10) Fricke, J.; Reichenauer, G. *Journal of Non-Crystalline Solids* **1987**, *95-96*, 1135.

(11) Tewari, P. H.; Hunt, A. J.; (United States Dept. of Energy, USA). Application: US
US, 1986, p 6 pp.

(12) Tewari, P. H.; Hunt, A. J.; Lofftus, K. D. *Springer Proceedings in Physics* **1986**, *6*, 31.

(13) Gronauer, M.; Fricke, J. *Acustica* **1986**, *59*, 177.

(14) Gibiat, V.; Lefeuvre, O.; Woignier, T.; Pelous, J.; Phalippou, J. *Journal of Non-Crystalline Solids* **1995**, *186*, 244.

(15) Gesser, H. D.; Goswami, P. C. *Chemical Reviews (Washington, DC, United States)* **1989**, *89*, 765.

(16) Poelz, G.; Riethmueller, R. *Nuclear Instruments & Methods in Physics Research* **1982**, *195*, 491.

(17) Aspen aerogels. 2011.

(18) Nanopore **2008**.

(19) Gurav, J. L.; Jung, I.-K.; Park, H.-H.; Kang, E. S.; Nadargi, D. Y. *Journal of Nanomaterials* **2010**, No pp given.

(20) Gurav, J. L.; Nadargi, D. Y.; Rao, A. V. *Applied Surface Science* **2008**, *255*, 3019.

(21) Gurav, J. L.; Rao, A. V.; Bangi, U. K. H. *Journal of Alloys and Compounds* **2009**, *471*, 296.

(22) Gurav, J. L.; Rao, A. V.; Nadargi, D. Y.; Park, H.-H. *Journal of Materials Science* **2010**, *45*, 503.

(23) Gurav, J. L.; Rao, A. V.; Rao, A. P.; Nadargi, D. Y.; Bhagat, S. D. *Journal of Alloys and Compounds* **2009**, *476*, 397.

(24) Lucas, E. M.; Doescher, M. S.; Ebenstein, D. M.; Wahl, K. J.; Rolison, D. R. *Journal of Non-Crystalline Solids* **2004**, *350*, 244.

(25) Ladd, D. M.; Volosin, A.; Seo, D.-K. *Journal of Materials Chemistry* **2010**, *20*, 5923.

(26) Ernest Orlando Lawrence, B. N. L.

(27) Brinker, C. J.; Scherer, G. W. In *Sol-Gel Science*; Academic Press: Boston: 1990, p 357.

(28) Jiao, J.; Sun, X.; Pinnavaia, T. J. *Polymer* **2009**, *50*, 983.

CHAPTER 6

SYNTHESIS OF HIGHLY POROUS YTTRIA-STABILIZED ZIRCONIA FROM INTERPENETRATING INORGANIC/ORGANIC NETWORKS

6.1 Introduction

Zirconia is one of the best known corrosion-resistant, refractory materials[1] and exhibits several unique properties making it a versatile materials. Zirconia shows chemical inertness under most conditions, but can be catalytically active if treated with sulfur. At ambient temperature, it is an electrical insulator but if mixed with tetravalent oxides can form a high temperature ionic conductor. Additionally, zirconia-metal oxide alloys exhibit high-strength, low-fracturing properties, which when combined with its low thermal conductivity makes it a desirable material for thermal barrier coatings in turbine engines. Zirconia is a polymorphic oxide, whose stable structure is monoclinic at temperatures under 1170ºC, tetragonal from 1170-2370ºC, and cubic at temperatures above 2370ºC.[2] The high temperature cubic phase is the most desirable phase for oxide conduction applications, and can be stabilized at room temperature by forming oxygen vacancies through substitution of Zr^{4+} with alkaline earth or rare earth cations. Yttria has been used as a stabilizer in zirconia parent-lattices to form partially stabilized or fully stabilized cubic zirconia materials (YSZ), depending on the substitution percentage.[3-6] It has been found that substitution of 8 – 10 mol% of Y_2O_3, corresponding to either full cubic stabilization or mixed tetragonal-cubic stabilization, is the most

practical for electrolyte applications, with the optimal being around 8 - 9 mol%.[7]

YSZ materials with high surface area and mesoporosity are highly desirable for solid oxide fuel cell applications as well as uses as gas sensors,[8] catalyst substrates[9] and membranes.[10] Different approaches have been taken to try and synthesize highly porous YSZ materials, with recent advances using block copolymers[11] and sol-gel technique to synthesize aerogels.[12,13] The later produced YSZ particles that were thermally stable after supercritical drying but then experienced structural collapse during the necessary heating step at 550ºC for the transition to a crystalline product. The former was able to achieve an ordered mesoporous material whose structure was stable up to 500ºC but then observed a significant decrease in surface area and pore volume when heated to 800ºC, all while requiring the use an expensive block-copolymer as an initial precursor. It is apparent that the synthesis of mesoporous YSZ materials is not trivial and there is a need for a synthetic procedure that does not require expensive, reactive precursors all while producing a product that is able to maintain its porous structure at high temperatures, is desirable.

Recently, Volosin *et al.* reported a one-pot synthesis of interpenetrating inorganic and organic gel networks to form mesoporous antimony-doped tin oxide (ATO).[14] Precursor solutions of inorganic salts, resorcinol and formaldehyde were initially mixed together. An epoxide was

then added to slowly increase the pH causing the gelation of the inorganic precursors. The gel was then heated to 70ºC to induce the gelation of the resorcinol formaldehyde (R-F) precursors present inside of the pores formed by the inorganic solid network. The solvent was then evaporated out of the composite gel, forming a xerogel, which was pyrolyzed at 500ºC to remove the R-F gel while dehydrating the ATO gel resulting in a crystalline, mesoporous ATO material. The key to this method is the sequential gelation (versus simultaneous gelation) of the inorganic and organic precursors, ensuring that the inorganic solid network is completely formed into a continuous network before the organic gel forms inside of the pores, acting as a sacrificial support. The synthesis of other metal oxides, such as YSZ, utilizing concurrent gelation and the formation of interconnecting inorganic and organic networks may provide an easy, one-pot method that produces mesoporous, crystalline YSZ materials.

6.2 Experimental Section

6.2.1 Synthesis of YSZ Gels

Multiple samples were prepared by varying two different synthetic parameters, the concentration of the zirconium precursor and the concentration of the melamine precursor. The specific concentrations for each sample are listed in Table 1. It should be noted that while it is stated that the concentration of zirconium and melamine were varied, the concentration of ytrrium and formaldehyde precursor were also adjusted

accordingly so that the final Zr/Y mole ratio was 5.13 (9% Y_2O_3) and the melamine/formaldehyde molar ratio was 3.6 for all samples.

In a typical synthesis the sample was prepared by making two precursor solutions. The first, being the inorganic precursor solution, was prepared by dissolving 2.3 g of $ZrCl_4$ in 8.0 g of deionized water followed by dissolving 0.6 g of $YCl_3 \cdot 6H_2O$, producing a precursor solution that had a pH of about 1. The second solution, being the organic precursor solution, was prepared by dissolving 7.0 g of melamine in 10.5 g of dionized water and 8.3 g of 90% ethanol followed by the addition of 16.2 g of 37 w/w% formaldehyde solution (Sigma-Aldrich, 7-8% methanol as stabilizer). Due to the limited solubility of melamine in water, the organic solution was heated to 90ºC in a sealed container, to ensure complete dissolution of the melamine and then allowed to cool to room temperature producing a precursor solution that had a pH of about 6. The inorganic precursor solution was then added slowly to the organic precursor solution while stirring vigorously, and continued stirring for 2 minutes until a homogeneous solution was achieved. After stirring, the solution was allowed to sit, and gelation occurred in about one minute with the final pH dependent on the concentration of the organic and inorganic precursors, as reported in Table 1. The gel was sealed and aged at room temperature for one day, in which a hard solid white gel monolith formed. The gel was subsequently placed in an oven at 70ºC for three days after which the gel shrank by 5 vol %.

The monolithic composite gel was then removed and broken up prior to being air-dried for several days. The drying caused the composite materials to significantly shrink. The xerogels were then heated in an ashing furnace for 10 hours at 600ºC to produce a white material that had a fluffy, airy texture. Calcination variation experiments were carried out by further heating the mesoporous YSZ product to 800, 900, 1000, and 1100ºC, resulting in a denser looking material.

6.2.2. Physical Characterization

Particle size and phase information were determined using powder X-ray diffraction (PXRD), with the data collected using a Siemens D5000 diffractometer with a Cu-Kα radiation. Further phase information was collected using Raman spectroscopy. Data was collected using a custom built Raman spectrometer in a 180 ° geometry. The sam ple was excited using a 100 mW Compass 532 nm laser coupled with an Acton 300i spectrograph and a back thinned Princeton Instruments liquid nitrogen cooled CCD detector. Data was collected from 200 to 800 cm^{-1}. Transmission electron microscopy (TEM) was performed on a JEOL JEM 2000FX TEM (LaB_6 source, accelerating voltage 200 kV, PTP resolution 0.28 nm). TEM samples were prepared by first grinding the material in an agate mortar in ethanol. A copper grid covered with lacy carbon was submerged in the solution, taken out and then allowed to dry in air. The images were taken under bright field conditions and slightly defocused to increase contrast. Scanning electron microscopy (SEM) studies was

performed using ground samples on a FEI XL-30 Environmental SEM using 5 keV electrons.

N_2 sorption experiments were carried out with a Micromeritics Tristar II 3020 at 77K. Prior to the analysis, samples weighing around 300 mg were degassed at 300 ℃ for 10 h under a continuous flow of nitrogen at ambient pressure. Specific surface areas were calculated according to the Brunauer-Emmett-Teller (BET) equation using nitrogen adsorption isotherms in the relative pressure range from 0.06 to 0.2. For the calculation of pore size distribution, the desorption branch was considered and the pore volume was obtained from the amount of nitrogen adsorbed at a relative pressure of 0.99. Mesopore size distributions were obtained using the Barrett-Joyner-Halenda (BJH) method assuming a cylindrical pore model. Elemental analysis was performed with Perkin-Elmer 2400 Series II CHNS/O Analyzer in order to estimate with the amount of residual carbon in the products.

6.3 Results and Discussion

6.3.1 Synthesis

The overall synthetic procedure for the synthesis of highly mesoporous YSZ is illustrated in Figure 6.1. An inorganic-organic composite gel is produced by the sequential formation of a hydrous YSZ gel network proceeded by the formation of a melamine-formaldehyde (M-F) gel network, with the two networks interpenetrating each other. The synthesis is carried out by initially dissolving the organic and inorganic

precursors separately, due to the limited solubility of the melamine in water and the hydrolysis rate of $ZrCl_4$. This ensures complete dissolution of all the precursors. The MF precursor solution had an initial pH of 6 while the Zr and Y precursor solution had an initial pH of 1 due to the hydrochloric acid generated during the hydrolysis of $ZrCl_4$ and $YCl_3 \cdot 6H_2O$. The two precursor solutions are then mixed together in one pot in which vigorous stirring is required in order to obtain a homogeneous solution. The pH of the mixed solution varied from 1 - 4 depending on the concentration of organic precursors. A weak, opaque gel forms within about two minutes after stirring has ceased and subsequently a hard, white gel is formed after 24 h.

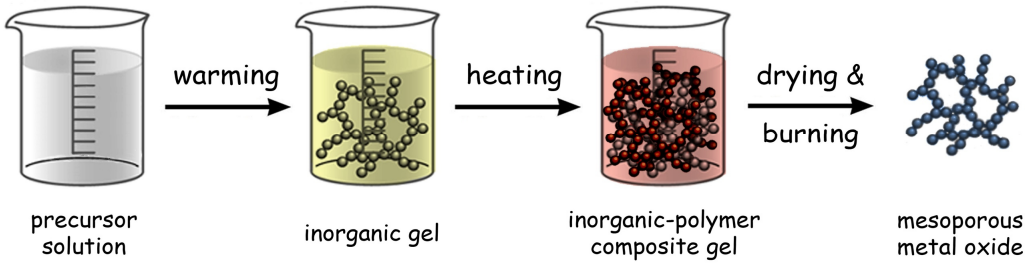

Figure 6.1. Synthetic procedure for interpenetrating organic/inorganic gel network.

The initial gelation point is attributed to the formation of the inorganic network as supported by several different factors that would induce this formation. First, zirconium and yttrium salts can undergo pH initiated hydrolysis and condensation to form sol-gel materials, however this process usually requires the presence of an acid scavenger, such as

an epoxide, to cause the slow increase in pH.[15] Slow consumption of the acid increases the pH of the solution and results in the precipitation of sol particles which then condense together forming the spanning network of the inorganic gel. In the presented synthesis, the only source for the acid to be consumed by is the organic precursors. It was found in a control experiment that no gelation or visible change in viscosity occurred when $ZrCl_4$ and $YCl_3 \cdot 6H_2O$ salts were dissolved in water without the presence of M-F precursors, supporting that another source must act on the system to induce gelation.

The exact mechanism of this initial gelation is not known and is outside the scope of this thesis, but a possible explanation is presented. Acidic conditions are required to promote the condensation of intermediates in the polymerization of melamine and formaldehyde.[15] However this catalyzed process is only effective at elevated temperatures typically above 60ºC[16-18]. The increase in pH observed in our MF-YSZ systems, which results in the initial gelation of the inorganic network, indicates that the acid present is slowly being consumed, possibly by MF polymerization taking place at room temperature. A similar effect at room temperature has been observed in ATO-RF composite gels.[14] The change in color of the gel from opaque to white over 24 h after initial gelation also supports that some extent of polymerization is occurring between the melamine and formaldehyde monomers. Control experiments showed that pure YSZ gels formed using an epoxide-addition sol-gel route with

water/ethanol ratios equivalent to those in the MF-YSZ composite synthesis, are opaque in color. The white color observed could then be due to the change in light scattering as the organic monomers present inside of the pores of the YSZ network, start to form longer, polymeric chains.

The second factor that would support the initial formation of the inorganic network is the decreased solubility of the YSZ sol particles in ethanol. The final solution, after the organic and inorganic precursors solutions were combined, contained up to 42% ethanol by volume as compared to the initial inorganic precursor solution which contained only deionized water. The decrease in solubility of the sole particles in this ethanolic environment induces rapid condensation of the formed oligomers and results in decreased gelation time.[12] Upon subsequent heating at 90ºC, the M-F polymerization fully occurred in the hydrous YSZ gel to give a very hard, solid white gel. It is plausible that the acid present from the inorganic precursors may catalyze the polymerization. However, it has been shown that the inorganic gel network itself may also promote polymerization,[14] owing to the fact that high valent metal oxides can act as Lewis acids.[19,20] Both the acid present from the precursors and the pre-formed YSZ gel network could play a role in catalyzing the M-F polymerization.

The YSZ/M-F composite gels were then dried in air to form composite xerogels and then subsequently heated to 600ºC for 10 h to

ensure complete combustion of the organic component. Elemental analysis shows that the residual carbon content is less than 0.4 wt% for the samples which supports that the organic component of the composite gel can be almost completely removed without leaving any significant amount of carbon residue in the final product.

6.3.2. Powder X-ray Diffraction

Preliminary phase information can be deduced from x-ray diffraction. All samples exhibited similar patterns, independent of precursor concentrations, with the XRD pattern of the sample with highest organic precursor concentration, Z4, shown in Figure 6.2. After removal of the organic component of the composite gel and calcinations at 600ºC, all of the YSZ materials showed almost identical diffraction patterns with semi-broad Bragg reflection peaks, indicating crystallinity of the product as well as small particle size. All of the refection peaks could be assigned to either tetragonal or cubic phase of YSZ, with no evidence showing the presence of the low temperature monoclinic phase. XRD can be used to rule out the presence of the monoclinic phase however it is known that the small atomic scattering factor of oxygen makes it difficult to distinguish between the tetragonal and cubic phases near the phase boundary, which occurs at 8-10 mol% stabilization with Y_2O_3.[21] All of the YSZ materials presented are 9.09% Y_2O_3 stabilized, falling within this range. The significant difference between the diffraction patterns of the tetragonal phase vs. the cubic phase is the formation of doublets, or ‘splitting’, of

several of the peaks due to the elongation of the *c* axis. This distinction becomes increasingly difficult in nanocrystalline materials because of the peak overlap due to crystallite size broadening effects.[22]

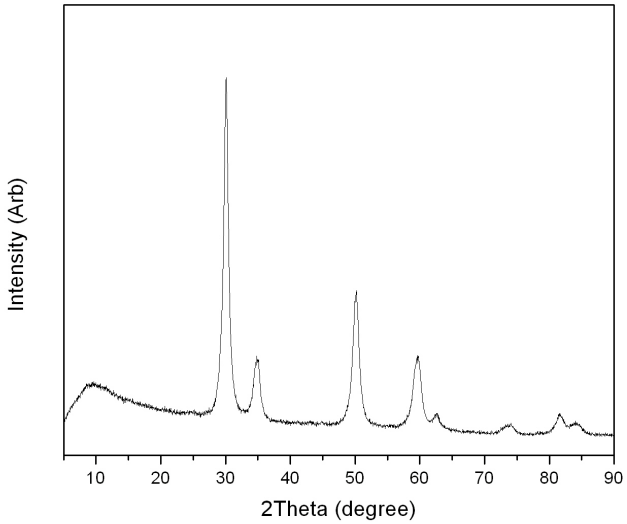

Figure 6.2. XRD pattern of M-F YSZ sample Z4.

6.3.3 Raman Spectroscopy

Primary phase information as well as identification of any transition from cubic to tetragonal phase was determined using Raman spectroscopy. The crystallographic structure of cubic and tetragonal YSZ as well as a full discussion addressing the use of Raman spectroscopy for phase identification has been given in Chapter 1 and Chapter 2. The Raman spectra for the samples with varying organic precursor concentration are show in Figure 6.3. The Raman spectra for the sample with the highest M-F concentration, Z4, show some tetragonal characteristic with peaks at 260, 323, 468, and 642 cm^{-1} along with a broad peak from 580 to 620 cm^{-1} indicative of the cubic phase. Simply

reducing the concentration of M-F from 1.75 M to 1.43 M, sample Z3, reduces the amount of tetragonal character drastically, with very weak features at 260, 336, 465, and 635 cm^{-1} still present but a significant cubic phase broad peak from 590 to 630 cm^{-1}. By further reducing the amount of M-F, samples Z2 and Z1, a continued decrease in the amount of tetragonal phase can be seen. The lowest M-F concentration sample, Z1, shows only three very broad features around 250, 330 and 450 cm^{-1}, and is dominated by a broad peak present between 570 and 650 cm^{-1}. This presence of tetragonal phase in 9.09 mol% Y_2O_3 YSZ systems is consistent with what has been observed before in the synthesis of YSZ aerogels,[12] where full cubic stabilization could only be achieved with 17 mole % Y_2O_3.

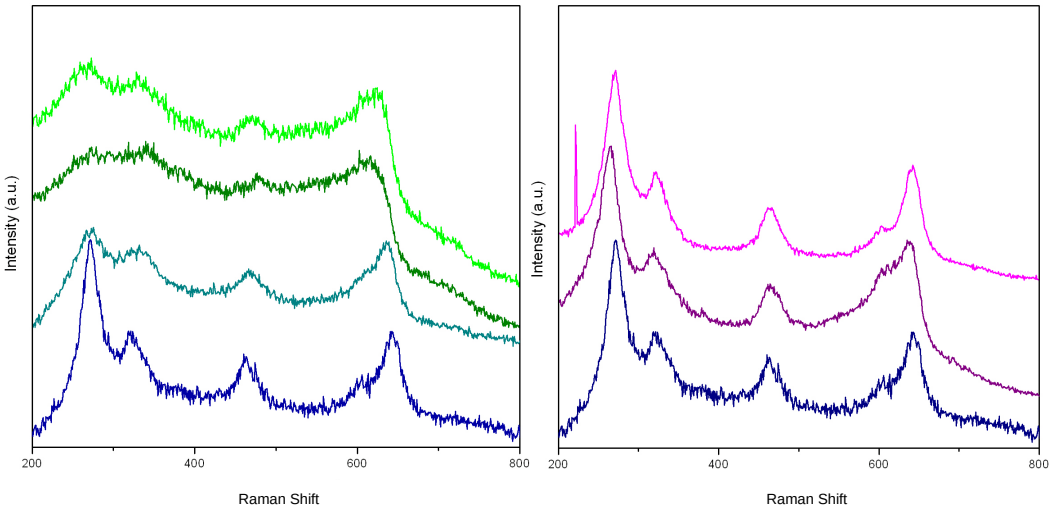

Figure 6.3. Raman spectra of samples with varying M-F content Z1, Z2, Z3, Z4 (left, listed top to bottom) and varying YSZ content Z6, Z5, Z4 (right, listed top to bottom).

For solid oxide fuel cell applications it has been found that the material

with cubic structure at the lowest stabilization limit (8-10 mol %) shows the highest ionic conductivity, making our synthesized YSZ materials very near to having the desired properties for use in such application.

When the concentration of the inorganic precursors was varied, it was found that there was little effect on the phase composition of the final YSZ material. Raman spectra are shown in Figure 6.3 for the series Z4, Z5 and Z6, where the M-F concentration was held constant and the zirconium precursor concentration decreased. The spectra show four broad peaks that can be assigned to the tetragonal phase as well as one broad shoulder/peak in the range of 570 to 640 cm^{-1} which can be assigned to the cubic phase. It can be concluded that the inorganic precursor concentration is not a critical parameter in controlling what phase is formed in the final material.

6.3.4 Electron Microscopy

Macroscopic structural features of the YSZ materials were examined through SEM studies on ground samples. All seven products had similar microscopic features, with representative images shown in Figure 6.4, of sample Z4 which had the highest porosity. The powder samples show a homogeneous textured surface with the absence of hard, dense agglomerates or any other heterogeneous aggregation.

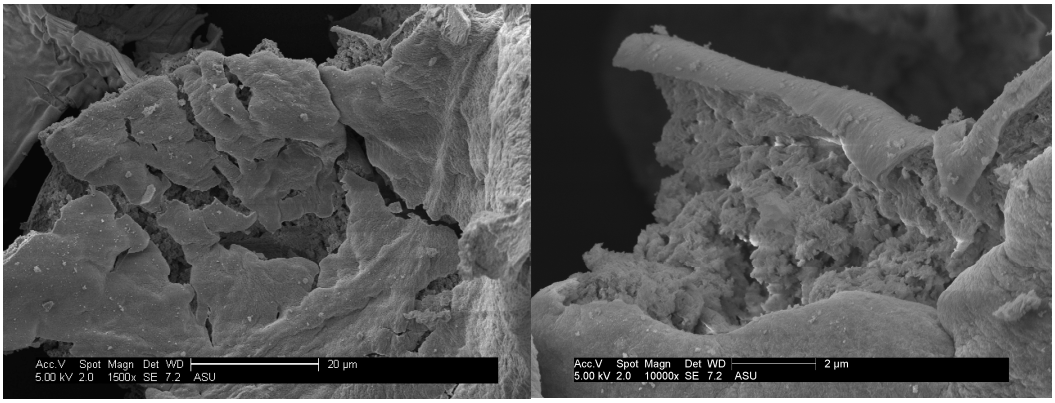

Figure 6.4. SEM micrographs of highest porosity sample, Z4, at low magnification (left) and high magnification (right).

Primary particle and nanoscopic structure studies were conducted using TEM. All samples showed very similar structures, with a representative image shown in Figure 6.5 of sample Z4 which had the highest porosity. The observations of round primary particle shape sintered together forming a large porous cluster network forming textural porosity is similar to the structures observed in previously reported YSZ aerogel particles synthesized from sol-gel routes.[12,15] The crystalline nature of the particles is confirmed by the presence of lattice fringes as shown in higher magnification image of Figure 6.5, which is consistent with the Bragg peaks observed in the collected XRD patterns. The average particle size of 18.5 nm determined by TEM is slightly larger than the average crystallite size of 13.0 nm calculated from XRD. The difference between the two determined sizes could be attributed to two possible factors; the first is peak broadening in the XRD pattern due to the presence of both tetragonal and cubic phase. The second factor could be that one primary

particle may be composed of more then one crystallite, making the primary particle size observed in TEM larger then the crystallite size calculated from XRD.

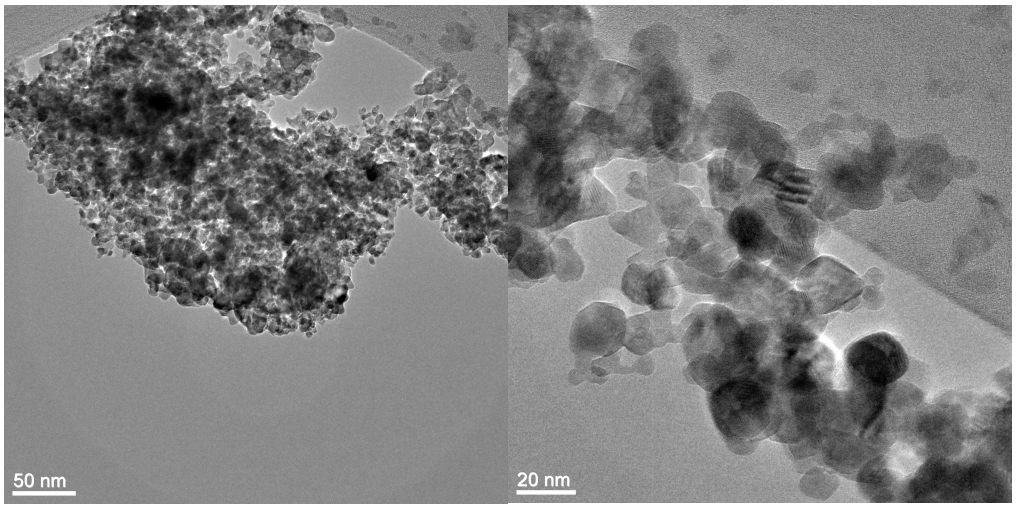

Figure 6.5. TEM micrographs of the highest porosity sample, Z4, at low magnification (left) and high magnification (right).

6.3.5 Surface Area and Porosity Analysis

The surface areas, average pore diameters and pore volumes for the porous YSZ products were measured using nitrogen adsorption/desorption analysis and are summarized in Table 1. YSZ materials which were prepared with a melamine concentration of 1.75 had consistent BET surface areas ranging from 73 to 76 m^2/g with the change of concentration of zirconium having little effect on the resulting surface areas of the products. The adsorption isotherms for samples Z4, Z5, and Z6 are almost identical (Figure 6.6), showing a hysteresis loop starting at relative pressure of 0.5, indicating mesoporosity, The YSZ materials that

were made with a zirconium concentration of 0.25 with varying concentration of melamine had BET surface areas ranging from 76 to 87 m^2/g, with a trend seen that increased melamine concentration samples showed an increase in volume of N_2 adsorbed, as indicated by their isotherms (Figure 6.7).

Table 1. Selected properties of YSZ synthesized using inorganic-organic interpenetrating network with varying inorganic and organic precursor concentrations.

Sample	$[Zr^{+4}]$ (mol/L)	[Melamine] (mol/L)	pH at gelation point	BET surface area (m^2/g)	BJH pore diameter[a] (nm)	BJH pore volume[b] (cm^3/g)
Z1	0.25	0.59	1	54	4.7	0.06
Z2	0.25	1.05	2	87	6	0.16
Z3	0.25	1.43	3.5	85	8.3	0.21
Z4	0.25	1.75	4	76	12.4	0.26
Z5	0.23	1.75	4	72	12.2	0.25
Z6	0.21	1.75	4	73	11.6	0.26

[a] 4(total pore volume)/(surface area).

[b] from the pores with the pore width no larger than 150 nm.

[c]from the BJH pore volume and theoretical density of 9 mol% YSZ

However, it should be noted that sample Z1, which had the lowest concentration of melamine at 0.59 M, has a drastically lower BET surface area. This could be due in part to the incomplete formation of a solid inorganic gel network. The pH of the combined solution of the inorganic and organic precursors was 1 for sample Z1. It is known that the rate of

condensation and subsequent precipitation of sol particles is pH dependent, and at low pH, the rate of condensation is very slow as well as the low pH inhibits the precipitation of the newly formed oligomers. Without an increase in pH, the inorganic precursors can only form a weakly spanning solid, which results in a weak inorganic solid structure. This weak solid structure will not be able to further withstand the removal of the polymerized organic gel support inside of the pores, resulting in pore collapse forming larger particles giving a smaller specific surface area. All of the YSZ products exhibited a Type IV isotherm, with a plateau at high relative pressure and a closed desorption hysteresis loop, indicative of mesoporous materials.[23]

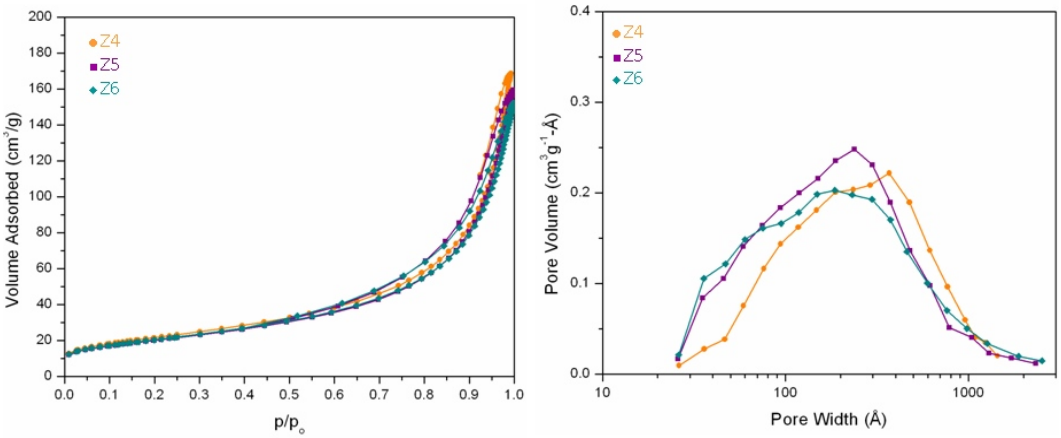

Figure 6.6. N_2 isotherm (left) and BJH pore distribution plots (right) for M-F YSZ samples Z4, Z5, and Z6.

A trend can be seen in the BJH pore volume as the concentration of organic precursor is varied Table 1. The pore volume increases from 0.06 to 0.26 cm^3/g as the concentration of melamine is increased from 0.59 to 1.75 M. This trend is in agreement with the conclusion that the M-F

gel is forming an interpenetrating network and is taking on the role of a hard template. As the physical volume of the solid organic network is increased, by increasing the concentration of the organic precursors, the pore volume that the inorganic gel is able to maintain during solvent evaporation and subsequent removal of the organic gel also increases. These results are consistent with other inorganic-organic composite systems synthesized using a similar route.[24]

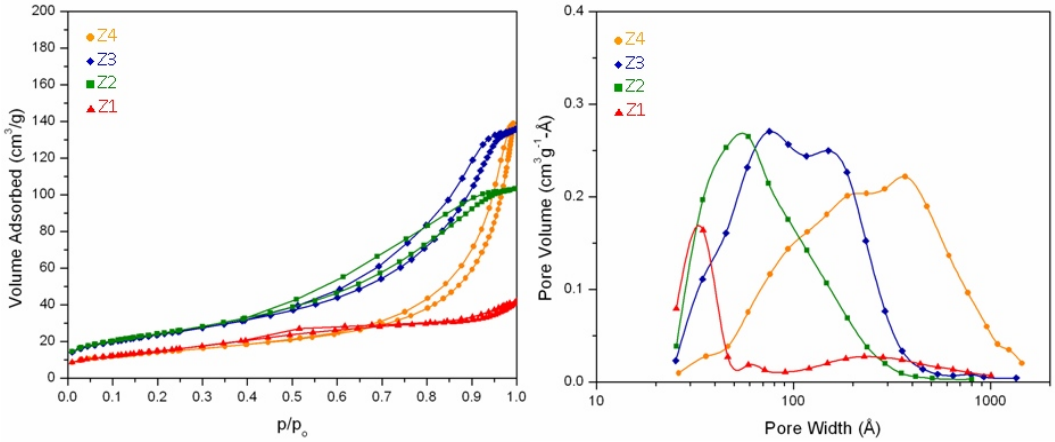

Figure 6.7 N_2 isotherm (left) and BJH pore distribution plots (right) for M-F YSZ sample Z1, Z2, Z3, Z4.

The increase in pore volume with increasing organic precursor concentration is accompanied by an increase in pore size. The BJH pore distribution, Figure 6.7, shows maxima at 2, 4, 8, and 30 nm for samples Z1, Z2, Z3, Z4 respectively. By varying the amount of the organic gel component in the organic-inorganic composite gel, the resulting YSZ products can have volume porosities varying from 27 to 61 %, which is estimated roughly from the pore volumes and theoretical density of 9 %

YSZ. To our knowledge, this is the highest porosity achieved in the synthesis of mesoporous YSZ materials after calcination at 600ºC, even when compared to ordered porous YSZ materials synthesized using templating techniques.[11]

Changing the inorganic precursor concentration had little effect on the resulting pore size and pore volume of the final YSZ products (Figure 6.6). All three samples that had equal M-F concentrations but varying zirconium concentrations resulted in materials with average pore diameters of ~12 nm and pore volumes of ~0.26 (Table 1). It can be concluded that varying the inorganic component within the range allowed by the synthesis to produce homogeneous products, has little effect on the surface area and pore properties of the final material.

6.4 High Temperature Studies

High temperature studies were carried out on the highest porosity product, Z4, after initial removal of the organic gel component and calcination at 600ºC for 10 hr. Each sample was subsequently heated for 10 hours at the indicated temperature, ranging from 800 to 1100ºC. The naming convention for this set of samples is the sample name followed by the calcination temperature (Z4_calcination temperature).

Table 2. Selected properties of sample Z4 calcined at various temperatures.

Sample	BET surface area (m^2/g)	BJH pore diameter[a] (nm)	BJH pore volume[b] (cm^3/g)	Porosity[c] (%)
Z4_600	72	14	0.28	63
Z4_800	34	27	0.24	59
Z4_900	26	31	0.19	54
Z4_1000	15	29	0.1	35
Z4_1100	8	33	0.05	23

[a] 4(total pore volume)/(surface area).

[b] from the pores with the pore width no larger than 150 nm.

[c] from the BJH pore volume and theoretical density of 9 mol% YSZ

The specific surface area decreases with increasing calcination temperature (Table 2) and can be correlated to the increase in crystallite size, as calculated from the XRD pattern and confirmed with TEM, as well as the increase in average pore diameter as the particles are further sintered together. The sintering of particles and loss of porosity due to structural changes in the solid framework is expected with increased calcination temperature for highly porous YSZ materials, of which most see loss of porous structure at temperatures below 800 ºC[11,13,15] It was observed that the densification effects of sintering are minimal up to temperatures of 900 ºC, with the final material having a pore volume of 0.19 cm^3/g correlating to a volume porosity of 54%. The final resulting material after calcination at 1100 ºC maintained a volume porosity of 23%,

demonstrating that the synthesized porous YSZ could be a viable material for higher temperature applications.

The preservation of the desired cubic structure is also key during increased calcination temperatures. As explained previously, XRD can be used for the determination of crystallite size, however Raman spectroscopy must be used for phase determination to distinguish between tetragonal and cubic phase. It can be seen that increasing calcination temperature results in an increase in tetragonal phase present. Sample M1_600 shows very broad, weak peaks at 250, 320 470, and 640 cm^{-1} indicating the presence of some tetragonal phase, but a dominant broad peak between 560 and 615 cm^{-1} belongs to the cubic phase (Figure 6.8). The broad peak associated with the cubic phase is still dominant up to 900 ºC, after which the four peaks assigned to the tetragonal phase become more pronounced. Increasing the mol % of Y_2O_3 might provide complete stabilization of the porous YSZ material at high temperature, however the lowest doping content possible is desired for SOFC applications.

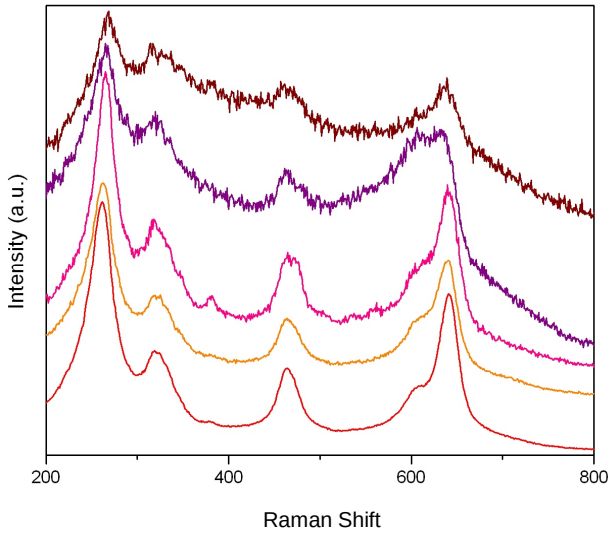

Figure 6.8. Raman spectra for Z4_600, Z4_800, Z4_900, Z4_1000, and Z4_1100 (listed top to bottom), highest porosity samples calcined at indicated temperatures.

6.5 Conclusion

Highly porous yttria-stabilized zirconia materials have numerous catalysis, catalytic support, and fuel cell applications. Currently, supercritical drying and templating techniques have been the only options for synthesizing such materials with the final products showing limited thermal stability, mechanical robustness, and requiring expensive precursors and time consuming techniques. It has been presented here that the formation of interpenetrating inorganic and organic networks by concurrent gelation technique was successfully applied to the synthesis of 9 mol % YSZ. The removal of the organic portion through calcination resulted in porous, crystalline products with controllable pore size and pore volume by varying the volume of organic component, the best having a volume porosity of 63%. Raman spectroscopy confirmed the

stabilization of the desired cubic phase up to 900 ºC, with partial stabilization up to 1100 ºC where the final material maintained a 23% volume porosity. The produced YSZ material shows thermal and mechanical structure stability. All of the past and current reported techniques for producing porous YSZ materials demonstrate the difficulty in finding a synthetic procedure that results in the formation of a YSZ material that contain all of the desired mechanical, structural and conductive properties needed for wide-use applications. Most of the reported procedures are able to exploit one property at the expense of the others, making porous YSZ systems very challenging from a synthetic point of view. The use of a sequential gelation process forming two interpenetrating networks seems very promising in that the final material produced shows mechanical and thermal stability as well as having the desired phase and controllable pore properties.

6.6 References

(1) Nawrocki, J.; Rigney, M. P.; McCormick, A.; Carr, P. W. *Journal of Chromatography, A* **1993**, *657*, 229.

(2) Kontoyannis, C. G.; Orkoula, M. *Journal of Materials Science* **1994**, *29*, 5316.

(3) Ingel, R. P.; Lewis, D., III *Journal of the American Ceramic Society* **1986**, *69*, 325.

(4) Strickler, D. W.; Carlson, W. G. *Journal of the American Ceramic Society* **1964**, *47*, 122.

(5) Yashima, M.; Takahashi, H.; Ohtake, K.; Hirose, T.; Kakihana, M.; Arashi, H.; Ikuma, Y.; Suzuki, Y.; Yoshimura, M. *Journal of Physics and Chemistry of Solids* **1996**, *57*, 289.

(6) Duwez, P.; Brown, F. H., Jr.; Odell, F. *Journal of the Electrochemical Society* **1951**, *98*, 356.

(7) Minh, N. Q. *Journal of the American Ceramic Society* **1993**, *76*, 563.

(8) Can, Z. Y.; Narita, H.; Mizusaki, J.; Tagawa, H. *Solid State Ionics* **1995**, *79*, 344.

(9) Dow, W.-P.; Huand, T.-J. *Journal of Catalysis* **1994**, *147*, 322.

(10) Kim, J.; Lin, Y. S. *Journal of Membrane Science* **1998**, *139*, 75.

(11) Hung, I. M.; Fung, K.-Z.; Hung, D.-T.; Hon, M.-H. *Journal of the European Ceramic Society* **2008**, *28*, 1161.

(12) Chervin, C. N.; Clapsaddle, B. J.; Chiu, H. W.; Gash, A. E.; Satcher, J. H., Jr.; Kauzlarich, S. M. *Chemistry of Materials* **2006**, *18*, 4865.

(13) Chervin, C. N.; Clapsaddle, B. J.; Chiu, H. W.; Gash, A. E.; Satcher, J. H., Jr.; Kauzlarich, S. M. *Chemistry of Materials* **2006**, *18*, 1928.

(14) Volosin, A. M.; Sharma, S.; Traverse, C.; Newman, N.; Seo, D.-K. *Journal of Materials Chemistry* **2011**, *21*, 13232 %U http://pubs.rsc.org.ezproxy1.lib.asu.edu/en/Content/ArticleLanding/2011/JM/c1jm12362a.

(15) Chervin, C. N.; Clapsaddle, B. J.; Chiu, H. W.; Gash, A. E.; Satcher, J. H., Jr.; Kauzlarich, S. M. *Chemistry of Materials* **2005**, *17*, 3345.

(16) Baumann, T. F.; Worsley, M. A.; Han, T. Y.-J.; Satcher, J. H. *Journal of Non-Crystalline Solids* **2008**, *354*, 3513.

(17) Brandt, R.; Fricke, J. *Journal of Non-Crystalline Solids* **2004**, *350*, 131.

(18) Reuss, M.; Ratke, L. *Journal of Sol-Gel Science and Technology* **2008**, *47*, 74.

(19) Leventis, N.; Chandrasekaran, N.; Sadekar, A. G.; Mulik, S.; Sotiriou-Leventis, C. *J. Mater. Chem.* **2010**, *20*, 7456.

(20) Leventis, N.; Chandrasekaran, N.; Sadekar, A. G.; Sotiriou-Leventis, C.; Lu, H. *Journal of the American Chemical Society* **2009**, *131*, 4576.

(21) Yashima, M.; Sasaki, S.; Kakihana, M.; Yamaguchi, Y.; Arashi, H. *Acta Crystallographica, Section B: Structural Science* **1994**, *B50*, 663.

(22) Southon, P., University of Technology, Sydney, 2000.

(23) Sing, K. S. W.; Everett, D. H.; Haul, R. A. W.; Moscou, L.; Pierotti, R. A.; Rouquerol, J.; Siemieniewska, T. *Pure and Applied Chemistry* **1985**, *57*, 603.

(24) Pekala, R. W.; Office, U. S. P., Ed.; The United States of America as represented by the Department of Energy: United States, 1992; Vol. 5,086,085, p 10.

References

Chapter 1 References

(1) Livage, J.; Babonneau, F.; Sanchez, C. *Sol-Gel Opt.* **1994**, 39.

(2) K. Ishizaki, S. K., and M. Nanko *Porous Materials; Process technology and applications*; Kluwer Academic Publishers, 1998.

(3) Chan, K. K.; Brownstein, A. M. *American Ceramic Society Bulletin* **1991**, *70*, 703.

(4) Thomas, J. M.; Hernandez-Garrido, J. C.; Raja, R.; Bell, R. G. *Physical Chemistry Chemical Physics* **2009**, *11*, 2799.

(5) Pierre, A. C.; Pajonk, G. M. *Chemical Reviews (Washington, DC, United States)* **2002**, *102*, 4243.

(6) Fryxell, G. E.; Mattigod, S. V.; Lin, Y.; Wu, H.; Fiskum, S.; Parker, K.; Zheng, F.; Yantasee, W.; Zemanian, T. S.; Addleman, R. S.; Liu, J.; Kemner, K.; Kelly, S.; Feng, X. *Journal of Materials Chemistry* **2007**, *17*, 2863.

(7) Huo, Q.; Margolese, D. I.; Ciesla, U.; Feng, P.; Gier, T. E.; Sieger, P.; Leon, R.; Petroff, P. M.; Schueth, F.; Stucky, G. D. *Nature (London, United Kingdom)* **1994**, *368*, 317.

(8) Zhang, Z.; Hicks, R. W.; Pauly, T. R.; Pinnavaia, T. J. *Journal of the American Chemical Society* **2002**, *124*, 1592.

(9) Baumann, T. F.; Gash, A. E.; Fox, G. A.; Satcher, J. H., Jr.; Hrubesh, L. W. In *Handb. Porous Solids*; Schüth, F., Sing, K. S. W., Weitkamp, J., Eds.; Wiley-VCH: Weinheim, Germany, 2002; Vol. 3, p 2014.

(10) De Soler-Illia, G. J.; Sanchez, C.; Lebeau, B.; Patarin, J. *Chemical Reviews (Washington, DC, United States)* **2002**, *102*, 4093.

(11) Long, J. W.; Rolison, D. R. *Acc. Chem. Res.* **2007**, *40*, 854.

(12) Schaefer, D. W. *MRS Bulletin* **1994**, *19*, 14.

(13) Husing, N.; Schubert, U. *Angewandte Chemie, International Edition* **1998**, *37*, 22.

(14) SciFinder; CAS American Chemical Society: 2010.

(15) Sohlberg, K.; Pennycook, S. J.; Pantelides, S. T. *Journal of the American Chemical Society* **1999**, *121*, 7493.

(16) Duwez, P.; Brown, F. H., Jr.; Odell, F. *Journal of the Electrochemical Society* **1951**, *98*, 356.

(17) Brinker, C. J.; Scherer, G. W. In *Sol-Gel Science*; Academic Press: Boston: 1990, p 839.

(18) Livage, J.; Henry, M.; Sanchez, C. *Progress in Solid State Chemistry* **1988**, *18*, 259.

(19) Hench, L. L.; West, J. K. *Chem. Rev.* **1990**, *90*, 33.

(20) Brinker, C. J.; Scherer, G. W. In *Sol-Gel Science*; Academic Press: Boston: 1990, p 1.

(21) Baumann, T. F.; Gash, A. E.; Chinn, S. C.; Sawvel, A. M.; Maxwell, R. S.; Satcher, J. H., Jr. *Chem. Mater.* **2005**, *17*, 395.

(22) Gash, A. E.; Satcher; Simpson, R. L. *Chemistry of Materials* **2003**, *15*, 3268.

(23) Chervin, C. N.; Clapsaddle, B. J.; Chiu, H. W.; Gash, A. E.; Satcher, J. H., Jr.; Kauzlarich, S. M. *Chemistry of Materials* **2005**, *17*, 3345.

(24) Brinker, C. J.; Scherer, G. W. In *Sol-Gel Science*; Academic Press: Boston: 1990, p 21.

(25) Gash, A. E.; Tillotson, T. M.; Satcher Jr, J. H.; Hrubesh, L. W.; Simpson, R. L. *Journal of Non-Crystalline Solids* **2001**, *285*, 22.

(26) Gash, A. E.; Tillotson, T. M.; Satcher, J. H., Jr.; Poco, J. F.; Hrubesh, L. W.; Simpson, R. L. *Chem. Mater.* **2001**, *13*, 999.

(27) Rolison, D. R.; Dunn, B. *J. Mater. Chem.* **2001**, *11*, 963.

(28) Brinker, C. J.; Scherer, G. W. In *Sol-Gel Science*; Academic Press: Boston: 1990, p 453.

(29) Brinker, C. J.; Scherer, G. W. In *Sol-Gel Science*; Academic Press: Boston: 1990, p 407.

(30) Kistler, S. S. *Nature (London, U. K.)* **1931**, *127*, 741.

(31) Kistler, S. S. *Journal of Physical Chemistry* **1932**, *36*, 52.

(32) Deshpande, R.; Smith, D. M.; Brinker, C. J. *Materials Research Society Symposium Proceedings* **1992**, *271*, 553.

(33) Huling, J. C.; Bailey, J. K.; Smith, D. M.; Brinker, C. J. *Materials Research Society Symposium Proceedings* **1992**, *271*, 511.

(34) Einarsrud, M.-A.; Haereid, S. *Journal of Sol-Gel Science and Technology* **1994**, *2*, 903.

(35) Brinker, C. J.; Scherer, G. W. In *Sol-Gel Science*; Academic Press: Boston: 1990, p 357.

(36) Lucas, E. M.; Doescher, M. S.; Ebenstein, D. M.; Wahl, K. J.; Rolison, D. R. *J. Non-Cryst. Solids* **2004**, *350*, 244.

(37) Rolison Debra, R. *Science (New York, N.Y.)* **2003**, *299*, 1698.

(38) Parmenter, K. E.; Milstein, F. *J. Non-Cryst. Solids* **1998**, *223*, 179.

(39) Ladd, D. M.; Volosin, A.; Seo, D.-K. *Journal of Materials Chemistry* **2010**, *20*, 5923.

(40) Lu, Y.; Larock, R. C. *ChemSusChem* **2009**, *2*, 136.

(41) Belgacem, M. N.; Gandini, A. *Monomers, Polymers and Composites from Renewable Resources*; Elsevier: Amsterdam, 2008.

(42) Bautista, L. F.; Vicente, G.; Rodriguez, R.; Pacheco, M. *Biomass and Bioenergy* **2009**, *33*, 862.

Chapter 2 References

(1) Klug, H. P.; Alexander, l. E. X-Ray Diffraction Procedures; 2nd ed.; Wiley: New York, 1974.

*(2) Holzwarth, U.; Gibson, N. Nature Nanotechnology **2011**, 6, 534.*

*(3) Zhou, R. S.; Snyder, R. L. Acta Crystallographica, Section B: Structural Science **1991**, B47, 617.*

*(4) Teufer, G. Acta Crystallographica **1962**, 15, 1187.*

*(5) Martin, U.; Boysen, H.; Frey, F. Acta Crystallographica, Section B: Structural Science **1993**, B49, 403.*

(6) Southon, P., University of Technology, Sydney, 2000.

*(7) Southon, P. D.; Bartlett, J. R.; Woolfrey, J. L.; Stevens, M. G. Ceramic Transactions **1998**, 81, 75.*

*(8) Lefevre, J.; Collongues, R.; Jorba, M. P. y. Compt. rend. **1959**, 249, 2329.*

*(9) Feinberg, A.; Perry, C. H. Journal of Physics and Chemistry of Solids **1981**, 42, 513.*

*(10) Todorovska, R.; Petrova, N.; Todorovsky, D. Applied Surface Science **2005**, 252, 1266.*

*(11) Kontoyannis, C. G.; Orkoula, M. Journal of Materials Science **1994**, 29, 5316.*

(12) Mackenzie, K. J. D.; Smith, M. E. Multinuclear Solid-State NMR of Inorganic Materials; Elsevier Science Ltd: Kindlington, Oxford, 2002.

(13) Duer, M. J. Solid-State NMR Spectroscopy; Blackwell Publishing Ltd: Oxford, UK, 2004.

(14) Williams, D. B.; Carter, C. B. Transmission Electron Microscopy: A Textbook for Materials Science; Plenum Press: New York, 1996; Vol. 1.

*(15) Stroud, R. M.; Long, J. W.; Pietron, J. J.; Rolison, D. R. Journal of Non-Crystalline Solids **2004**, 350, 277.*

*(16) Chervin, C. N.; Clapsaddle, B. J.; Chiu, H. W.; Gash, A. E.; Satcher, J. H., Jr.; Kauzlarich, S. M. Chemistry of Materials **2006**, 18, 4865.*

*(17) Baumann, T. F.; Gash, A. E.; Chinn, S. C.; Sawvel, A. M.; Maxwell, R. S.; Satcher, J. H., Jr. Chemistry of Materials **2005**, 17, 395.*

(18) Condon, J. B. Surface Area and Porosity Determinations by Physisorption; Elsevier: The Netherlands, 2006.

*(19) Brunauer, S.; Emmett, P. H.; Teller, E. Journal of the American Chemical Society **1938**, 60, 309.*

(20) Volosin, A., Surface Area and Pore Measurement in Porous Materials.

Chapter 3 References

(1) Trueba, M.; Trasatti, S. P. *European Journal of Inorganic Chemistry* **2005**, 3393.

(2) Li, W.-C.; Lu, A.-H.; Schmidt, W.; Schueth, F. *Chemistry--A European Journal* **2005**, *11*, 1658.

(3) Choi, J.; Suh, D. J. *Catalysis Surveys from Asia* **2007**, *11*, 123.

(4) Euzen, P., Raybaud, P., Krokidis, X., Toulhoat, H., Le Loarer, J., Jolivet, J., Froidefond, C *Handbook of Porous Solids*; Wiley-VCH: Weiheim, 2002.

(5) Yoldas, B. E. *Journal of Applied Chemistry & Biotechnology* **1973**, *23*, 803.

(6) Yoldas, B. E. *Journal of Materials Science* **1975**, *10*, 1856.

(7) Yoldas, B. E. *American Ceramic Society Bulletin* **1975**, *54*, 289.

(8) Yoldas, B. E. *American Ceramic Society Bulletin* **1975**, *54*, 286.

(9) Baumann, T. F.; Gash, A. E.; Chinn, S. C.; Sawvel, A. M.; Maxwell, R. S.; Satcher, J. H., Jr. *Chemistry of Materials* **2005**, *17*, 395.

(10) Baes, C. F., Mesmer, R.E. *The Hydrolysis of Cations*; John Wiley & Sons: New York, 1976.

(11) Livage, J.; Henry, M.; Sanchez, C. *Progress in Solid State Chemistry* **1988**, *18*, 259.

(12) Jolivet, J.-P.; Henry, M.; Livage, J.; Bescher, E. *Metal Oxide Chemistry and Synthesis: From Solution to Solid State*; John Wiley & Sons: New York, 2000.

(13) De Soler-Illia, G. J.; Sanchez, C.; Lebeau, B.; Patarin, J. *Chemical Reviews (Washington, DC, United States)* **2002**, *102*, 4093.

(14) Baumann, T. F.; Gash, A. E.; Fox, G. A.; Satcher, J. H., Jr.; Hrubesh, L. W. In *Handb. Porous Solids*; Schüth, F., Sing, K. S. W., Weitkamp, J., Eds.; Wiley-VCH: Weinheim, Germany, 2002; Vol. 3, p 2014.

(15) Rouquerol, F.; Rouquerol, J.; Sing, K. *Adsorption by Powders and Porous Solids: Principles, Methodology and Applications*; Academic: San Diego, 1999.

(16) Pierre, A. C.; Pajonk, G. M. *Chemical Reviews (Washington, DC, United States)* **2002**, *102*, 4243.

(17) Tetramethyfuran (THF) can be used as an alternative which does not give any polluting gases upon burning.

(18) Zhang, Z.; Hicks, R. W.; Pauly, T. R.; Pinnavaia, T. J. *Journal of the American Chemical Society* **2002**, *124*, 1592.

(19) Suh, D. J.; Park, T.-J.; Kim, J.-H.; Kim, K.-L. *Chemistry of Materials* **1997**, *9*, 1903.

(20) Wilson, S. J.; McConnell, J. D. C. *Journal of Solid State Chemistry* **1980**, *34*, 315.

(21) Krokidis, X.; Raybaud, P.; Gobichon, A.-E.; Rebours, B.; Euzen, P.; Toulhoat, H. *Journal of Physical Chemistry B* **2001**, *105*, 5121.

(22) Kucheyev, S. O.; Baumann, T. F.; Cox, C. A.; Wang, Y. M.; Satcher, J. H., Jr.; Hamza, A. V.; Bradby, J. E. *Applied Physics Letters* **2006**, *89*, 041911/1.

(23) Long, J. W.; Rolison, D. R. *Accounts of Chemical Research* **2007**, *40*, 854.

(24) Oberlander, R. K. *Appl. Ind. Catal.* **1984**, *3*, 63.

(25) Lowell, S.; Shield, J. E.; Thomas, M. A.; Thommes, M. *Characterization of Porous Solids and Powders: Surface Area, and Density*; Kluwer: Dordrecht, The Netherlands, 2004; Vol. 84.

(26) MacKenzie, K. J. D. *Multinuclear Solid-State Nuclear Magnetic Resonance of Inorganic Materials*; Pergamon: New York, 2002.

(27) Khaleel, A. A.; Klabunde, K. J. *Chemistry--A European Journal* **2002**, *8*, 3991.

(28) Wang, J. A.; Bokhimi, X.; Morales, A.; Novaro, O.; Lopez, T.; Gomez, R. *The Journal of Physical Chemistry B* **1998**, *103*, 299.

(29) Hidalgo, F. J.; Zamora, R. In *Handbook of Food Science, Technology, and Engineering; 4 Volume Set*; Hui, Y. H., Ed. 2005; Vol. 1, p 3632 pp.

(30) Ndiaye, P. M.; Tavares, F. W.; Dalmolin, I.; Dariva, C.; Oliveira, D.; Oliveira, J. V. *Journal of Chemical and Engineering Data* **2005**, *50*, 330.

(31) Scholz, V.; Nogueira da Silva, J. *Biomass and Bioenergy* **2008**, *32*, 95.

(32) Ogunniyi, D. S. *Bioresource Technology* **2006**, *97*, 1086.

(33) Conceição, M. M.; Fernandes; Araújo, A. S.; Farias, M. F.; Santos, I. M. G.; Souza, A. G. *Energy & Fuels* **2007**, *21*, 1522.

(34) Mondal, P.; Basu, M.; Balasubramanian, N. *Biofuels, Bioproducts & Biorefining* **2008**, *2*, 155.

(35) Demirbas, A. *Energy Conversion and Management* **2008**, *50*, 14.

(36) Lee, J.; Orilall, M. C.; Warren, S. C.; Kamperman, M.; DiSalvo, F. J.; Wiesner, U. *Nature Materials* **2008**, *7*, 222.

(37) Caps, R.; Fricke, J. *Sol-Gel Technologies for Glass Producers and Users* **2004**, 349.

(38) Norris, P. M.; Shrinivasan, S. *Annual Review of Heat Transfer* **2005**, *14*, 385.

Chapter 4 References

(1) Husing, N.; Schubert, U. *Angewandte Chemie, International Edition* **1998**, *37*, 22.

(2) Kucheyev, S. O.; Baumann, T. F.; Cox, C. A.; Wang, Y. M.; Satcher, J. H., Jr.; Hamza, A. V.; Bradby, J. E. *Applied Physics Letters* **2006**, *89*, 041911/1.

(3) Pajonk, G. M. *Catalysis Today* **1999**, *52*, 3.

(4) Tiemann, M. *Chemistry--A European Journal* **2007**, *13*, 8376.

(5) Rao, Y.; Antonelli, D. M. *J. Mater. Chem.* **2009**, *19*, 1937.

(6) Carlson, G.; Lewis, D.; McKinley, K.; Richardson, J.; Tillotson, T. *Journal of Non-Crystalline Solids* **1995**, *186*, 372.

(7) Alie, C.; Pirard, R.; Lecloux, A. J.; Pirard, J.-P. *Journal of Non-Crystalline Solids* **1999**, *246*, 216.

(8) Kim, S.-W.; Iwamoto, S.; Inoue, M. *Journal of Porous Materials* **2010**, *17*, 377.

(9) Klvana, D.; Chaouki, J.; Repellin-Lacroix, M.; Pajonk, G. M. *Journal de Physique, Colloque* **1989**, C4.

(10) Baumann, T. F.; Gash, A. E.; Fox, G. A.; Satcher, J. H., Jr.; Hrubesh, L. W. In *Handbook of Porous Solids*; Schüth, F., Sing, K. S. W., Weitkamp, J., Eds.; Wiley-VCH: Weinheim, Germany, 2002; Vol. 3, p 2014.

(11) Jarzebski, A. B.; Lorenc, J.; Aristov, Y. I.; Lisitza, N. *Journal of Non-Crystalline Solids* **1995**, *190*, 198.

(12) Rolison, D. R.; Dunn, B. *Journal of Materials Chemistry* **2001**, *11*, 963.

(13) Trueba, M.; Trasatti, S. P. *European Journal of Inorganic Chemistry* **2005**, 3393.

(14) Seki, T.; Onaka, M. *Catalysis Surveys from Asia* **2006**, *10*, 138.

(15) Rambo, C. R.; Sieber, H. *Advanced Materials (Weinheim, Germany)* **2005**, *17*, 1088.

(16) Pinnavaia, T. J.; Zhang, Z.; Hicks, R. W. *Studies in Surface Science and Catalysis* **2005**, *156*, 1.

(17) Baumann, T. F.; Gash, A. E.; Chinn, S. C.; Sawvel, A. M.; Maxwell, R. S.; Satcher, J. H., Jr. *Chemistry of Materials* **2005**, *17*, 395.

(18) Suh, D. J.; Park, T.-J.; Kim, J.-H.; Kim, K.-L. *Chemistry of Materials* **1997**, *9*, 1903.

(19) Ladd, D. M.; Volosin, A.; Seo, D.-K. *Journal of Materials Chemistry* **2010**, *20*, 5923.

(20) Fountain, C. W.; Jennings, J.; McKie, C. K.; Oakman, P.; Fetterolf, M. L. *Journal of Chemical Education* **1997**, *74*, 224.

(21) U.S. Department of Agriculture, Agricultural Research Service. 2009. USDA National Nutrient Database for Standard Reference, Release 22. Nutrient Data Laboratory Home Page, http://www.ars.usda.gov/ba/bhnrc/ndl, products and services-fats and oils.

(22) Zhang, Z.; Hicks, R. W.; Pauly, T. R.; Pinnavaia, T. J. *Journal of the American Chemical Society* **2002**, *124*, 1592.

(23) Wilson, S. J.; McConnell, J. D. C. *Journal of Solid State Chemistry* **1980**, *34*, 315.

(24) Krokidis, X.; Raybaud, P.; Gobichon, A.-E.; Rebours, B.; Euzen, P.; Toulhoat, H. *Journal of Physical Chemistry B* **2001**, *105*, 5121.

(25) Caps, R.; Fricke, J. *Sol-Gel Technologies for Glass Producers and Users* **2004**, 349.

(26) Norris, P. M.; Shrinivasan, S. *Annual Review of Heat Transfer* **2005**, *14*, 385.

(27) Ogunniyi, D. S. *Bioresource Technology* **2006**, *97*, 1086.

(28) Conceição, M. M.; Fernandes; Araújo, A. S.; Farias, M. F.; Santos, I. M. G.; Souza, A. G. *Energy & Fuels* **2007**, *21*, 1522.

(29) Mondal, P.; Basu, M.; Balasubramanian, N. *Biofuels, Bioproducts & Biorefining* **2008**, *2*, 155.

Chapter 5 References

(1) Iler, R. K. *The Chemistry of Silica*; Wiley New York, 1979.

(2) Brinker, C. J.; Scherer, G. W. In *Sol-Gel Science*; Academic Press: Boston, 1990, p 97.

(3) Kistler, S. S. *Nature (London, United Kingdom)* **1931**, *127*, 741.

(4) Blanchard, F.; Reymond, J. P.; Pommier, B.; Teichner, S. J. *Journal of Molecular Catalysis* **1982**, *17*, 171.

(5) Bond, G. C.; Flamerz, S. *Applied Catalysis* **1987**, *33*, 219.

(6) Pajonk, G. M. *Applied Catalysis* **1991**, *72*, 217.

(7) Wang, L.; Eguchi, K.; Arai, H.; Seiyama, T. *Applied Catalysis* **1987**, *33*, 107.

(8) Rolison Debra, R. *Science (New York, N.Y.)* **2003**, *299*, 1698.

(9) Fricke, J.; Caps, R.; Buettner, D.; Heinemann, U.; Huemmer, E.; Kadur, A. *Solar Energy Materials* **1987**, *16*, 267.

(10) Fricke, J.; Reichenauer, G. *Journal of Non-Crystalline Solids* **1987**, *95-96*, 1135.

(11) Tewari, P. H.; Hunt, A. J.; (United States Dept. of Energy, USA). Application: US
US, 1986, p 6 pp.

(12) Tewari, P. H.; Hunt, A. J.; Lofftus, K. D. *Springer Proceedings in Physics* **1986**, *6*, 31.

(13) Gronauer, M.; Fricke, J. *Acustica* **1986**, *59*, 177.

(14) Gibiat, V.; Lefeuvre, O.; Woignier, T.; Pelous, J.; Phalippou, J. *Journal of Non-Crystalline Solids* **1995**, *186*, 244.

(15) Gesser, H. D.; Goswami, P. C. *Chemical Reviews (Washington, DC, United States)* **1989**, *89*, 765.

(16) Poelz, G.; Riethmueller, R. *Nuclear Instruments & Methods in Physics Research* **1982**, *195*, 491.

(17) Aspen aerogels. 2011.

(18) Nanopore **2008**.

(19) Gurav, J. L.; Jung, I.-K.; Park, H.-H.; Kang, E. S.; Nadargi, D. Y. *Journal of Nanomaterials* **2010**, No pp given.

(20) Gurav, J. L.; Nadargi, D. Y.; Rao, A. V. *Applied Surface Science* **2008**, *255*, 3019.

(21) Gurav, J. L.; Rao, A. V.; Bangi, U. K. H. *Journal of Alloys and Compounds* **2009**, *471*, 296.

(22) Gurav, J. L.; Rao, A. V.; Nadargi, D. Y.; Park, H.-H. *Journal of Materials Science* **2010**, *45*, 503.

(23) Gurav, J. L.; Rao, A. V.; Rao, A. P.; Nadargi, D. Y.; Bhagat, S. D. *Journal of Alloys and Compounds* **2009**, *476*, 397.

(24) Lucas, E. M.; Doescher, M. S.; Ebenstein, D. M.; Wahl, K. J.; Rolison, D. R. *Journal of Non-Crystalline Solids* **2004**, *350*, 244.

(25) Ladd, D. M.; Volosin, A.; Seo, D.-K. *Journal of Materials Chemistry* **2010**, *20*, 5923.

(26) Ernest Orlando Lawrence, B. N. L.

(27) Brinker, C. J.; Scherer, G. W. In *Sol-Gel Science*; Academic Press: Boston: 1990, p 357.

(28) Jiao, J.; Sun, X.; Pinnavaia, T. J. *Polymer* **2009**, *50*, 983.

Chapter 6 References

(1) Nawrocki, J.; Rigney, M. P.; McCormick, A.; Carr, P. W. *Journal of Chromatography, A* **1993**, *657*, 229.

(2) Kontoyannis, C. G.; Orkoula, M. *Journal of Materials Science* **1994**, *29*, 5316.

(3) Ingel, R. P.; Lewis, D., III *Journal of the American Ceramic Society* **1986**, *69*, 325.

(4) Strickler, D. W.; Carlson, W. G. *Journal of the American Ceramic Society* **1964**, *47*, 122.

(5) Yashima, M.; Takahashi, H.; Ohtake, K.; Hirose, T.; Kakihana, M.; Arashi, H.; Ikuma, Y.; Suzuki, Y.; Yoshimura, M. *Journal of Physics and Chemistry of Solids* **1996**, *57*, 289.

(6) Duwez, P.; Brown, F. H., Jr.; Odell, F. *Journal of the Electrochemical Society* **1951**, *98*, 356.

(7) Minh, N. Q. *Journal of the American Ceramic Society* **1993**, *76*, 563.

(8) Can, Z. Y.; Narita, H.; Mizusaki, J.; Tagawa, H. *Solid State Ionics* **1995**, *79*, 344.

(9) Dow, W.-P.; Huand, T.-J. *Journal of Catalysis* **1994**, *147*, 322.

(10) Kim, J.; Lin, Y. S. *Journal of Membrane Science* **1998**, *139*, 75.

(11) Hung, I. M.; Fung, K.-Z.; Hung, D.-T.; Hon, M.-H. *Journal of the European Ceramic Society* **2008**, *28*, 1161.

(12) Chervin, C. N.; Clapsaddle, B. J.; Chiu, H. W.; Gash, A. E.; Satcher, J. H., Jr.; Kauzlarich, S. M. *Chemistry of Materials* **2006**, *18*, 4865.

(13) Chervin, C. N.; Clapsaddle, B. J.; Chiu, H. W.; Gash, A. E.; Satcher, J. H., Jr.; Kauzlarich, S. M. *Chemistry of Materials* **2006**, *18*, 1928.

(14) Volosin, A. M.; Sharma, S.; Traverse, C.; Newman, N.; Seo, D.-K. *Journal of Materials Chemistry* **2011**, *21*, 13232 %U http://pubs.rsc.org.ezproxy1.lib.asu.edu/en/Content/ArticleLanding/2011/JM/c1jm12362a.

(15) Chervin, C. N.; Clapsaddle, B. J.; Chiu, H. W.; Gash, A. E.; Satcher, J. H., Jr.; Kauzlarich, S. M. *Chemistry of Materials* **2005**, *17*, 3345.

(16) Baumann, T. F.; Worsley, M. A.; Han, T. Y.-J.; Satcher, J. H. *Journal of Non-Crystalline Solids* **2008**, *354*, 3513.

(17) Brandt, R.; Fricke, J. *Journal of Non-Crystalline Solids* **2004**, *350*, 131.

(18) Reuss, M.; Ratke, L. *Journal of Sol-Gel Science and Technology* **2008**, *47*, 74.

(19) Leventis, N.; Chandrasekaran, N.; Sadekar, A. G.; Mulik, S.; Sotiriou-Leventis, C. *J. Mater. Chem.* **2010**, *20*, 7456.

(20) Leventis, N.; Chandrasekaran, N.; Sadekar, A. G.; Sotiriou-Leventis, C.; Lu, H. *Journal of the American Chemical Society* **2009**, *131*, 4576.

(21) Yashima, M.; Sasaki, S.; Kakihana, M.; Yamaguchi, Y.; Arashi, H. *Acta Crystallographica, Section B: Structural Science* **1994**, *B50*, 663.

(22) Southon, P., University of Technology, Sydney, 2000.

(23) Sing, K. S. W.; Everett, D. H.; Haul, R. A. W.; Moscou, L.; Pierotti, R. A.; Rouquerol, J.; Siemieniewska, T. *Pure and Applied Chemistry* **1985**, *57*, 603.

(24) Pekala, R. W.; Office, U. S. P., Ed.; The United States of America as represented by the Department of Energy: United States, 1992; Vol. 5,086,085, p 10.